The neural basis of the blood-oxygen-level-dependent functional magnetic resonance imaging signal

Nikos K. Logothetis

Max Planck Institute for Biological Cybernetics, Spemannstrasse 38, 72076 Tübingen, Germany
(nikos.logothetis@tuebingen.mpg.de)

Magnetic resonance imaging (MRI) has rapidly become an important tool in clinical medicine and biological research. Its functional variant (functional magnetic resonance imaging; fMRI) is currently the most widely used method for brain mapping and studying the neural basis of human cognition. While the method is widespread, there is insufficient knowledge of the physiological basis of the fMRI signal to interpret the data confidently with respect to neural activity. This paper reviews the basic principles of MRI and fMRI, and subsequently discusses in some detail the relationship between the blood-oxygen-level-dependent (BOLD) fMRI signal and the neural activity elicited during sensory stimulation. To examine this relationship, we conducted the first simultaneous intracortical recordings of neural signals and BOLD responses. Depending on the temporal characteristics of the stimulus, a moderate to strong correlation was found between the neural activity measured with microelectrodes and the BOLD signal averaged over a small area around the microelectrode tips. However, the BOLD signal had significantly higher variability than the neural activity, indicating that human fMRI combined with traditional statistical methods underestimates the reliability of the neuronal activity. To understand the relative contribution of several types of neuronal signals to the haemodynamic response, we compared local field potentials (LFPs), single- and multi-unit activity (MUA) with high spatio-temporal fMRI responses recorded simultaneously in monkey visual cortex. At recording sites characterized by transient responses, only the LFP signal was significantly correlated with the haemodynamic response. Furthermore, the LFPs had the largest magnitude signal and linear systems analysis showed that the LFPs were better than the MUAs at predicting the fMRI responses. These findings, together with an analysis of the neural signals, indicate that the BOLD signal primarily measures the input and processing of neuronal information within a region and not the output signal transmitted to other brain regions.

Keywords: functional magnetic resonance imaging; monkey; local field potentials; multi-unit activity; action potentials; synaptic activity

1. INTRODUCTION

Modern *in vivo* imaging is one of medicine's most exciting success stories. It has optimized diagnostics and enabled us to monitor therapeutics, providing not only clinically essential information but also insight into the basic mechanisms of brain function and malfunction. Its recently developed functional variant has had an analogous impact in a number of different research disciplines ranging from developmental biology to cognitive psychology.

In the neurosciences, imaging techniques are indispensable. Understanding how the brain functions requires not only a comprehension of the physiological workings of its individual elements, that is its neurons and glia cells, but also demands a detailed map of its functional architecture and a description of the connections between populations of neurons, the networks that underlie behaviour. Furthermore, the functional plasticity of the brain, that is reflected in its capacity for anatomical reorganization, means that a mere snapshot of its architecture is not enough. Instead,

we need repeated, conjoined anatomical and physiological observations of the connectivity patterns at different organizational levels. *In vivo* imaging is an ideal tool for such observations, and is currently the only tool that can link perception, cognition and action with their neural substrates in humans.

In this review, I will first very briefly describe the history and basic principles of modern imaging techniques, and then concentrate on the application of MRI to the study of the monkey brain. Emphasis will be placed on fMRI at high spatio-temporal resolution and its combination with electrophysiological measurements. Finally, the neural origin of the BOLD contrast mechanism of fMRI will be discussed.

2. BASIC PRINCIPLES AND HISTORY

(a) *Neuronal activity, energy metabolism and brain imaging*

Most current imaging techniques, in particular those used to assess brain function, capitalize on the interconnections among CBF, energy demand and neural activity. It is therefore worth devoting a few paragraphs to an introduction of some basic concepts. Although comprising only

1003

2% of the total body mass, the brain receives 12–15% of the cardiac output and consumes *ca.* 20% of the oxygen entering the body (Siesjo 1978). The energy requirement of the brain, or the CMR, is usually expressed simply in terms of oxygen consumption ($CMRO_2$). This simplification is possible because *ca.* 90% of the glucose ($5 \, mg \, kg^{-1} \, min^{-1}$) is aerobically metabolized, and therefore parallels oxygen consumption. $CMRO_2$ is proportional to neural activity and is four times greater in grey than in WM. At rest, the brain consumes oxygen at an average rate of *ca.* 3.5 ml of oxygen per 100 g of brain tissue per minute (Siesjo 1978; Ames 2000). Approximately 50–60% of the energy produced by this consumption supports electrophysiological function, as large amounts of energy are required for the maintenance and restoration of ionic gradients and for the synthesis, transport and reuptake of neurotransmitters (Siesjo 1978; Ames 2000). The remainder of the energy is used for cellular homeostatic activities, including the maintenance of the neuron's relatively large membrane mass.

The brain's substantial demand for substrates requires the adequate delivery of oxygen and glucose via the CBF. The space constraints imposed by the non-compliant cranium and meninges require that the blood flow be sufficient without ever being excessive. It is hardly surprising, then, that there are very elaborate mechanisms regulating the CBF and that these mechanisms are closely coupled with regional neural activity.

Angelo Mosso (1881) first demonstrated the correlation between energy demand and the CBF. He measured brain pulsations in a patient who had a permanent defect in the skull over the frontal lobes. Mosso (1881) observed a sudden increase in pulsation, presumably due to an increase in the flow, immediately after the patient was asked to perform simple arithmetic calculations. Interestingly, there was no concomitant increase in the patient's heart rate or blood pressure as commonly measured at the forearm. Some years later, the neurosurgeon John Fulton (1928) reported an increase in blood flow with increased regional neural activation in the occipital lobe of another patient with a bony defect that permitted the acoustical recording of the bruit from a vascular malformation.

Experimental evidence of the activity–flow coupling was provided by Roy & Sherrington (1890) after conducting experiments on laboratory animals. Roy & Sherrington indicated that some products of the brain's metabolism stimulated vasomotor activity that probably alters the regional vascular supply in response to local variations in the functional activity. In their seminal and remarkably insightful study, they conclude that '…the chemical products of cerebral metabolism contained in the lymph that bathes the walls of the arterioles of the brain can cause variations of the calibre of the cerebral vessels: that in this re-action the brain possesses an intrinsic mechanism by which its vascular supply can be varied locally in correspondence with local variations of functional activity' (Roy & Sherrington 1890, p. 105).

The study of Roy & Sherrington was later followed by the systematic investigations of Kety & Schmidt (1948), who introduced the nitrous oxide technique, a global flow measurement method that initially seemed to disprove the notion of a local coupling of cerebral flow and neural activity (Sokoloff 1960). Experimental verification of the

regional coupling of the metabolic rate and neural activity came only from methods allowing local cerebral flow measurements. Although such methods had been used in conscious laboratory animals since the early 1960s (Sokoloff 1981), a precise quantitative assessment of the relationship between neural activity and regional blood flow was only possible after the introduction of the deoxyglucose autoradiographic technique that enabled spatially resolved measurements of glucose metabolism in laboratory animals (Sokoloff *et al.* 1977). The results of a large number of experiments with the 2DG method have indeed revealed a clear relationship between local cerebral activation and glucose consumption (Sokoloff 1977).

The first quantitative measurements of regional brain blood flow and oxygen consumption in humans were performed using the radiotracer techniques developed by Ter Pogossian *et al.* (1969, 1970) and Raichle *et al.* (1976). PET, the technology widely used today for clinical applications and research, followed (Ter Pogossian *et al.* 1975; Hoffmann *et al.* 1976) when Phelps *et al.* (1975) applied the mathematical algorithms developed by Cormack (1973) for X-ray computed tomography; for a historical review see Raichle (2000).

PET images are spatial maps of the radioactivity distribution within tissues, and are thus analogous to the autoradiograms obtained from 2DG experiments. With these PET images, it could be shown that maps of activated brain regions could be produced by detecting the indirect effects of neural activity on variables such as CBF (Fox *et al.* 1986), CBV (Fox & Raichle 1986) and blood oxygenation (Fox & Raichle 1986; Fox *et al.* 1988; Frostig *et al.* 1990).

At the same time, optical imaging using either voltage-sensitive dyes or intrinsic signals, that also relies on microvascular changes, was being developed for animal experiments and was used with great success to construct detailed maps of cortical microarchitecture in both the anaesthetized and the alert animal (Bonhoeffer & Grinvald 1996). Compared with PET, optical imaging has more limited coverage, but substantially better spatial resolution, and it can be combined easily with other physiological measurements including single-unit recordings. Finally, in recent decades another technology has emerged that could be used for conjoined anatomical and functional investigations. This new method was MRI, the technology that offers a substantially better spatio-temporal resolution than any other non-invasive method and which will be dealt with in the rest of this review.

(b) *MRI*

(i) *Nuclear magnetism*

The physical principles on which MRI is based are complex, and a thorough discussion of them is obviously beyond the scope of this article. For details, the interested reader is referred to several excellent works on this topic (Abragam 1961; Callaghan 1991; de Graaf 1998; Haacke *et al.* 1999; Stark & Bradley 1999). Here, I provide a brief description of the basic concepts to make it easier to follow the discussion of our own methodology that concludes this review.

Imaging with NMR exploits the magnetization differences that are created in a strong magnetic field. A rough description of the phenomenon can be made with a classi-
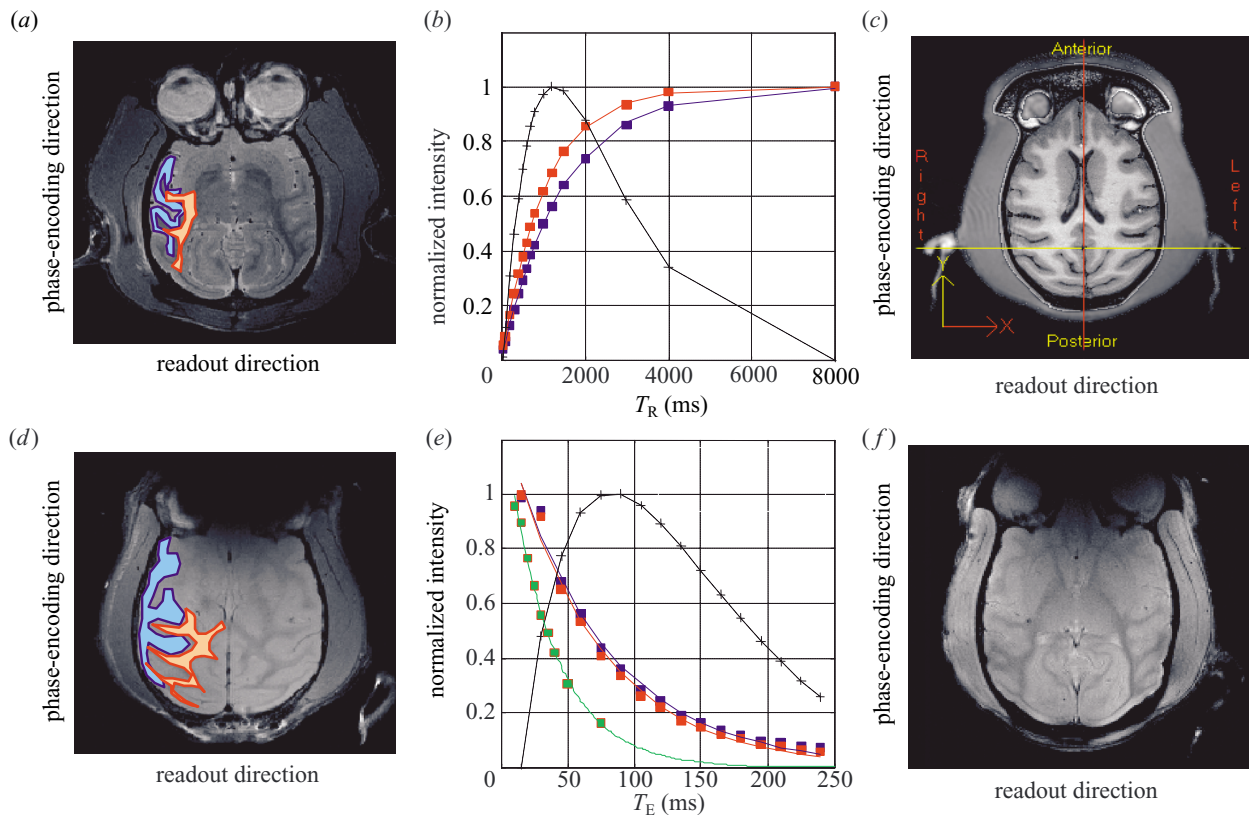
Figure 1. Relaxation curves for the GM and WM of the monkey brain. (*a*) Example of a proton-density image. The image was collected with a multi-slice, multi-echo sequence using a FOV of $128 \, \text{mm} \times 128 \, \text{mm}$ over a matrix of 256×256 voxels. Sixteen such images are acquired using T_R-values ranging from 50 to 8000 ms. (*b*) Average intensity change of voxels in cortical (blue) and WM (red) regions as a function of repetition time, T_R. T_1 is defined as the time required for *ca*. 63% of the remaining longitudinal magnetization to appear. The more 'watery' the tissue the longer its T_1 relaxation time. The WM (red curve, $T_1 = 1097$ ms) relaxes faster than the GM (blue curve, $T_1 = 1499$), so the former appears brighter in a typical T_1-weighted image than the latter (see figure 1*c*). The black trace shows the differences between the two curves. The maximum contrast is obtained with a T_R-value close to the T_1-value of the tissue having the faster relaxation. (*c*) An example of a T_1-weighted image. (*d*) An example of a spin-echo T_2-weighted image. The relaxation times for different tissues were calculated by collecting 16 such images differing in their T_E-values. (*e*) The T_2-relaxation curves for the cortex and WM, with the black trace denoting the difference between the two. The T_2-values are longer for small and shorter for large molecules, and the contrast of T_2-weighted images has a polarity opposite to that obtained with T_1. The cortex (longer T_2) in (*d*) appears brighter than WM (shorter T_2). The green trace shows the T_2^* relaxation curve for the cortical area of (*d*) T_2 GM = 74 ms (blue curve); T_2 WM = 69 ms (red curve); T_2^* GM = 36 ms (green curve). (*f*) An example of a T_2^*-weighted image collected in a multi-shot, multi-slice with an EPI sequence. T_E, echo time; T_R, repetition time; GM, grey matter; WM, white matter.

cal vector model of rotating spins, although quantum theory is needed to fully explain it. Nuclei with an odd number of protons, such as ^{1}H or ^{13}C, can be viewed as small magnets or magnetic dipoles, the vector representation of which is called the *magnetic dipole moment*, μ. Such dipoles are due to the fact that protons possess angular momentum or nuclear spin. When exposed to an external static magnetic field, the randomly oriented dipoles line up with and precess around the field's direction, thus creating a macroscopic magnetization. The rate of precession is given by the so-called Larmor relationship, $f = \gamma B_0 / 2\pi$; where f is the resonance frequency in Hz, γ is a constant called the gyromagnetic ratio, and B_0 is the magnetic field. The principal isotope ^{1}H of hydrogen relevant to most imaging studies has spin $I = \frac{1}{2}$. It has two permissible states with orientations parallel (lower energy) and antiparallel (higher energy) to the main magnetic field. The tissue magnetization that MRI uses is actually due to the tiny fractional excess of the population in the lower energy level (*ca*. 1/100 000 for a 1.5 T field) and

varies with temperature and magnetic field strength. The lower the temperature or the stronger the field, the stronger the magnetization is. NMR refers to the frequency-specific excitation produced by transitions between these two different energy states. We are able to measure the energy emitted when the system returns to equilibrium.

Inspired by the work of Stern and Gerlach in the 1920s, Rabi *et al*. (1938, 1939) were the first to apply the method of NMR to measure magnetic moments precisely. With their landmark molecular-beam experiment, they established the fundamental principle behind the technique, the 'trick' of applying a second alternating electromagnetic field resonating with the Larmor frequency inside a constant magnetic field to cause transitions between energy states. In 1946, two groups working independently of each other, Bloch *et al*. (1946) at Stanford and Purcell *et al*. (1946) at Harvard, were able to build on this foundation to measure a precessional signal from a water and a paraffin sample, respectively. In doing so, they laid the experi-

mental and theoretical foundation for NMR as it is used today (for a good collection of classical physics papers on NMR see Fukushima (1989)).

The experiment of Bloch *et al.* (1946) was the first to observe directly the electromotive force in a coil induced by the precession of nuclear moments around the static field, B_0, in a direction perpendicular to both B_0 and the applied RF field B_1. This is basically the way the MR signal is still acquired today. An RF coil is used to apply an RF pulse (an oscillating electromagnetic field of the order of 100 MHz) to excite the nuclear spins and cause the tissue magnetization to nutate on the transverse plane. The magnetization can be rotated by any arbitrary angle, commonly called the *flip* angle, θ. The optimum angle is known as the Ernst angle θ_E given by $\cos \theta_E = \exp(-T_R/T_1)$, where T_R is the time between successive excitations, the so-called repetition time, and T_1 is the spin–lattice relaxation time (see § 2b(ii)). For T_R/T_1 around 3, the relaxation between pulses is almost complete. When the pulse is off, the magnetization is subjected to the static field only, and it gradually returns to its equilibrium state emitting energy at the same radio-wave frequency. The induced voltage in a receiver RF coil has the characteristics of a damped cosine and is known as the FID. In the early days of NMR, the RF signal was a continuous wave, and only a single frequency was measured at one time. Acquisition was simplified greatly when Ernst & Anderson (1966) later introduced a technique in which a single broader-band pulse is used to excite a whole band of frequencies that can be subsequently extracted using Fourier transform analysis (Fukushima 1989, p. 84).

(ii) Relaxation processes

So far, I have described the process of obtaining an NMR signal from a tissue or sample. Two more topics need to be touched upon briefly to illustrate the principles of MRI: the process of extracting spatial information to produce an image, and that of generating contrast between the structures of that image, i.e. between different tissues. Image information is directly dependent on the strength of transverse magnetization; that in turn depends on the (proton) spin density, the so-called T_1 and T_2 relaxation times, and on other physical parameters of the tissue such as diffusion, perfusion or velocity (e.g. blood flow).

Proton spin density is determined by the number of spins that contribute to the transverse magnetization. In biological tissue, this corresponds roughly to the concentration of water. T_1 (longitudinal or spin–lattice) relaxation is an exponential process referring to the 'rebuilding' of the longitudinal 'z' magnetization (along the B_0 direction). Rebuilding occurs because of the Brownian motion of the surrounding molecules, called the *lattice*, that (motion) generates a fluctuating magnetic field. The closer the frequency of the fluctuation to the Larmor frequency the more efficient is the relaxation. Medium-sized molecules, such as lipids, match the Larmor frequency of most common fields more closely, and thus relax faster than water. Tissues differ in their T_1-values, thus providing contrast in T_1-weighted imaging. Figure 1 shows examples of relaxation curves for the grey and WM of the monkey brain. Figure 1*a* illustrates an example of a proton-density image. The image was collected with a multi-slice, multi-echo sequence using an FOV of

128×128 mm^2 over a matrix of 256×256 voxels. Sixteen such images are acquired using repetition time (T_R) values ranging from 50 to 8000 ms. The curves in figure 1*b* depict the average intensity change of the voxels in cortical (blue) and WM (red) regions as a function of T_R. The spin–lattice relaxation of the WM (red curve) is faster than that of the GM (blue curve), so the former appears lighter in a typical T_1-weighted image than the latter (see figure 1*c*). The black trace shows the differences between the two curves. The maximum contrast is obtained with a T_R close to the T_1-value of the tissue having the faster relaxation time.

T_2, also called transverse or spin–spin relaxation, however, reflects spin dephasing on the 'xy' plane as a result of mutual interactions between spins. An important mechanism at work in transverse relaxation is the energy transfer within the spin system. Any energy transition of a nucleus changes the local field at nearby nuclei. Such field variations randomly alter the frequency of the protons' precession, resulting in a loss of phase coherence and consequently of transverse magnetization. Figure 1*d* shows a spin-echo (see next paragraph) T_2-weighted image. Relaxation times for different tissues were calculated by collecting 16 such images with T_E-values ranging from 6 to 240 ms. Figure 1*e* shows the T_2-relaxation curves for cortex and WM, with the black trace denoting the difference between the two. T_2 is longer for small and shorter for large molecules, so T_2 provides a contrast with a polarity opposite to that obtained with T_1. In figure 1*d*, for instance, the cortex (longer T_2) appears brighter than the WM (shorter T_2).

In actuality the transverse magnetization decays faster than we would expect from the spin–spin relaxation process alone. T_2 actually refers to spin–spin relaxation occurring in a perfectly homogenous magnetic field. No such field exists. Local magnetic field inhomogeneities as well as inhomogeneities caused by the application of field gradients during image acquisition (see § 2b(iii)), unavoidably cause an additional 'dephasing' of magnetization. For this reason the loss of transverse magnetization occurs much more rapidly, and an FID typically has a T_2^* (T_2 star), rather than T_2, time constant reflecting the *effective* transverse relaxation time. An example of a T_2^*-weighted image is shown in figure 1*f*. To some extent the rapid signal loss can be 'recalled' by inverting the rotation direction of the spins. Indeed, the classic 'spin echo' experiment of Hahn (1950) showed that a second RF pulse (180°) applied at time τ after the initial RF excitation pulse (90°) refocuses spin coherence at 2τ ms. The measured signal is called spin echo (see figures 2 and 3) and the time at which the echo arrives is called the echo time (T_E).

(iii) Principles of imaging

One more trick is needed to create an image with encoded spatial information. As Lauterbur (1973) showed, projections of an object can be generated and images can be reconstructed, just as in X-ray computed tomography, by superimposing linear-field gradients on the main static field. Here, the term 'gradient' designates the dynamic alternations of the magnetic field along one particular dimension (e.g. $G_x = \partial B_0/\partial x$). The Larmor relationship thus becomes $f = \gamma(B_0 + G_x x + G_y y + G_z z)$, relating spatial encoding by means of, say, a gradient G_x to the MR

signal with the frequency content f. The gradient determines a range of Larmor frequencies, and those frequencies can in turn provide exact position information. This is the trick. In an actual MRI sequence there are a couple of basic elements for encoding the spatial information, i.e. gradient schemes for slice selection (G_{ss}), frequency encoding (readout) (G_{ro}), and phase encoding (G_{pe}). Here, we arbitrarily assign the directions x, y and z to the readout (frequency encoding), phase encoding and slice-selection gradient directions (ro, pe and ss, respectively).

Figure 2 shows a typical pulsing diagram for a spin-echo image (commonly referred to as the conventional spin-warp two-dimensional fast Fourier transform image). To select a slice, a frequency-selective RF pulse is used in combination with a field gradient perpendicular to the desired slice. Figure 3a shows a typical RF pulse (sinc function) used to excite the tissue and figure 3b shows the spin echoes measured by two different channels (90° out of phase) combined as complex numbers. Two further orthogonal gradients are used to extract the spatial information within the slice. The 'readout' gradient is applied at the same time as the MR data are actually acquired ('read'), while the 'phase-encode' gradient encodes the second dimension in the image plane. For an image with $N_{ro}N_{pe}$ pixels, N_{ro} points are sampled with the same 'readout' gradient G_{ro}, whereas for phase encoding the gradient G_{pe} is incremented N_{pe} times. Thus, in each readout step, the collected signal consists of the same frequencies differing only in their phases as determined by each phase-encoding step. The acquired $N_{ro}N_{pe}$ data matrix, usually termed the k space (figure 3c), with $k_{ro,pe,ss} = \gamma \int G_{ro,pe,ss}dt$, represents the image in the inverse spatial domain. Performing a Fourier transform for each row extracts the amplitudes (figure 3d), and performing it for each column extracts the phase angles of the frequency components (figure 3e). The amplitude of the central point of the k space determines the SNR of the global image. Sampling a larger number of points farther and farther away from the k space centre encodes the image's details and increases image resolution.

In many MRI methods, the acquisition of *each row* of the k space is preceded by an RF excitation. The pulse T_R is dictated by the rate of recovery of longitudinal magnetization, and the phase-encoding steps are determined by the desired resolution. Decreasing either one will affect the image quality. This makes high-quality conventional imaging too slow for comparing the MRI signal with its underlying neural activity. EPI (Mansfield 1977) permits substantially faster data acquisition, and this is the approach currently being used in most rapid imaging experiments and the one used in the studies described here (for a comprehensive review on EPI see Schmitt *et al.* (1998)). With EPI, an entire image can be created following a single excitatory pulse because it collects the complete dataset within the short time that the FID signal is detectable, that is, within a time for most applications limited by T_2^*. Refocusing in EPI is achieved by the gradient ('gradient echo') rather than RF pulses. Along the readout direction an oscillating gradient permits the generation of a train of echoes. Along the phase-encoding direction, short blips advance the encoding to the next k space line. There are many different ways of sampling the

k space corresponding to different imaging techniques (Callaghan 1991). The scheme used is very often a zigzag pattern, scanning even and odd lines from left to right and vice versa. The T_E is defined here as the time from the excitation pulse to the centre of the k space. EPI can acquire images within a very short time (less than 50 ms) and does so with a short T_R to the order of 100 ms. Its correct implementation, however, demands careful tuning of sequence parameters to minimize image artefacts.

(iv) *Image quality*

Image quality is determined by a number of interdependent variables, including the SNR, the CNR, and the spatial resolution. The SNR and CNR are both functions of the relaxation times, the scan properties, such as flip angle, interpulse delay times and the number of averages, the quality factor of the resonant input circuit (see § 4b(i)), the noise levels of the receiver, and the effective unit volume. The latter is determined by the slice thickness d, the number of phase-encoding steps N_{pe}, the number of samples in the frequency-encoding direction N_{ro} and the FOV. For an FOV of dimensions $D_{ro}D_{pe}$ the volume size is given by

$$d\frac{D_{ro}}{N_{ro}}\frac{D_{pe}}{N_{pe}},$$

and the SNR by

$$\mathrm{SNR} \approx \frac{dD_{ro}D_{pe}}{\sqrt{N_{ro}N_{pe}}}\sqrt{\mathrm{NEX}},$$

where NEX is the number of excitations (or averages). SNR also depends on the sampling frequency bandwidth; reducing the bandwidth increases SNR at the cost of increased sampling time. The maximum achievable SNR is of course determined to a significant extent by the strength of the static magnetic field, B_0. Increasing the field strengthens the MR signal in an approximately linear fashion. In practice, the SNR and CNR can be estimated by measuring the signal of a tissue region or the signal difference between two different tissue regions and expressing that signal in units of the standard deviation of the background signal (noise).

Spatial resolution is the smallest resolvable distance between two different image features. In the field of optics, it is usually determined on the basis of the Rayleigh criterion, wherein objects can be distinguished when the maximal intensity of one occurs at the first diffraction minimum of the other. An analogous expression of this criterion which is directly applicable to MRI is that between two maxima the intensity must drop below 81% of its maximum value. Nominally, the spatial resolution of an MR image is determined by the size of the image elements (voxels), that in turn is defined as the volume covered (FOV) divided by the image points sampled during acquisition ($R_{nom} = \mathrm{FOV}/N$). In other words, voxel size is defined by the slice thickness, the number of samples in the phase and frequency-encoding directions, and the FOV. The optimal selection of voxel size is important. Large voxels will inevitably average the signal from the tissue with functional variations across space. The smearing of local information acquired with large voxels—usually termed the partial volume effect—alters both the
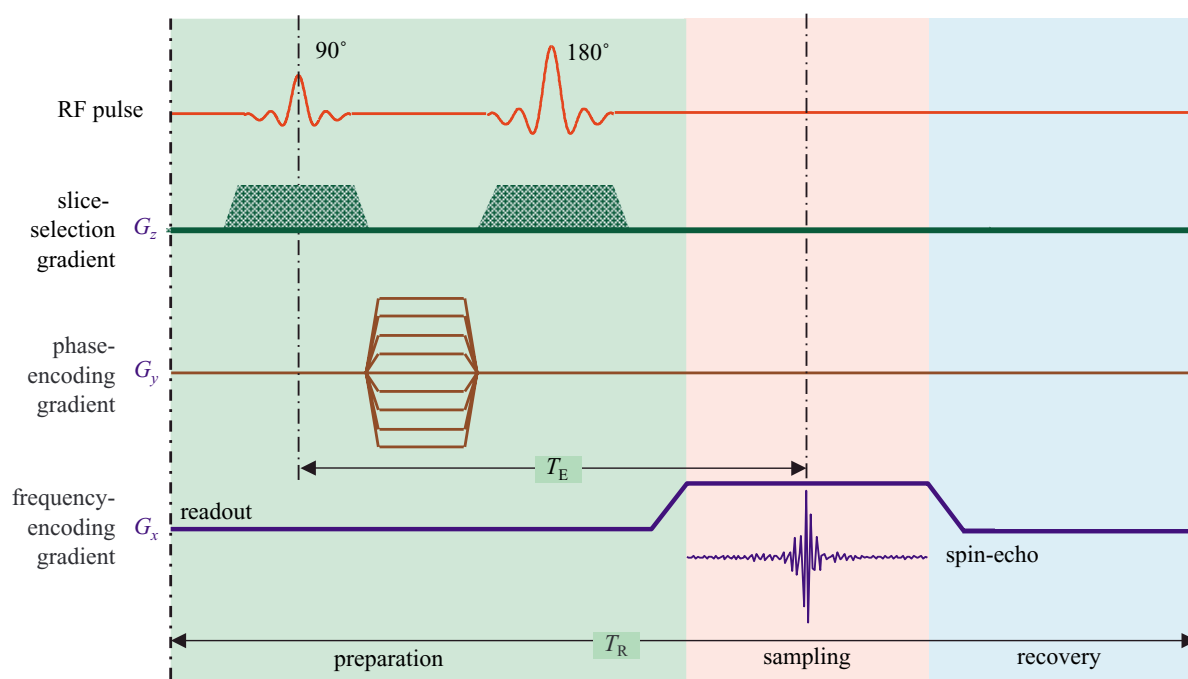
Figure 2. A highly simplified pulse sequence timing diagram. The actual pulse sequences have a number of additional compensatory gradients used to negate the dephasing caused by the slice-selection and frequency-encoding gradients. For the sake of simplicity no such additional pulses are displayed here. The pulse sequence is composed of three distinct phases: (i) the preparation of transverse magnetization; (ii) the actual data collection (sampling); and (iii) sufficient recovery of the longitudinal magnetization before the next repetition starts. In the first phase, the slice-selecting gradient (G_z) is turned on during the 90° RF pulse. The phase-encoding gradient (G_y) turns on as soon as the RF activity ceases. The spatial location of the spins along this gradient is again encoded by their frequency. But when the gradient is turned off all spins return to uniform frequency, and the spatial information is only preserved in the form of their phase angles, which remain different according to their location along the y-axis (hence the phase-encoding direction). Obviously the measured phase is the vectorial sum of all phases along the y direction. Individual phases (encoding spatial location) can be only recovered by applying phase-encoding pulses of different amplitudes during each repetition, depicted here as multiple polygons. The second RF pulse (180°) combined with a second slice-selection gradient inverts the phase of the transverse magnetization and thus generates a spin echo after time $T_E/2$. Finally, a third gradient is used to create the positional dependence of frequency during the collection of the spin echo. T_E, echo time; T_R, repetition time. G_z, G_y and G_x, the slice, phase-encoding and frequency-encoding gradients, respectively.

waveform of the haemodynamic response and the fractional change in the MR signal. Reducing the voxel size, however, while reducing the partial volume effects, affects both the SNR and the CNR of the image, thus imposing strong limitations on the image quality. Such limitations can be minimized using stronger magnetic fields and smaller RF coils.

The nominal resolution of an image can be improved by Fourier interpolation (or the mathematically equivalent 'zero filling' in k space). Typically, signals acquired with a resolution of $N_{ro}N_{pe}$ can be reconstructed as $2N_{ro}2N_{pe}$ images. This improves digital resolution by making implicit information visible to the viewer, but does not change the spatial response function of the imaging method or the image resolution according to the Rayleigh criterion.

Like the SNR and CNR, the spatial resolution of an MR image depends on a number of scan factors, including gradient strength, sampling frequency bandwidth, reconstruction method and measurement sensitivity. All other factors being optimized, the last can be greatly improved by closely matching the size, shape and proximity of an RF coil to the structure of interest, a strategy that substantially improves the SNR of the image by decreasing the noise detected by the coil. A number of different coil types have

been developed over the last few decades to achieve this, ranging from simple surface coils (Ackerman *et al.* 1980) to quadrature coil combinations (Hyde *et al.* 1987) and a phased array of several coil loops (Roemer *et al.* 1990). Further improvement of sensitivity can be obtained by using implantable, directly or inductively coupled RF coils (see § 3).

3. FUNCTIONAL MRI WITH BOLD CONTRAST

MRI, like PET, can be used to map activated brain regions by exploiting the well-established interrelation between physiological function, energy metabolism and localized blood supply. Different techniques can be employed to measure different aspects of the haemodynamic response. For example, blood-supply changes can be used in perfusion-based fMRI, that measures blood flow quantitatively. Here, I shall concentrate on a single technique exploiting the BOLD contrast which, because of its reasonably high sensitivity and wide accessibility, is the mainstay of brain fMRI studies.

The BOLD contrast mechanism was first described by Ogawa *et al.* (1990*a,b*) and Ogawa & Lee (1990) in rat brain studies with strong magnetic fields (7 and 8.4 T). Ogawa noticed that the contrast of very high resolution
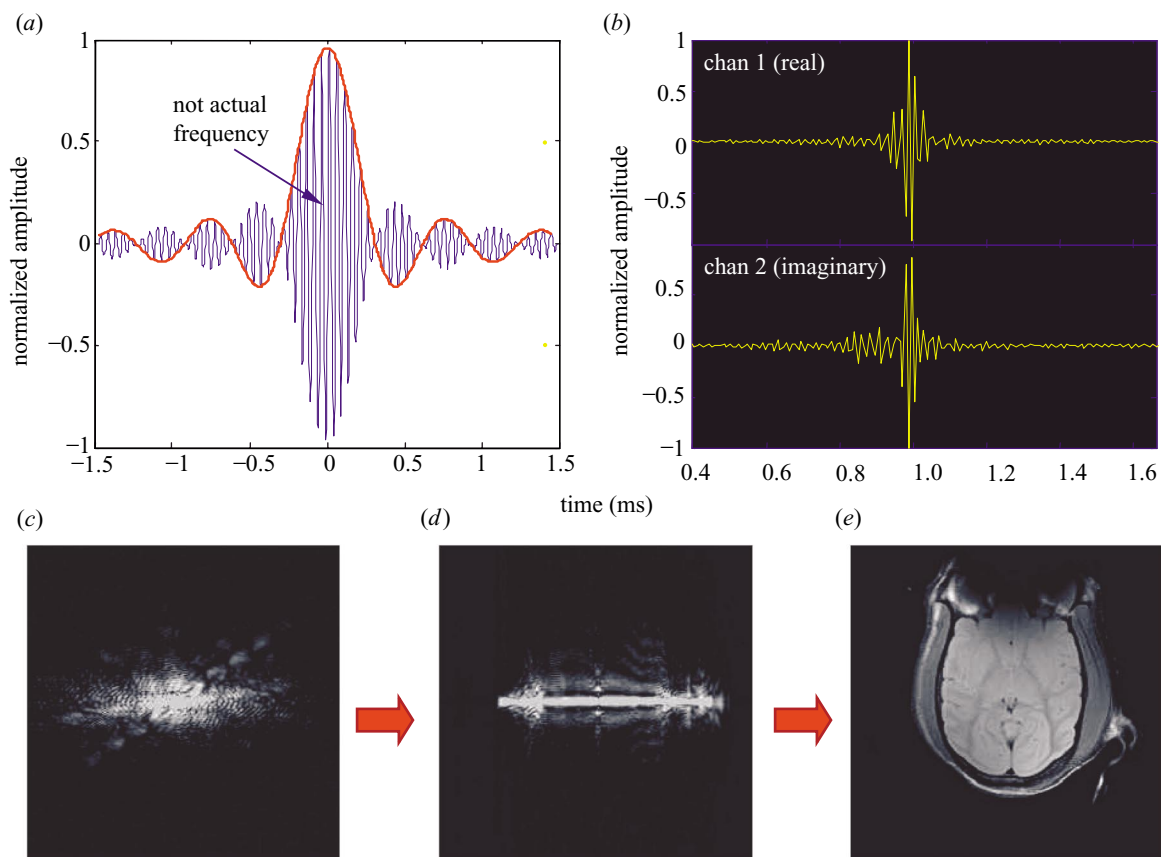
Figure 3. Image formation. (*a*) A typical RF excitation pulse (here $sinc(x) = sin(x)/x$) used to nutate the net magnetization down into the *xy* plane. The RF pulse actually consists of the product of a sine wave of the Larmor frequency with the sinc function. In the 4.7 T magnet this is *ca*. 200 MHz. The blue line depicts the sine wave at much lower frequencies for illustration purposes. $\gamma = 42.57$ MHz T^{-1}; resonance frequency = 200 MHz; duration = 3 ms; BW = 1.85 kHz. (*b*) The two spin echoes produced by an inversion pulse of 180° (see also figure 2). In MRI the initially very high RF signal (MHz range) is typically converted into an audio signal (kHz range) by comparing the RF signal with a reference signal (phase-sensitive detection). In fact, to improve SNR the signal is collected by two PSDs that are 90° out of phase (upper and lower panels of (*b*)). The converted signal is digitized and the two channels are represented as the real and imaginary part of complex numbers (alternatively they can be transformed into the magnitude and phase of the signal). Each row of the *k* space consists of a sequence of such numbers. $T_E = 15$ ms; duration = 3 ms. (*c*) Magnitude of the *k* space in a spin-echo experiment. Each row is an echo with the same frequency composition but different phase encoding. Top and bottom rows have the strongest phase-encoding gradient and hence the largest dephasing (weakest signal). The strongest echo is in the centre of the *k* space, where no phase-encoding occurs. (*d*) The first Fourier transformation along the readout direction. (*e*) The second Fourier transformation along the phase-encoding direction resulting in the actual image.

images ($65 \times 65 \times 700$ μm³) acquired with a gradient–echo–pulse sequence depicts anatomical details of the brain as numerous dark lines of varying thickness. These lines could not be seen when the usual spin-echo sequences were used, and they turned out to be image 'artefacts', signal dropouts from blood vessels (Ogawa *et al.* 1990*a*). In other words, by accentuating the susceptibility effects of dHb in the venous blood with gradient–echo techniques, Ogawa discovered a contrast mechanism reflecting the blood oxygen level, and realized the potential importance of its application by concluding that 'BOLD contrast adds an additional feature to magnetic resonance imaging and complements other techniques that are attempting to provide PET-like measurements related to regional neural activity' (Ogawa *et al.* 1990*b*). Shortly after this, the effect was nicely demonstrated in the cat brain during the course of anoxia (Turner *et al.* 1991). As is now known, the phenomenon is indeed due to the field inhomogeneities induced by the endogenous MRI contrast agent dHb.

The paramagnetic nature of dHb (Pauling & Coryell 1936) and its influence on the MR signal (Brooks *et al.* 1975) were well known before the development of MRI. Haemoglobin consists of two pairs of polypeptide chains (globin), each of which is attached to a complex of protoporphyrin and iron (haem group). In dHb the iron (Fe^{2+}) is in a paramagnetic high-spin state, as four of its six outer electrons are unpaired and act as an exogenous paramagnetic agent. When oxygenated, the haem iron changes to a low-spin state by receiving the oxygen's electrons.

The magnetic properties of dHb would be of little value if haemoglobin were evenly distributed in all the tissues. Instead, paramagnetic dHb is confined in the intracellular space of the red blood cells that in turn are restricted to the blood vessels. Magnetic susceptibility differences between the dHb-containing compartments and the surrounding space generate magnetic field gradients across and near the compartment boundaries. Pulse sequences designed to be highly sensitive to such susceptibility differences, like those used by Ogawa in his seminal studies

(Ogawa & Lee 1990; Ogawa *et al.* 1990*a*,*b*), generate signal alterations whenever the concentration of dHb changes. The field inhomogeneities induced by dHb mean that neural activity should result in a BOLD signal reduction. However, during brain activation the BOLD signal increases rather than decreasing relative to a resting level. This is because activation within a region causes an increase in CBF and the use of glucose, but not a commensurate increase in the oxygen consumption rate (Fox & Raichle 1986; Fox *et al.* 1988). This results in a decreased oxygen extraction fraction and lower dHb content per volume unit of brain tissue.

Not surprisingly, the groundbreaking work of Ogawa excited great interest in the application of BOLD fMRI to humans. MR-based CBV imaging had already been demonstrated in humans using high-speed EPI techniques and the exogenous paramagnetic contrast agent gadolinium (Belliveau *et al.* 1991; Rosen *et al.* 1991). In 1992, however, three groups simultaneously and independently obtained results in humans with the BOLD mechanism (Bandettini *et al.* 1992; Kwong *et al.* 1992; Ogawa *et al.* 1992), starting the flood of fMRI publications that have been appearing in scientific journals ever since.

Research over the last decade has established that BOLD contrast depends not only on blood oxygenation but also on CBF and CBV, representing a complex response controlled by several parameters (Ogawa *et al.* 1993, 1998; Weisskoff *et al.* 1994; Kennan *et al.* 1994; Boxerman *et al.* 1995*a*,*b*; Buxton & Frank 1997; Van Zijl *et al.* 1998). Despite this complexity, much progress has been made toward quantitatively elucidating various aspects of the BOLD signal and the way it relates to the haemodynamic and metabolic changes occurring in response to elevated neuronal activity (Kim & Ugurbil 1997; Buxton *et al.* 1998; Van Zijl *et al.* 1998).

BOLD fMRI has also been applied successfully in anaesthetized or conscious animals, including rodents (Hsu *et al.* 1998; Lahti *et al.* 1998; Bock *et al.* 1998; Tuor *et al.* 2000; Burke *et al.* 2000; Ances *et al.* 2000; Burke *et al.* 2000; Chang & Shyu 2001), rabbits (Wyrwicz *et al.* 2000), cats (Jezzard *et al.* 1997), bats (Kamada *et al.* 1999), and recently monkeys (Nakahara *et al.* 2002; Logothetis *et al.* 1998, 1999; Disbrow *et al.* 1999; Zhang *et al.* 2000; Disbrow *et al.* 2000; Vanduffel *et al.* 2001; Dubowitz *et al.* 2001). What follows describes the use of BOLD fMRI in monkeys (*Macaca mulatta*) and its combination with electrophysiological measurements in an attempt to investigate the neural basis of the BOLD response.

4. MRI OF THE MONKEY BRAIN

fMRI and microelectrode recordings are complementary techniques, providing information on two different spatio-temporal scales. The electrodes have excellent spatio-temporal resolution but very poor coverage, while fMRI has relatively poor resolution but can yield important information on a larger spatio-temporal scale. The development and application of NMR techniques (e.g. imaging, spectroscopy) for the non-human primate enables the investigation of certain levels of neural organization that cannot be studied by electrodes alone. These include the study of:

(i) long-range interactions between different brain structures;
(ii) task- and learning-related neurochemical changes by means of localized *in vivo* spectroscopy or MRS imaging;
(iii) dynamic changes in the magnitude and location of activated regions—over periods of minutes to days—with priming, learning and habituation;
(iv) dynamic connectivity patterns by means of labelling techniques involving MR contrast agents; and
(v) plasticity and reorganization following experimentally placed focal lesions.

In addition, the application of this technique to the behaviour of monkeys has the potential to build a bridge between human studies and the large body of animal research carried out over the last 50 years.

Monkeys are ideal experimental animals because a great deal is known about the organization of their sensory systems that are functionally very similar to those of humans. In addition, comparisons of psychophysical data from humans and the most commonly used species, the rhesus macaque, have revealed remarkable behavioural similarities between the two species. Thus, MRI in monkeys not only provides insights into the neural origin of the fMRI signals, but it can do so in the context of different types of behaviour. With this conviction, we set out to develop and apply MRI (and MRS) in monkeys, using both conventional volume coils for whole-head scanning and implanted coils allowing imaging with high spatial resolution.

Figure 4 shows the system used for imaging the monkey brain. It is a vertical 4.7 T scanner with a 40 cm diameter bore (Biospec 47/40v; Bruker Medical Inc., Ettlingen, Germany). The scanner is equipped with a 50 mT m^{-1} (180 μs rise time) actively shielded gradient coil (Bruker, B-GA 26) of 26 cm inner diameter. A primate chair and a special transport system were designed and built to position the monkey inside the magnet (Logothetis *et al.* 1999). Whole-head scans were carried out with either linear birdcage-type coils or with custom-made linear homogeneous saddle coils. For high-resolution fMRI, we used customized small RF coils (see § 4*b*) which had been optimized for increased sensitivity over a given ROI (Logothetis *et al.* 2002). In the combined physiology and fMRI sessions (see § 5*a*), the coils were attached around the recording chamber and were used as transceivers (Logothetis *et al.* 2001).

(a) *Large FOV imaging: volume coils*

This section introduces a few applications with volume, whole-head coils that demonstrate the value of the technique for research involving:

(i) the comparison of monkey and human sensory systems;
(ii) microelectrode recordings from different sites of distributed neural networks subserving a behaviour under investigation; or
(iii) the planning of selective focal brain lesions in the context of investigations into behavioural disorders to illuminate the role of a particular brain region.

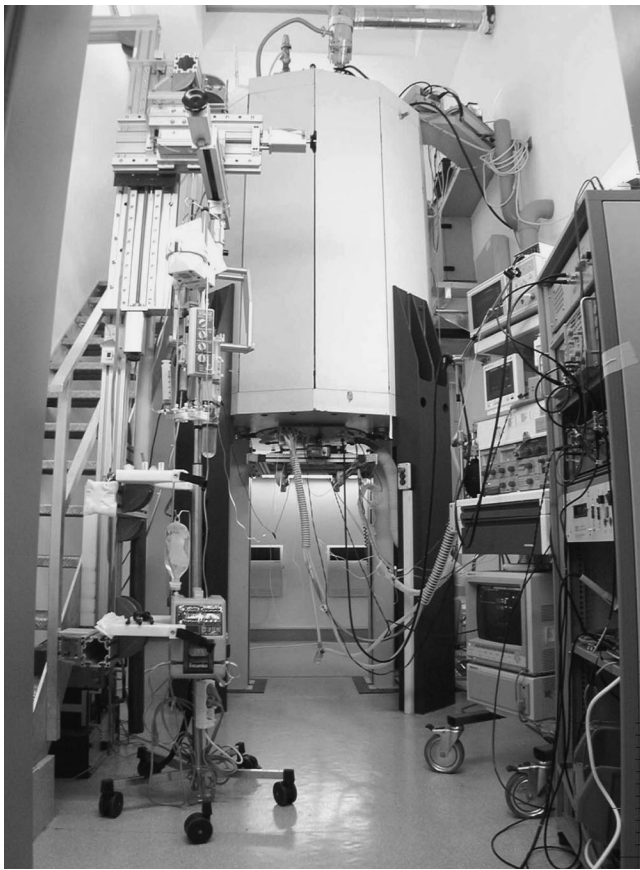Details on these applications can be found in various

Figure 4. The scanner system. A vertical 4.7 T magnet with a 40 cm diameter bore was used to image monkey brains. The magnet has local passive shielding to permit the use of neurophysiology and anaesthesia equipment. It is equipped with a 50 mT m^{-1} (180 µs rise time) actively shielded gradient coil (Bruker, B-GA 26) with an inner diameter of 26 cm. A primate chair and a special transport system were designed and built for positioning the monkey within the magnet.

recent publications (Logothetis *et al.* 1999; Rainer *et al.* 2001; Tolias *et al.* 2001; Brewer *et al.* 2002; Sereno *et al.* 2002).

(i) *Activation of the thalamus and visual cortex*

Figure 5 shows the results from a macaque monkey scanned under isoflurane (0.4%) anaesthesia (Logothetis *et al.* 1999). The left half of the figure depicts typical *z*-score maps for 12 horizontal slices. No threshold was applied to the statistical maps so that one can directly see the strength of the difference signal and its relationship to noise. On the right half, thresholded *z*-score maps showing brain activation are colour coded and superimposed on anatomical scans as slices of the computer-rendered monkey head. The activation was elicited by a polar-transformed checkerboard pattern rotating in alternating directions.

Figure 5*a,b* shows a robust BOLD signal in the LGN as well as in the striate and extrastriate cortices. The anatomical scan was acquired with an FOV of 128 mm × 128 mm with a matrix of 256 × 256 and slice thickness of 0.5 mm using the three-dimensional MDEFT (Ugurbil *et al.* 1993) pulse sequence. The fMRI was carried out by multi-slice (13 slices, 2 mm thick), multi-shot

(eight segments) gradient-recalled EPI, with an FOV of 128 mm × 128 mm on a 128 × 128 matrix and a voxel size of 1 mm × 1 mm × 2 mm.

(ii) *Retinotopy*

The robustness of activation and the spatial selectivity of the BOLD signal can be examined by exploiting the well-established retinotopic organization of the visual system. In humans, retinotopy can be reliably demonstrated in fMRI by using slowly moving, phase-encoded retinotopic stimuli (Engel *et al.* 1994, 1997; Deyoe *et al.* 1994; Sereno *et al.* 1995).

We have used the same approach to study the retinotopical organization of the monkey visual areas. As in human studies, the stimuli consisted of a series of slowly rotating wedges or expanding rings, each wedge or ring being a collection of flickering squares (Engel *et al.* 1994, 1997; Wandell *et al.* 2000). The ring typically begins as a small spot located at the centre of the visual field and then grows until it travels beyond the edge of the stimulus display. As it disappears from view, it is replaced by a new spot starting at the centre. Such an expanding stimulus causes a travelling wave of neural activity beginning a couple of millimetres posterior to the lunate sulcus (figure 6*a,b*) and travelling in the posterior direction toward the pole of the occipital lobe. The temporal phase of the MRI signal varies as a function of eccentricity, and this phase can be used to generate the eccentricity maps shown in figure 6*c* (adapted from Brewer *et al.* (2002)). This technique made it possible to identify the boundaries between visual areas V1, V2, V3 and V4 and V5 (MT) and to measure the visual-field eccentricity functions that reveal the distribution of foveal and peripheral signals within the ventral and dorsal streams, respectively (Wandell *et al.* 2000; Brewer *et al.* 2002). The maps obtained in this manner are in excellent agreement with those derived from monkeys with anatomical and physiological techniques, and they can be used to study the process of cortical reorganization after deafferentiation (e.g. Kaas *et al.* 1990; Darian-Smith & Gilbert 1995; Das & Gilbert 1995; Obata *et al.* 1999). Such applications demonstrate the quality of data that can be obtained in the monkey, and the feasibility of a direct comparison between human and non-human primate studies.

(b) High-spatial resolution imaging: surface coils

Whole-head imaging, although of great importance for the localization of activations, is of limited value when very high spatio-temporal resolution is required to study cortical microarchitecture or to compare imaging with electrophysiology. We have therefore adapted and optimized the implanted coil technique for monkeys. Very high-resolution structural and functional images of the monkey brain were obtained with small, tissue-compatible, intra-osteally implantable RF coils. Voxel sizes as small as 0.012 µl (125 × 125 × 770 µm^3) were obtained with high values of the SNR and CNR, revealing both structural and functional cortical architecture in great detail.

(i) *Implanted RF coils*

As mentioned in § 2b, the RF system is a transceiver system used both to generate the alternating B_1 field and to receive the RF signal transmitted by the tissue (for a
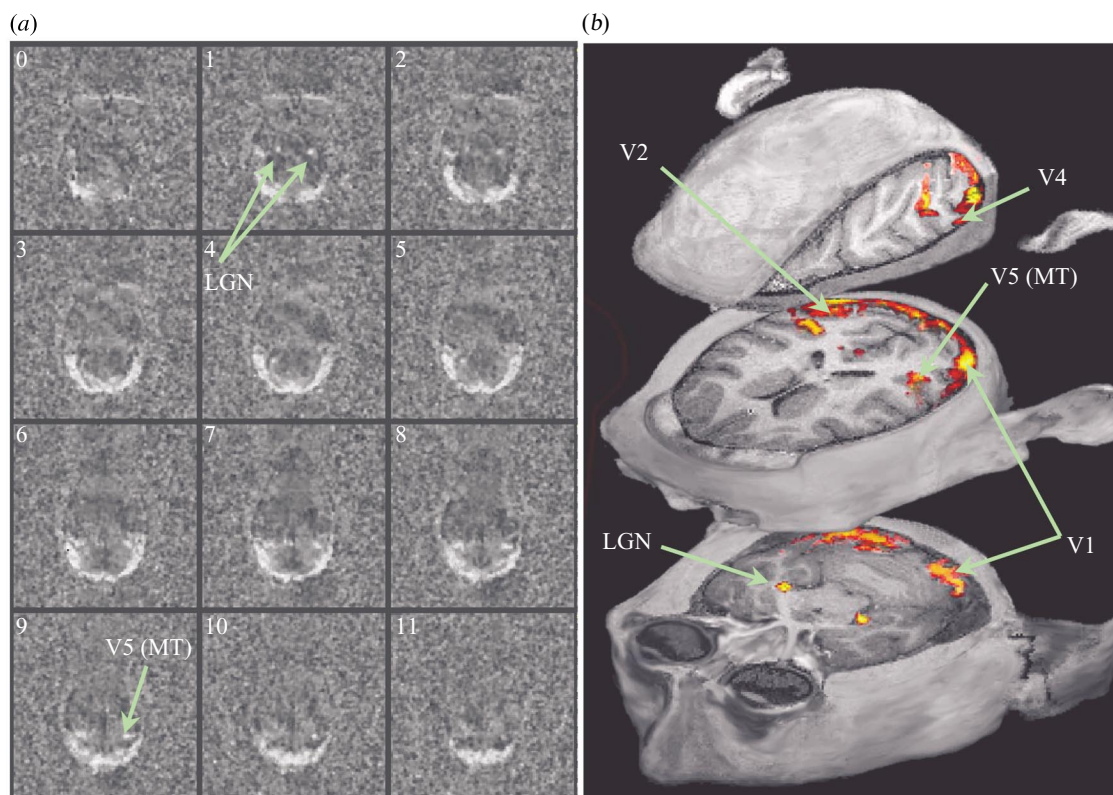
Figure 5. (*a*) BOLD activation shown in terms of *z*-score maps. The specificity of the signal enables the visualization of anatomical details in the occipital lobe. (*b*) Activation maps superimposed on anatomical three-dimensional MDEFT scans (0.125 µl voxel size). The figure shows activation of the LGN, striate and some extrastriate areas including V2, V3, V4 and V5 (MT). V1 activation covers almost the entire representation of the perifovea (the horizontal extent of the checkerboard stimulus was 30°). The V1 regions showing high activation (yellow) lie within the cortical representation of the fovea.

review on principles and instrumentation see Vlaardinger-broek & Den 1996; Wood & Wehrli 1999; Matwiyoff & Brooks 1999). It is typically an integral part of any imaging system, and is delivered with the magnet and all the other components of a scanner. However, coils can also be custom made in all kinds of different designs to accommodate the needs of specific experiments. They can be used as transceivers, but also as transmit- or receive-only units, the former transmitting the B_1 field and the latter receiving the FID after an adjustable delay.

Technically, RF coils are equivalent to an electrical circuit with inductance (L), capacitance (C) and resistance (R), and are tuned to a specific resonance frequency (ω) (e.g. 200 MHz at 4.7 T); for MRI this is the precessional frequency of the nuclear spin moments. Optimizing a coil commonly involves increasing its quality factor (or filling factor), Q. The latter is defined as the maximum energy stored divided by the average energy dissipated per radian, and can be improved by fine tuning the parameters L and C and minimizing R (the smaller the resistance, the sharper the resonance curve) for any given frequency. The RF coil design can be optimized (i) for signal homogeneity over the whole brain, (ii) for increased sensitivity over a given ROI, an example being the large quadrature surface coils, or (iii) for very high-resolution studies of a small area of interest (surface coils).

Small surface coils are often used in either human or animal studies to provide the highest possible SNR and to allow the use of small voxel sizes in high-resolution imaging (e.g. McArdle *et al.* 1986; Le *et al.* 1987; Rudin

1987; Garwood *et al.* 1989; Gruetter *et al.* 1990; Walker *et al.* 1991; Merkle *et al.* 1993; Hendrich *et al.* 1994; Lopez-Villegas *et al.* 1996). The SNR of such coils can be further increased by geometrically matching the coil to a specific tissue region. Finally, in animal experiments, the SNR can be substantially increased by implanting the coils in the body (Farmer *et al.* 1990; Summers *et al.* 1995; Silver *et al.* 2001). Implanted coils bring about a substantial increase in both the SNR and spatial selectivity by effectively improving the filling factor of a reception coil. The measured signal typically decreases as the distance of the coil from the ROI increases, while the noise detected by a coil increases with coil size. Thus, the smaller the coils and the closer the area of interest, the better the obtained signal.

The small RF surface coils described here were implanted intraosteally. They were made of 2 mm thick, Teflon-insulated, fine silver wire and had diameters varying from 18 to 30 mm. The implantable coils were 15 or 22 mm in diameter (see figure 7). Their electronic circuitry had non-magnetic (copper–beryllium) slotted tubes to ensure a reliable electrical connection. During the surgical placement of the implanted coils, special care was taken to optimize the loaded Q of the coils. The Q factor can be directly affected by placing the coil too far from—but also too close to—the ROI. The appropriate distance of the coil from the ROI was therefore calculated based on models of the brain and skull surfaces created from anatomical scans.
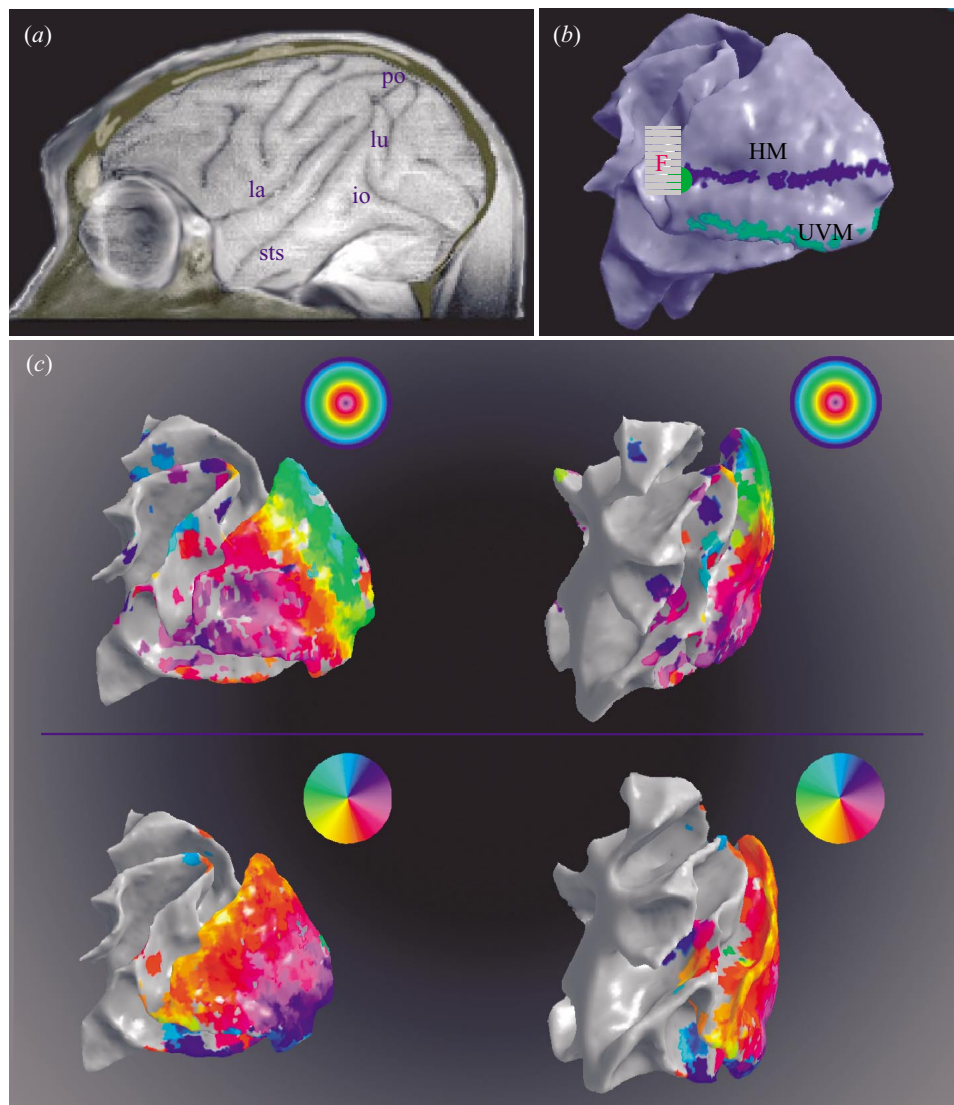
Figure 6. Retinotopic organization revealed with fMRI. (*a*) Lateral view of a computer-rendered monkey brain. It shows some of the primary sulci. (*b*) Latero-caudal view of the posterior part of the brain with opened-up sulci. It shows the fovea and the horizontal and vertical meridians as determined with phase-encoding stimuli. (*c*) The upper panels show the eccentricity maps and the lower panels the orientation maps generated by using expanding-ring and rotated-wedge stimuli, respectively. Abbreviations: la, lateral; sts, superior temporal; io, inferotemporal, lu, lunate; po, parieto-occipital; HM, horizontal meridian; UVM, upper vertical meridian; F, foveal representation.

(ii) *High-resolution echo-planar BOLD imaging*

Figure 8 shows anatomical and functional scans acquired with an implanted surface coil. Figure 8*a* is an example of a T_2^*-weighted echo planar (EP) image obtained with an actual resolution of $125 \times 125 \ \mu m^2$ and a slice thickness of $720 \ \mu m$. The contrast sensitivity of the image is sufficient to reveal the characteristic striation of the primary visual cortex. The dark line shown by the white arrow (Gen) is the well-known, *ca.* $200 \ \mu m$ thick Gennari line between the cortical layers IVA and IVC, a result of the axonal plexus formed by the axons of pyramidal and spiny stellate cells contained in IVB. It appears dark in T_2^*-weighted images because the plexus contains a large number of horizontally arranged, myelinated (the T_2-values are shorter for fat; see § 2b(ii)) axons from collaterals, horizontal axonal branches, and ascending ramifications of spiny stellates.

Also visible in figure 8*b* are the small cortical blood vessels that are known to vary in their degree of cortical pen-

etration. Cortical vessels, that were traditionally divided into three groups (short, intermediate and long), were further divided by Duvernoy *et al.* (1981) into six groups according to their length and termination in the various cortical layers. The green arrows show two vessels of Group 5 according to Duvernoy *et al.* (1981) consisting of arteries and veins (the MR images show the veins) that pass through the entire cortical thickness and vascularize both cortex and the adjacent WM (figure 5*c*,*d*). Measurements after methyl methacrylate injections show that the veins of this group have an average diameter of $120 \ \mu m$. The actual resolution of the presented image permits the visualization of susceptibility effects produced by such tiny vessels.

Figure 8*e* shows fMRI correlation coefficient maps (in colour) superimposed on the actual EPI (T_2^*-weighted) images of a monkey during visual block-design stimulation. The sections are around the lunate sulcus, and activation extends into the primary and secondary visual
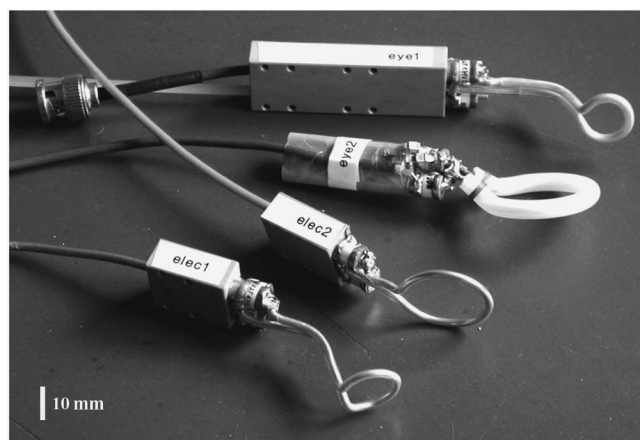
Figure 7. Implantable RF coils. The coils were made of insulated silver wire and were used either as transceivers or receive-only units. All circuits were equipped with non-magnetic (copper–beryllium) slotted tubes to ensure reliable connection with the silver-wire loops.

cortices (V1 and V2, respectively). The images have high SNR (27:1 for an ROI of 36 voxels, measured for an ROI positioned over the high-signal-intensity region in the image) and CNR (21:1 and signal modulation ranging from 2 to 7%, averaged for ROI of *ca.* 15–24 voxels). Both robust activation and good anatomical detail can be discerned.

(iii) Spatial specificity of BOLD fMRI

Gradient echo sequences like those used extensively for BOLD imaging are sensitive to both small and large vessels (Weisskoff *et al.* 1994). The significant contribution of the large vessels can lead to erroneous mapping of the activation site, as the flowing blood will generate BOLD contrast downstream of the actual tissue with increased metabolic activity. Thus, the extent of activation will appear to be larger that it really is. The contribution of large vessels depends on both field strength and the parameters of the pulse sequences (Boxerman *et al.* 1995*a*; Zhong *et al.* 1998; Hoogenraad *et al.* 2001).

Large vessels can be de-emphasized using pulse sequences designed to suppress higher flow velocities (Boxerman *et al.* 1995*a*). They are also de-emphasized in stronger magnetic fields, because the strength of extra-vascular BOLD increases more rapidly for small vessels than it does for large ones. More specifically, the transverse relaxation rate, R_2^*, increases linearly with the external magnetic field for large vessels (larger than 10 μm) but varies as the square of the field for small vessels (Ogawa *et al.* 1993; Gati *et al.* 2000). Thus, with sufficient SNR, signals originating from the capillary bed are clearly discernible in strong magnetic fields.

A loss of specificity can also result from so-called inflow effects. Both supplying pial arteries and draining vessels unavoidably bring fresh spins into the area of interest during the inter-image delay. For instance, when short repetition times are used, gradient–echo sequences yield considerable contrast between the partially saturated tissues in the imaging plane, i.e. tissues whose longitudinal magnetization was not yet fully recovered, and the unsaturated blood flowing into this plane (Axel 1984, 1986). In the same vein, increased CBF in an activated tissue will

lead to signal enhancement in the image of a selected slice if the time between consecutive RF excitations is insufficient for the signal within the slice to reach full relaxation. Such inflow effects can be considerably stronger than the BOLD signal itself (Segebarth *et al.* 1994; Frahm *et al.* 1994; Kim *et al.* 1994; Belle *et al.* 1995) and much less tissue specific. The shorter the repetition times, the stronger the inflow effect will be (Glover & Lee 1995; Haacke *et al.* 1995). Inflow effects can be eliminated by utilizing low flip angles and increasing the T_R time (Menon *et al.* 1993; Frahm *et al.* 1994).

Assuming the appropriate selection of pulsing parameters to minimize the above-mentioned effects, the issue of spatial specificity can be addressed by conducting specific experiments targeted at mapping functionally distinct structures with well-defined organization and topography in the brain. The activation of LGN shown in figure 5 is an example of such specificity, as the structure is only *ca.* 6 mm in the rostrocaudal, and *ca.* 5 mm in the dorsoventral and mediolateral directions.

Figure 9 demonstrates the spatial specificity of BOLD by exploiting the non-uniform distribution of directionally selective cells across the layers of the striate cortex. About one-third of the striate cells are known to be directionally selective (Goldberg & Wurtz 1972; Schiller *et al.* 1976; De Valois *et al.* 1982; Albright 1984; Desimone & Ungerleider 1986; Colby *et al.* 1993). However, these cells do not exhibit a uniform laminar distribution. Instead, most are found in layers 4A, 4B, 4Cα and 6 (Dow 1974; Hawken *et al.* 1988). In high-field MRI such differences in neuron density can be visualized if the appropriate visual stimuli are used and the pulsing parameters are tuned to stress the extravascular BOLD signals. Figure 6*a*,*b* shows the *z*-score maps obtained by comparing the activation elicited by the moving checkerboard stimulus to that elicited by the blank screen and the counter-flickering checkerboard stimulus, respectively (Logothetis *et al.* 2002). The parameters used in this scan were: FOV = 32 mm × 32 mm on a matrix of 256 × 256 voxels (0.125 mm × 0.125 mm resolution), slice thickness = 1 mm, T_E/T_R = 20/750 ms, and number of segments = 8. Figure 9*c* illustrates the plane of the slice selected for high-resolution imaging and figure 7*d* illustrates the signal modulation. For the most part, activity in V1 was found in the middle layers, usually layer IV. This activity may indeed reflect the density of active directional neurons within this lamina. However, it is possible that the activation in the middle layers of cortex reflects the highest capillary density that occurs at approximately layers 3C, 4 and 5 (vascular layer 3 as defined by Duvernoy *et al.* (1981)). A recent human fMRI study indicates that the origin of the BOLD signal may actually be the vascular layer 3, presumably extending into adjacent vascular layers (Hyde *et al.* 2001). Further experimentation is needed to dissect the effect of vascular density from that of neural specificity.

(c) High-temporal resolution imaging

In order to compare imaging with physiology we used a rapid scanning protocol to acquire a single slice containing the microelectrode tip (GR-EPI with four segments and T_E/T_R = 20/250 ms). To minimize the effects of inflow and large drainage vessels, we consistently used flip angles

that were smaller than the computed Ernst angle (see § 4b) by 10°. Modelling the haemodynamic response requires an understanding of the role of noise and its sources.

In imaging, different types of disturbances can interfere with the time-course of the haemodynamic response. In fact, EPI is one of the sequences most sensitive to disturbance, and various artefacts easily degrade EP images. Signal fluctuations are often related to physiological motion or general physiological state changes. They can also be of subtle origin, including minute fluctuations within the environment such as small changes in air pressure or temperature that by themselves are already sufficient to slightly alter the resonance frequency, phase or magnitude of the signal and prevent reproducible results in high resolution, time-resolved functional imaging. One way to reduce such artefacts is to use a technique based on 'navigator' echoes. This approach was initially used in conventional spin-echo imaging of moving structures (Ehman & Felmlee 1989) to reduce motion artefacts, and was subsequently adopted by a number of investigators (Hu & Kim 1994; Kim *et al.* 1996; Glover & Lai 1998; Pfeuffer *et al.* 2002*a*) employing susceptibility-weighted fMRI.

'Navigator' FIDs or echoes can be acquired to obtain information on a number of parameters (e.g. resonance frequency, global amplitude or phase). In our implementation with the Bruker Biospec system, for instance, the navigator echoes were two gradient echoes that were sampled with a positive and a negative readout gradient at the beginning of each acquisition. They were immediately followed by the acquisition of the phase-encoded gradient–echo train (i.e. a set of k space lines). The navigator FID was used for amplitude and frequency correction and the two navigator echoes were used for image deghosting (i.e. removing distortions in the phase-encoding direction). Additional ways to improve the image include corrections of direct current offset and equidistant sampling during the gradient-switch (transient) periods. The latter source of distortion originates in the way echoes are acquired in gradient-recalled MRI. More specifically, the digitization of the EPI gradient–echo sequence is done at equidistant time intervals, even while the read gradient is ramping to the desired strength. The data points acquired during ramping do not span a constant area, and therefore some correction is usually needed to achieve equidistant sampling in the k space. Finally, an important source of variability in EP imaging comes from physiologically induced global off-resonance effects. Typically, respiratory and cardiac pulsations—just like instrument instabilities—may introduce NMR phase shifts that may cause variation in the signal's amplitude as well as shifts (ghosting) between segments; such artefacts can be detected and also corrected with navigator echoes either directly in the k space (Pfeuffer *et al.* 2002*a*) or in the spatial domain.

The effects of all these corrections on the time-course of the BOLD signal are presented in figure 10*a*, that shows the average of haemodynamic responses from a single voxel (0.5 mm × 0.5 mm × 2 mm) to 14 stimulus (rotating checkerboards) presentations. The variability of the response can be seen in the standard deviation bars plotted for every other image.

The onset of the stimulus-induced haemodynamic response plotted in figure 10*a* was delayed by about 2 s,

which is consistent with previous studies (Kwong *et al.* 1992). This is the time that it takes blood to travel from arteries to capillaries and draining veins. The haemodynamic response reached a plateau in 6–12 s and returned to the baseline with a similar ramp, although often a prolonged poststimulus undershoot was evident (Frahm *et al.* 1996; Kruger *et al.* 1996; Buxton *et al.* 1998; Logothetis *et al.* 1999). It is thought that the time-course of the haemodynamic response is determined by an initial increase in oxygen consumption that alters the dHb-to-oxyhaemoglobin ratio (Malonek & Grinvald 1996), followed by an increase in CBF that overcompensates for the oxygen extraction, so that an oversupply of oxygenated blood is delivered (Fox & Raichle 1986; Fox *et al.* 1988). This oversupply underlies the signal increase typically observed in BOLD fMRI (positive BOLD). Figure 10*a* shows an example of positive BOLD for the time-series of a single voxel, averaged over 14 repetitions. Small changes in metabolism require a disproportionately large oversupply because the passive diffusion-driven oxygen extraction from the blood is less efficient at higher flow rates (Buxton & Frank 1997; Hyder *et al.* 1998). The increased flow causes vasodilation because of the balloon-like elasticity of the venules and veins, resulting in an increase in venous blood volume (Buxton *et al.* 1998; Mandeville *et al.* 1999*a,b*). This volume increase is thought to lie at the root of the poststimulus undershoot described in § 4c.

Occasionally, a small decrease in image intensity below the baseline was observed immediately after the stimulus onset. Figure 10*b* illustrates this initial 'dip' for the time-series of a voxel (14 repetitions). This kind of dip has been reported in MRS experiments (Ernst & Hennig 1994) and in BOLD fMRI in humans, rats, cats and monkeys (Menon *et al.* 1995; Jezzard *et al.* 1997; Hu *et al.* 1997; Yacoub & Hu 1999; Logothetis *et al.* 1999). Optical imaging studies indicate that the initial dip reflects the early oxygen consumption, so it should be closely correlated with the metabolic demand in the parenchyma, and hence more closely related to the neuronal activity than the other components of the haemodynamic response (Malonek & Grinvald 1996; Malonek *et al.* 1997; Vanzetta & Grinvald 1999; Jones *et al.* 2001).

In a series of experiments conducted in my laboratory, we have investigated the time-course of the BOLD signal using a fast scanning protocol ($T_R/T_E = 250/20$ ms). The probability of seeing the initial dip in a single voxel at least once in 50 repetitions was found to be approximately 0.3. This variability is probably due to physiological noise. Haemodynamic responses depend not only on magnetic susceptibility but also on blood volume and flow, each of which can be selectively evaluated by various methods (Frahm *et al.* 1996; Kruger *et al.* 1996; Kim & Ugurbil 1997; Kennan *et al.* 1997; Bandettini *et al.* 1997; Davis *et al.* 1998; Mandeville *et al.* 1999*b*; Marota *et al.* 1999; Lee *et al.* 2001; Mandeville *et al.* 2001). All in all, with such sensitivity, the initial dip seems to be an extremely unreliable BOLD component for use in studies of cortical microarchitecture, a fact that explains the controversy between different investigators (Marota *et al.* 1999; Logothetis 2000; Kim *et al.* 2000; Buxton 2001; Vanzetta & Grinvald 2001; Mayhew *et al.* 2001; Lindauer *et al.* 2001; Cannestra *et al.* 2001).
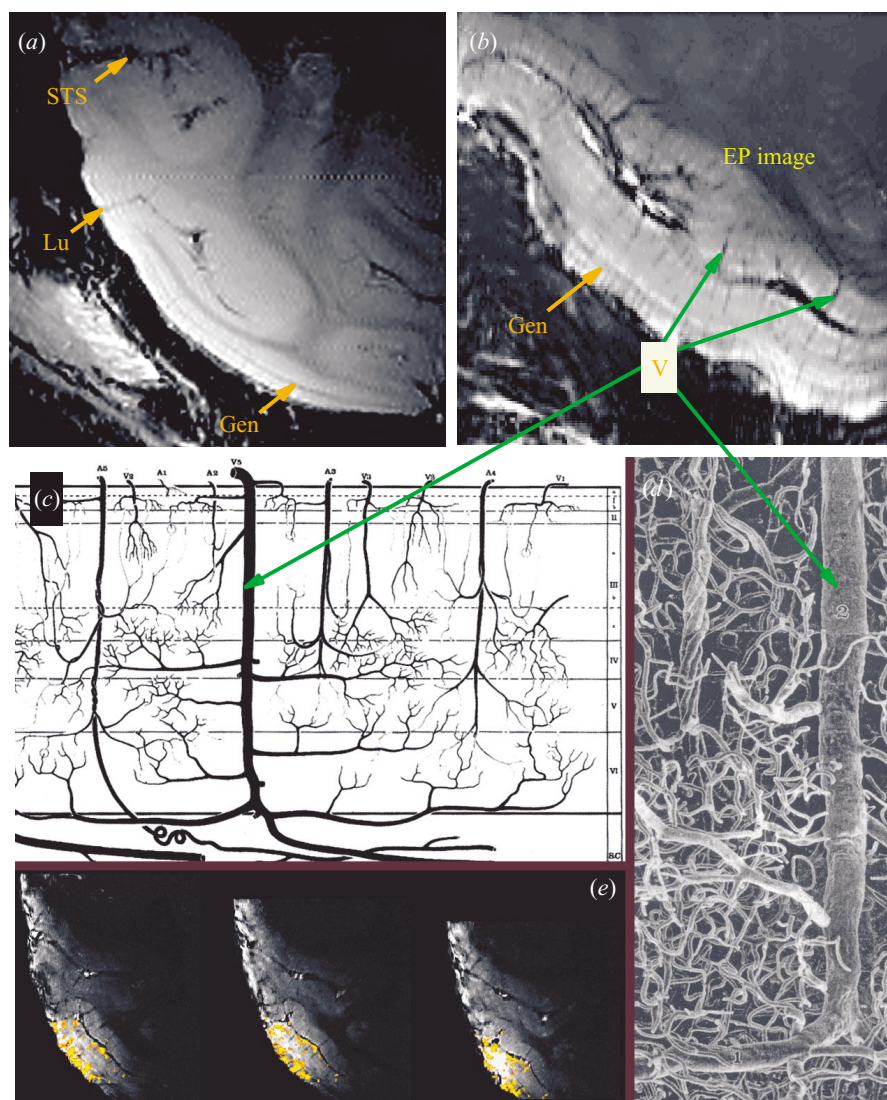
Figure 8. Anatomical and functional scans acquired with an implanted surface coil. (*a*) T_2^*-weighted EP image obtained with an actual resolution of $125 \times 125 \ \mu m^2$ and a slice thickness of 720 μm. (*b*) The resolution permits visualization of susceptibility effects produced by small cortical vessels with an average diameter of 120 μm. (*c*,*d*) Schematic and microphotograph of cortical vessels (see § 4b(ii)). (*e*) fMRI correlation coefficient maps (in colour) superimposed on the actual EPI (T_2^* weighted) images during visual block-design stimulation. Abbreviations: Gen, Gennari line; V, cortical vessels; Lu, Lunate sulcus; STS, superior temporal sulcus. Figure parts (*c*) and (*d*) from Duvernoy *et al.* 1981, with permission.

The BOLD response is not always 'positively correlated' to the stimulus time-course the way it has been described so far. Negative signals (anti-correlations) like those shown in figure 10*c* have also been observed and were reported in previous studies (Kennan *et al.* 1998; Martin *et al.* 1999). In our studies, we often found a negative BOLD response that was perfectly anti-correlated with the positive BOLD response, all the way to the undershoot component (see figure 10*c*). A negative BOLD signal was seen exclusively in cortical regions that were not stimulated by the visual stimulus (e.g. a peripheral visual field beyond the extent of the stimulus). Retinotopy experiments in humans also systematically demonstrate the existence of negative BOLD (B. Wandell, personal communication), the origin of which is currently under extensive physiological investigation.

As a final point, temporally resolved fMRI is only useful for physiological studies if the images also have a high spatial resolution. In EPI, for a given spatial resolution, the acquisition time is proportional to the FOV in the phase-encoding direction, i.e. to the number of *k* space lines. Multi-shot or *segmented* acquisition that affords better SNR and thus promises higher spatial resolution, decreases the temporal resolution by increasing the image acquisition time. It is therefore important to apply methods that use an FOV as small as the potential volume of interest. Reducing the FOV, on the other hand, causes signals outside the FOV to fold back into the image in the phase-encoding direction. Recently, a special outer-volume suppression technique was successfully employed to achieve B_1-insensitive suppression in the inhomogeneous RF field of a surface coil (Luo *et al.* 2001). This technique, combined with zoomed imaging that minimizes imaging time by reducing the FOV (Pfeuffer *et al.* 2002*b*), promises to be of great value in combined physiology and imaging experiments.
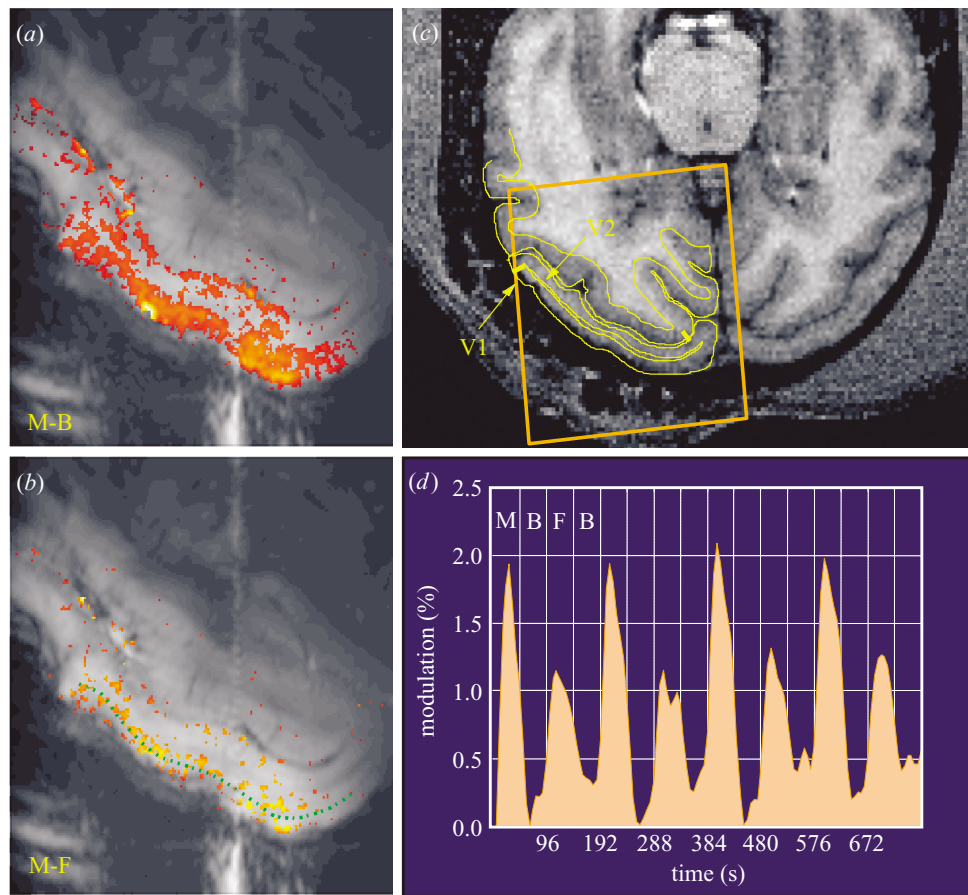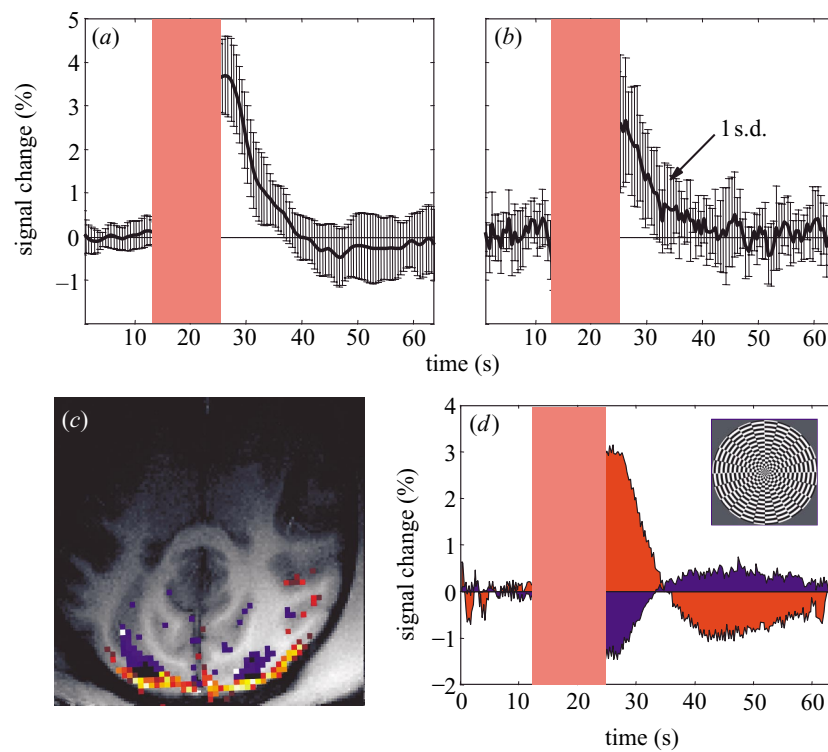
Figure 9. (*Legend overleaf.*)

Figure 10. (*Legend overleaf.*)

Figure 9. Lamina-specific activation. (*a*) *z*-score maps obtained by comparing the activation elicited by the moving stimulus with that elicited by the blank screen. (*b*) *z*-score maps obtained in the same ROI by comparing the responses to the moving stimuli with those elicited by flickering stimuli. The green dashed line corresponds approximately to the layer 4. (*c*) Axial slice showing the ROI studied with the surface coil. The orange square is the region shown in (*a*) and (*b*). It also depicts the position of V1 and V2. (*d*) Signal modulation for all four repetitions of an observation period for all significantly activated voxels colour coded in (*b*). M-B, motion vs blank screen; M-F, motion vs counter-phase flicker; MBFB, motion, blank, flicker, blank etc.

Figure 10. (*a*) Time-course of the typical 'positive' BOLD signal. Bars denote standard deviation. The trace is the average of 14 time series of the same voxel. (*b*) The initial dip (see § 4*c*), 14 averages of a single voxel. (*c*) *z*-score map showing areas with negative BOLD. (*d*) The time-course of the two—correlated and anticorrelated—BOLD responses.

5. COMBINED fMRI AND MICROELECTRODE RECORDING

The success of fMRI ultimately depends on a comprehensive understanding of the relationship between the fMRI signal and the underlying neuronal activity. A number of studies in humans and animals have already combined fMRI with EEG (Menon *et al.* 1997; Krakow *et al.* 1999; Bonmassar *et al.* 1999; Krakow *et al.* 2000) or optical imaging recordings of intrinsic signals (Hess *et al.* 2000). But optical imaging also measures haemodynamic responses (Bonhoeffer & Grinvald 1996) and thus can offer very little direct evidence of the underlying neural activity, while EEG studies typically suffer from poor spatial resolution and relatively imprecise localization of the electromagnetic field patterns associated with neural current flow. Microelectrode recordings, however, can directly measure the activity of small neural populations, and have been used extensively to obtain data about the central nervous system in both anaesthetized and alert, behaving animals. Simultaneous electrophysiological and imaging experiments are a promising method that should reveal a great deal about the nature of the fMRI BOLD signal.

(a) *Microelectrode recording in the presence of strong magnetic fields*

Certain hardware, including novel electrode types and signal conditioning equipment, had to be developed before it was possible to conduct electrophysiological measurements during the MR image acquisition. Details have been given elsewhere (Logothetis *et al.* 2001). Briefly, the generation of an MR image involves a strong alternation of field gradients (see § 2*b*(iii)). Such alternations induce voltages in any existing loop in the circuit of electrophysiology equipment placed within the magnet. Conventional shielding reduces electrical interference but is ineffective against magnetic interference, while materials like μ-metals that attenuate magnetic interference contain iron, affecting the field homogeneity. Furthermore, the

low-noise, low-frequency voltage amplifiers typically used in neurophysiology rectify high-frequency voltage signals coupled with the input signal, an effect that occurs at all stages of their integrated circuits. In a 4.7 T magnet, for instance, amplifiers rectify the 200 MHz RF excitation pulses, resulting in a substantial disturbance of the output that only recovers several tens of milliseconds after the RF signal has subsided. Alternatively, simply placing the preamplifiers outside the gradient tube is not a solution, because the electrode impedance and the capacitance of the long (more than 2 m) cable necessary to connect the electrode to that preamplifier would act as a voltage divider and compromise the signal.

To avoid signal loss due to increased cable length, we developed a method of measuring current instead of voltage that is insensitive to the cable length. Current flow from the electrode tip was measured over a cable long enough to permit the placement of preamplifiers outside the gradient coil, and was then converted into voltage at the input stage of the amplifier. In addition, we identified and compensated for the interference introduced by the gradient alternation. Interference during imaging originated from sources located at a distance greater than that from the electrode tip to the electrode ground (far interference) and from the immediate vicinity of the electrode tip (near interference). The first is due to the metal-to-electrolyte interface present whenever the animal is capacitively connected to any metal contact, including connections to the ground and electrode; the latter originates and acts in the vicinity of the electrode tip or within the electrode holder and the cables primarily because of eddy currents. Near interference required the measurement of local magnetic field changes by means of three small, identical, orthogonally oriented coils positioned near the electrode. The two types of interference compensations ultimately permitted the collection of denoised neural data.

The denoising procedures described in the previous paragraph ensure a non-saturated, measurable signal which, however, may be still contaminated with a certain amount of gradient interference. By using the principal component analysis technique and by reconstructing the signal after excluding those components that best correlated with the directly recorded interference, we were able to isolate the neural signal. Figure 11 illustrates the procedure of interference removal. Figure 11*a* shows the recorded gradient currents of the three gradients, and figure 11*b*, upper trace shows the summed signal that induced the voltages depicted by the middle trace of figure 11*b*. The pattern of interference shown in the middle trace was approximately the same for each acquired image segment. The data were therefore initially realigned to the slice-selection pulse (signifying the beginning of collection of an image of a single *k* space segment for single- or multi-shot acquisitions, respectively), and subsequently reshaped into an $N \times M$ matrix, where N was the number of segments and M was the number of data points acquired while digitizing the physiology signal. The PC analysis of such data and elimination of those principal components that best correlated with the directly recorded interference (figure 11*c*) resulted in a 'clean' signal (bottom trace of figure 11*b*).
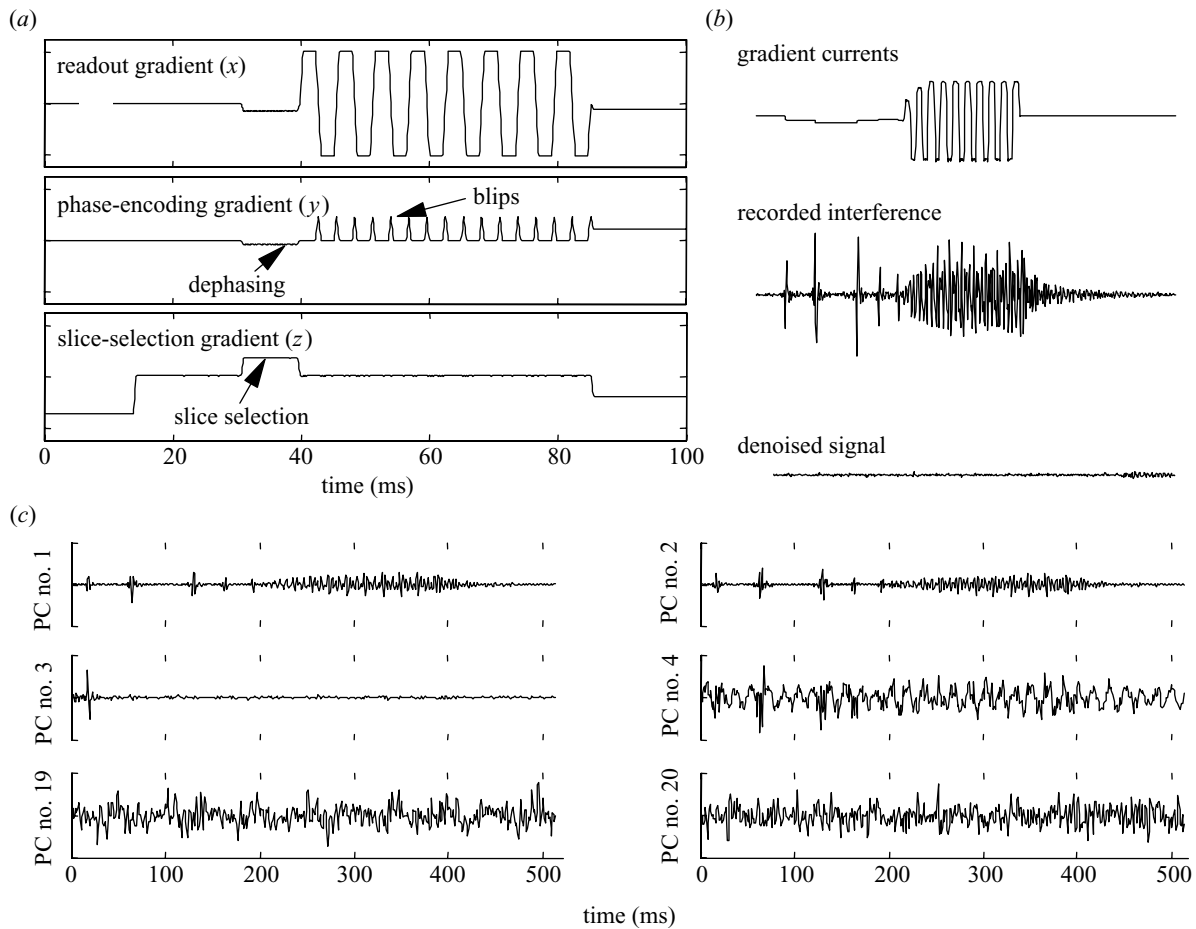
Figure 11. Electromagnetic interference. (*a*) The recorded gradient currents from the slice-selection, phase-encoding and readout gradient for an EP imaging sequence. (*b*) Elimination of residual interference by applying principal component analysis. The top trace is the summation of the three gradient currents, and the middle the induced voltage at the tip of the electrode. PC analysis isolates the residual interference left after online compensation. The denoised signal is depicted by the lower trace. (*c*) Examples of principal components. PCs nos 1 and 2 capture most interference. Setting their eigenvectors to zero and reconstructing the signal with the remaining PCs eliminates any interference.

(**b**) *Microelectrode measurements of the neural signal*

(i) *Imaging the recording site*

Figure 12*a* shows the electrodes used for the combined imaging and physiology experiments, together with the different types of sensors used to compensate the gradient interference. Figure 12*b* is an anatomical scan ($T_E/T_R = 8.9$, $T_R = 2000$ ms, FOV = 96 mm × 96 mm, and a 512 × 384 matrix reconstructed to 512 × 512, slice thickness of 0.5 mm) acquired with the FLASH sequence (Haase *et al.* 1986). Similar scans were typically used for the precise localization of the electrode tip. Here, the electrode tip is located in the middle layers of the primary visual cortex. The image demonstrates the limited susceptibility artefacts caused by the miniature electrode tip. Although of smaller SNR, spin-echo T_2 weighted images are usually even less susceptible to such artefacts. In most scans, a functional signal could be obtained in the immediate vicinity of the microelectrode. Figure 12*c* shows a typical three-dimensional reconstruction of the electrode position (here two electrodes) from a multi-slice anatomical scan (three-dimensional MDEFT; $T_E/T_R = 4/14.9$ ms, four segments).

Figure 13*a* demonstrates the neural activity (black trace) recorded in such a combined experiment superimposed on the BOLD fMRI signal (red). The yellow trace shows the effective (root mean square) value of the neural signal obtained for non-overlapping windows of 250 ms (the T_R of imaging). The neural signal shown was digitized, denoised as described in § 5*a*, and reduced from 22.3 to 7 kHz. It is a comprehensive signal characterized by time-varying spatial distributions of action potentials (spikes) superimposed on relatively slow varying field potentials. The action potentials can be isolated from the other signals by using template matching or other statistical pattern recognition techniques (figure 13*b*).

The instantaneous or mean rate of such spikes is the neuronal variable most frequently examined with respect to a sensory stimulus or behavioural state, and the one recently used to examine quantitatively the relationship of the BOLD signal to neural activity by comparing human fMRI data with electrophysiological data in monkeys performing the same task (Heeger *et al.* 2000; Rees *et al.* 2000; for a review see Heeger & Ress 2002). At this point it is therefore worth taking a moment to consider what aspects of cortical processing the commonly reported spikes represent. Or, more generally, what kind of cortical activity is actually measured by the microelectrodes?
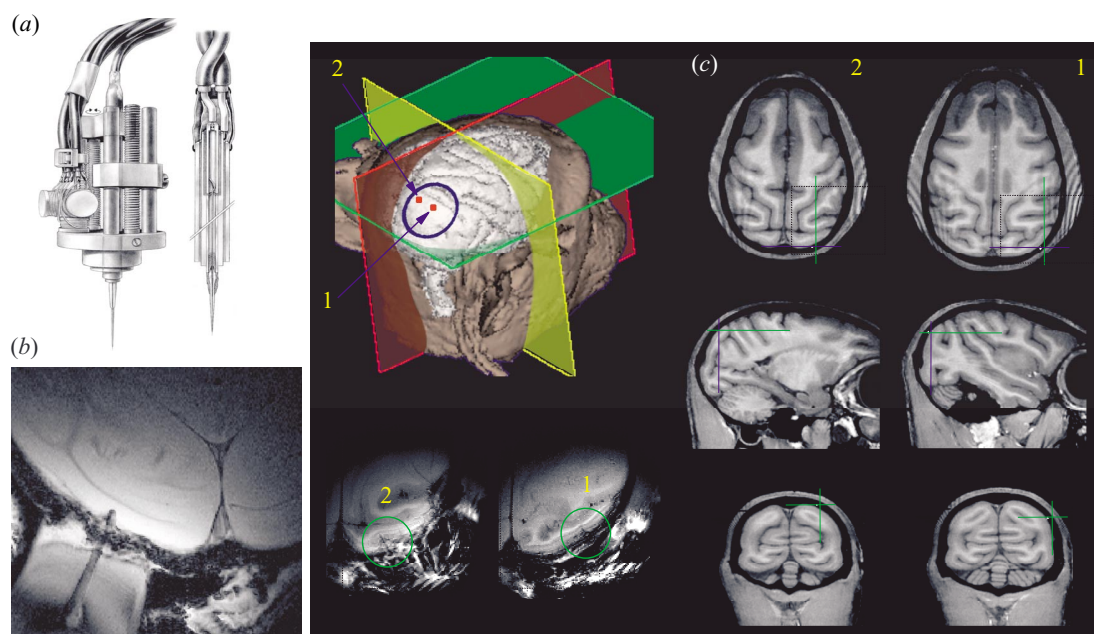
Figure 12. (*a*) The microelectrodes and their holder consisting of three concentric, metallic cylinders, the innermost serving as the contact point for the electrode, the middle as the far-interference sensor and the outermost as the ground. The three-coil magnetic-field sensor used to compensate for near interference is also shown. (*b*) FLASH scan (see § 5b(i)) showing the location of the electrode-tip in the primary visual cortex. (*c*) A reconstruction of the position of the two electrodes from the three-dimensional MDEFT scans (top left) with orthogonal views (right). At the bottom left the inversion-recovery images show the actual electrodes (double electrode recording).
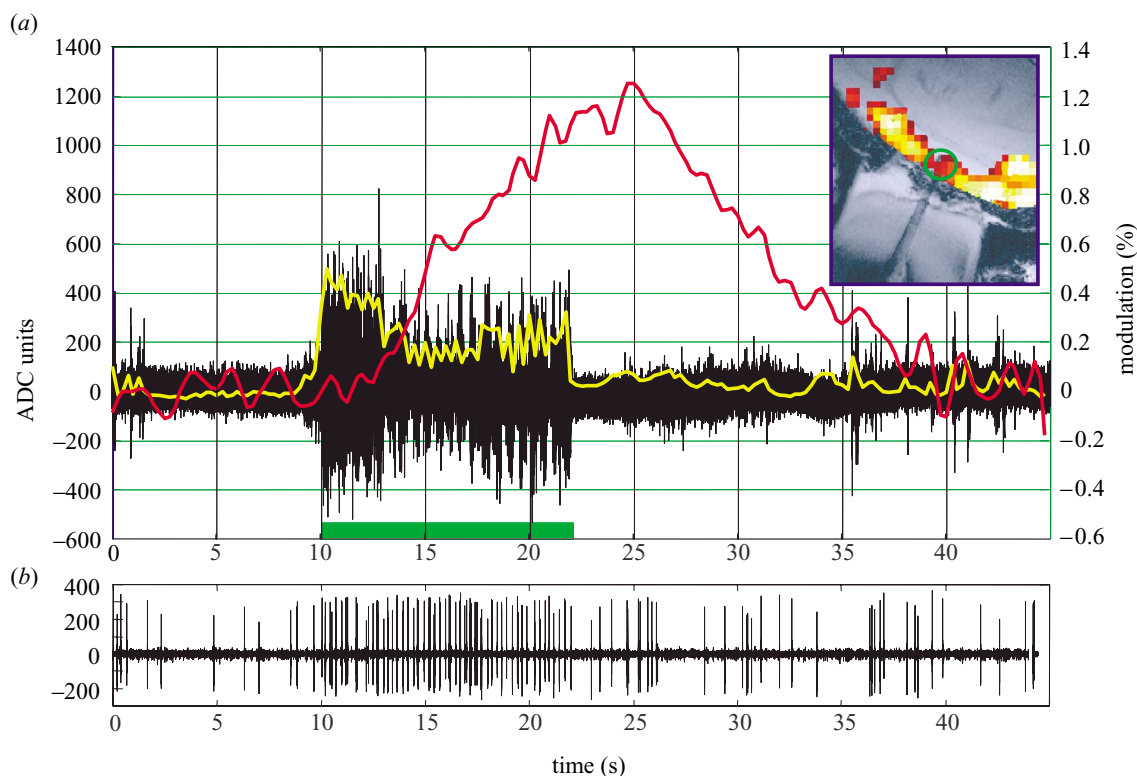

Figure 13. The neural signal. (*a*) The comprehensive signal, with its effective values in yellow and the BOLD activation in red. The BOLD response is the average time-series of the voxels within the green circle of the T_2^*-weighted image in the inset. The green horizontal bar shows the stimulus presentation period. Black trace, raw; yellow trace, root mean square. (*b*) A sequence of single action potentials included in the comprehensive signal. The spikes were isolated using statistical methods. Their rate is one of the parameters often compared with the haemodynamic response. In most extracellular recordings, in particular in those conducted with behaving animals, such isolated action potentials commonly reflect the 'output' activity of a studied area (see § 5b(v)).
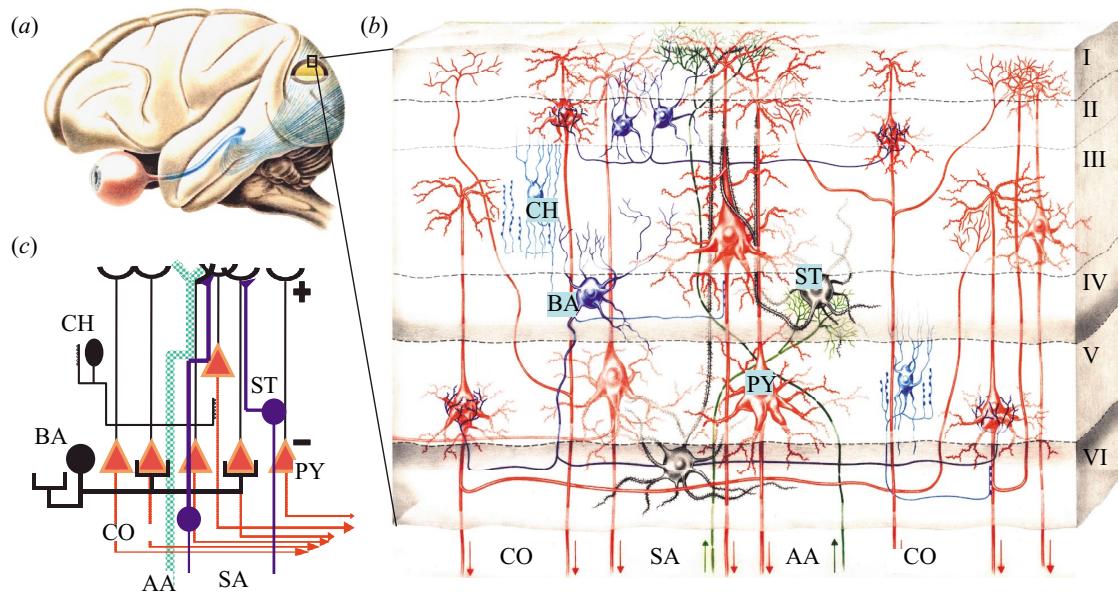
Figure 14. Cortical circuitry. (*a*) Lateral view of a monkey brain. The section is in the striate cortex. (*b*) Neuronal types and connections. (*c*) Model of basic cortical circuitry showing the 'open field' arrangement of pyramidal cells. The parallel unidirectional arrangement of apical dendrites facilitates the summation of field potentials by generating strong dipoles (see § 5*b*(ii)). Abbreviations: CH, chandelier; BA, basket; PY, pyramidal; ST, stellate cells; SA, specific afferents; AA, association afferents; CO, pyramidal cell axons representing cortical output.
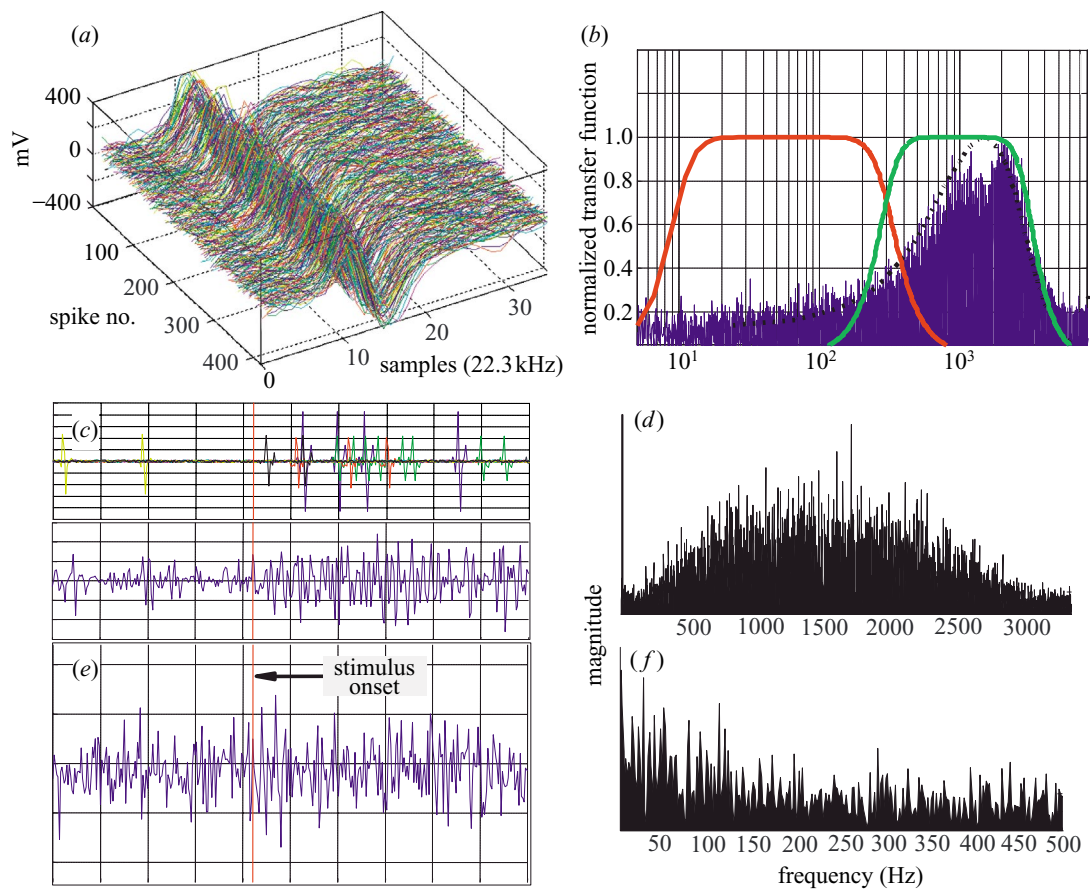

Figure 15. The rationale of band separation in extracellular recordings. (*a*) Isolated action potentials. (*b*) The average spectrum of these potentials is shown with the blue surface plot. The red and green traces represent the transfer functions of the chosen filters. They correspond to the LFPs and MUA, respectively. Red trace, LFP transfer function; green trace, MUA transfer function; dotted black trace, average spike-spectrum. (*c*) Top, using the isolated spikes, spike trains were simulated by using the interspike probability distributions measured in the actual experiment. Bottom, the simulated spikes are summed up to obtain artificial MUA. (*d*) The spectrum of such activity. (*e*,*f*) Simulations for pEPSPs.

(ii) *What is measured by the electrodes?*

Almost all physiology studies in conscious animals report extracellular recordings. While the principles at work during the recording of transmembrane electrical events with intracellular electrodes are reasonably well understood, the interpretation of such extracellular recordings often proves very difficult. Most variations in such signals are closely related to the architecture of neuronal sites, making a comprehensive quantitative treatment of this subject enormously complicated.

In the classical treatment of the topic, a neuron is considered to be embedded in an extracellular medium that acts as a volume conductor (Lorente de Nó 1947) (for a detailed review on field potentials see Freeman (1975); for background in biophysics see Aidley 1989; Johnston & Wu 1995; Koch 1999). When the membrane potential between two separate regions of such a neuron is different, there is a flow of current in the neuron matched by a return current through the extracellular path. Active regions of the membrane are considered to act as a current *sink* and inactive ones as a *source* for the active regions. Such extracellular field potentials add up linearly and algebraically throughout the volume conductor. Thus, with respect to a remote or indifferent electrode potential, fields generated by, say, two neurons may add to or cancel each other depending upon the relative timing of their action potentials. Synchronous activation of many neurons lying in an array within the brain will result in a large field potential that is very similar to the action potential of a single neuron within that array. At least, that is what would happen if the volume conductor behaved like an ohmic resistor and was isotropic; but in actuality this is not the case. It is actually made up largely of neuronal elements with a comparatively small portion of the total volume occupied by extracellular fluid. The membrane of the neurons 'adds' a great deal of capacitance and makes it unlikely that current will flow uniformly in all directions around the neuron. In fact, the orientation of dendrites and axons dramatically influences the summation of the potentials. In other words, although theoretical calculations are useful, understanding the content of the comprehensive signal acquired by the electrode requires systematic experimentation and good knowledge of the microanatomical cortical architecture.

Figure 14b is a schematic drawing of neo-cortex (a section of the primary visual cortex of monkeys illustrated in figure 14a) with some basic neuron types and their interconnections (for comprehensive reviews see Szentagothai 1978; Martin 1988; Lund *et al.* 1994). The pyramidal cells with their prominent apical dendrites are the principal (projection) neurons, representing the sole cortical output. They project to other brain areas and to the spinal cord, but also have recurrent collaterals projecting locally. They receive input from other pyramidal cells (recurrent input) and from a number of interneurons, including the spiny stellate cells, chandelier cells and the small and large basket cells. Input to the pyramidal cells may also be of thalamic (specific) and cortical (association) origin. The pyramidal cells are highly polarized, and their apical dendrites are always perpendicular to the pial surface of the brain. They are thus an exquisite example of a so-called *open field* geometrical arrangement (figure 14c), because the dendrites face in one direction and the soma in

another. This produces strong dendrite-to-soma dipoles when they are activated by synchronous synaptic input. Other neurons are oriented horizontally, and may contribute less efficiently or not at all to the sum of potentials.

If a microelectrode is inserted into a brain site, say at a point in cerebral cortex, the measured potential with respect to a distant site actually reflects many different action potentials of various sizes, some at high amplitudes and others at amplitudes that are barely discriminable from the thermal noise at the electrode tip. The spikes are superimposed on many other waves of lower frequency. Traditionally, the spikes and the slower voltage variations are separated from one another by high- and low-pass filtering, respectively, and this band separation is thought to reflect different types of activity. A filter cut-off of *ca.* 300–400 Hz is used in most recordings to obtain MUA (above 400 Hz) and (LFPs (below 300 Hz).

(iii) *Origin of LFPs and MUA: the logic of frequency-band separation*

The rationale behind this frequency-band separation can be understood on the basis of some simple theoretical considerations (unpublished simulations). Spikes are fast events lasting only 0.4–0.5 ms and 0.7–1.0 ms for axons and soma, respectively. EPSPs or IPSPs, on the other hand, may last several milliseconds and range from a couple to 100 ms. In other words, they are slow waves. A spectral analysis of these two types of waveforms shows quantitatively that they fall into two different frequency bands. More specifically, individual action potentials in the comprehensive signal can be detected and isolated using a variety of statistical pattern recognition techniques. Figure 15a shows 392 isolated action potentials. The power spectrum of each spike is computed and the average of these spectra is plotted in figure 15b (dotted black trace). The blue line shows the actual spectrum of the MUA from the same session. Note the similarity between the spectral power distribution of the MUA with that of a single spike waveform. Superimposed on this plot are the frequency responses of the filters used to split the original signal into bands. For our measurements the LFPs (red trace) were extracted by bandpass filtering between 10 and 300 Hz, and the MUA (green trace) by bandpass filtering between 300 and 3000 Hz. It can be seen that the average spectrum of a spike is well within the region thought to represent MUA. The latter is, after all, the result of a summation of many such waveforms (spikes) shifted randomly in time, and it does not substantially change the spectral power distribution, a fact shown by the simulations in figure 15c,d.

In the same vein, the average spectrum of simulated population pEPSPs shows substantially higher energy in the low-frequency range (below 150 Hz) than in the MUA range. The summation of such potentials (figure 15e), even without any synchronicity constraints, yields the spectrum shown in figure 15f. To a large extent, therefore, population EPSPs and MUA are separated in the frequency domain. But the inverse may not be always true, in the sense that a considerable synchronization of spikes exhibiting significant periodicity at different frequencies may yield power in the low-frequency range. However, such intrusion will take the form of single spectral peaks rather than a broad enhancement over the

entire LFP range. All in all, MUA most probably represents the average spiking of small neural populations around the electrode, and LFPs represent the weighted averages of dendrosomatic postsynaptic signals reflecting input activity (afferent or local). The synchronization of input activity facilitates the summation of LFPs, although their slow nature, which itself facilitates summation as well, does not impose strict synchronization constraints.

(iv) *Origin of LFP and MUA: experimental evidence*

The aforementioned simple theoretical considerations are consistent with experimental work. The extracellular current flow does indeed vary from one recording site to another as a direct function of neuronal size (Nelson 1966), and the magnitude of axonal spikes directly correlates with the size of the transmitting axon (Gasser & Grundfest 1939; Hunt 1951). Furthermore, it has been shown that fast activity (i.e. activity in the 'MUA range' mentioned in § 5b(iii)) is a characteristic property of a given brain site (Buchwald & Grover 1970), varying considerably in amplitude from one brain region to another but remaining relatively constant for any particular site (e.g. neocortex versus hippocampus). In combined physiology–histology experiments. Moreover, it was found that homogeneous populations of large cells occur at sites of large amplitude fast activity and vice versa (Grover & Buchwald 1970). Thus, the specificity of the fast activity reflects the magnitude of variation of extracellular spike potentials rather than artefacts such as variations in the recording system, fibre discharge contamination or differences in local tissue impedances. Thus, the large amplitude of fast activity reflects large-amplitude extracellular potentials and small-amplitude fast activity is correlated with small potentials.

Fast MUA can be measured whenever the impedance of the electrode is sufficiently low, so that spikes from single units do not predominate in the signal. Electrodes with exposed tips of *ca.* 100 μm (impedance from 40 to 120 kΩ), for example, were estimated to record from a sphere of radius equal to 50–350 μm (Grover & Buchwald 1970; Legatt *et al.* 1980; Gray *et al.* 1995), whereby the activity from each point within the sphere is weighted by a factor depending on the distance of the point from the tip of the electrode (Nicholson & Llinas 1971). Recent simultaneous intracellular and extracellular tetrode recordings from single neurons showed that the amplitude of the average extracellular spike decreases rapidly as a function of the distance of the tip from the soma, with the largest amplitudes recorded at distances smaller than 50 μm; at distances greater than 140 mm, no extracellular spike activity could be discerned from the background noise (Henze *et al.* 2000). In conclusion, depending on the recording site and the electrode properties, the MUA most probably represents a weighted sum of the extracellular action potentials of neurons within a sphere of *ca.* 200–300 μm radius, with the electrode at its centre. Spikes produced by the synchronous firings of many cells can, in principle, be enhanced by summation and thus detected at a larger distance (Huang & Buchwald 1977; Arezzo *et al.* 1979).

LFPs, on the other hand, were shown to correlate with synaptic interactions and less often with MUA. Initial evidence for this came from combined EEG and intracortical recordings showing that the slow wave activity in the EEG is largely independent of the neuronal spiking (Fromm & Bond 1964, 1967; Ajmone-Marsan 1965; Buchwald *et al.* 1965). These studies indicated that slow field fluctuations reflect the extent and geometry of dendrites in each recording site and are not correlated with cell size. More recent evidence comes from current-source density analysis and combined field potential and intracellular recordings. The former has indicated that LFPs actually reflect a weighted average of synchronized dendrosomatic components of synaptic signals of a neural population within 0.5–3 mm of the electrode tip (Mitzdorf 1987; Juergens *et al.* 1999). The upper limits of the spatial extent of LFP summation were indirectly calculated by computing the phase coherence of LFPs as a function of interelectrode distance in experiments with simultaneous multiple-electrode recordings (Juergens *et al.* 1996).

Combined intracellular and field potential recordings also indicate a synaptic–dendritic origin for the LFPs. Experiments comparing membrane and network properties typically investigate the phase locking of membrane potential oscillations (rhythmic discharges) to certain frequency bands. Traditionally, low-frequency signal modulations are classified in a number of specific frequency bands initially introduced in the EEG literature (see Elul 1969, 1971; Pedley & Traub 1990). For one, EEG is classified in three distinct groups: rhythmic, arrhythmic and dysrhythmic. The first two appear in normal subjects and refer to waves of approximately constant frequency and no stable rhythms, respectively. The latter refers to rhythms or patterns of EEG activity that characteristically appear in patient groups and rarely or never in healthy subjects. Rhythmic EEG is further subdivided into frequency bands known as delta (δ, 0–4 Hz), theta (θ, 4–8 Hz), alpha (α, 8–12 Hz), beta (β, 12–24 Hz), and gamma (γ, 24–40/80 Hz) that are typically characterized by different amplitudes (Lindsley & Wicke 1974; Steriade & Hobson 1976; Basar 1980; Steriade 1991). The classification is based on the strong correlation of each band with a distinct behavioural state. In humans, delta and theta, for instance, are generally associated with sleep and have the largest amplitudes in EEG activity; alpha waves are associated with a state of relaxed wakefulness and beta and gamma with intense mental activity. These last two are characterized by very small amplitudes. Such rhythmic patterns are associated with the thalamocortical loops and are modulated by the ascending network system and basal forebrain (Steriade 1991; Steriade *et al.* 1993).

Important insights into the origin of LFPs come from studies examining the relationship of activity in any of the frequency bands described in the previous paragraph to changes in the membrane potential of individual neurons. Recently, for instance, the relationship between membrane and network properties of lateral septum neurons to the theta band was studied in the rat hippocampus (Pedemonte *et al.* 1998). The DB and the MSN are thought to act as θ-rhythm pacemakers, because cells in these nuclei display rhythmic membrane oscillations and bursting discharge patterns (Barrenechea *et al.* 1995), while lesions of these nuclei abolish this rhythm (Gray & Ball 1970; Apostol & Creutzfeldt 1974). Furthermore, the lateral septum is thought to provide feedback input from
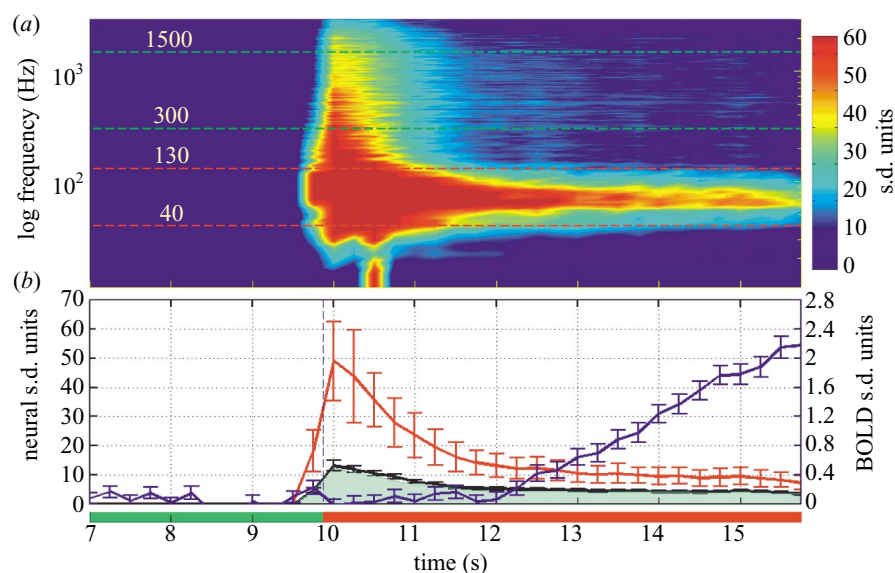
Figure 16. Time-dependent frequency analysis for the population data. (*a*) Spectrogram of the first 6 s of the neural response averaged over all data. Each time-course is expressed in units of the standard deviation of the prestimulus period. Colour coding indicates the reliability of the signal change for each frequency (SNR). Red and green dashed lines show the LFP and MUA frequency bands, respectively. Mean = 72.96; s.d. = 21.04. (*b*) Mean LFP (red), MUA (black) and total (light green surface) neural response averaged across all frequencies, together with the BOLD signal (blue). Note that the 'activity increase' seemingly occurring before the stimulus presentation is due solely to the windows used to create the spectrograms. The two vertical axes show the difference in the SNR of the neural and BOLD signals. Across all the data a difference of approximately one order of magnitude was found in the reliability of the two signals. From Logothetis *et al.* (2001), with permission.
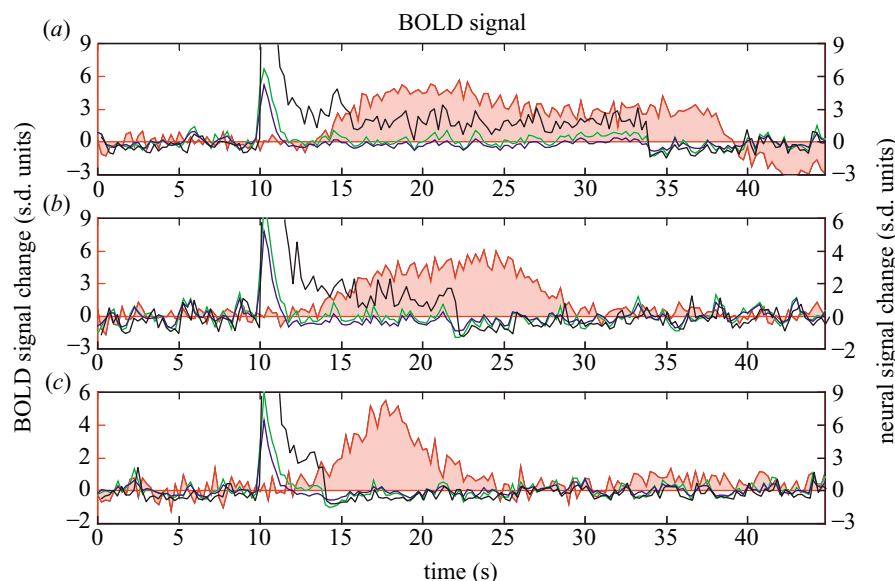

Figure 17. Simultaneous neural and haemodynamic recordings from a cortical site showing a transient neural response. (*a–c*) Responses to pulse stimuli of 24, 12 and 4 s. Pink tint, BOLD; black trace, LFP; green trace, MUA; blue trace, SDF. Note that both single- and multiple-unit responses adapt a couple of seconds after stimulus onset, with LFP remaining the only signal correlated with the BOLD response. The SDF (see § 6b) reflects the instantaneous firing rate of a small population of neurons whose action potential could be identified and isolated during the analysis using standard mathematical methods. Note the covariation of the rate of such isolated spikes with the filtered MUA. From Logothetis *et al.* (2001), with permission.

hippocampus to DB and MSN (see Raisman 1966). Inter-actions within this pathway were investigated by making simultaneous extracellular recordings of LFPs and intra-cellular recordings of transmembrane potentials from neurons exhibiting rhythmic discharges or phase locking to theta oscillations. The results indicated that the rhythmic discharge patterns of septal neurons are due to synaptic

interactions (Pedemonte *et al.* 1998). Membrane oscillations in lateral septal neurons, for instance, are phase locked to hippocampal theta activity, the amplitude of the former being dependent on the amplitude of the field changes. Furthermore, current injections showed that hyperpolarization increases and depolarization decreases the amplitude of oscillations, indicating that EPSPs may
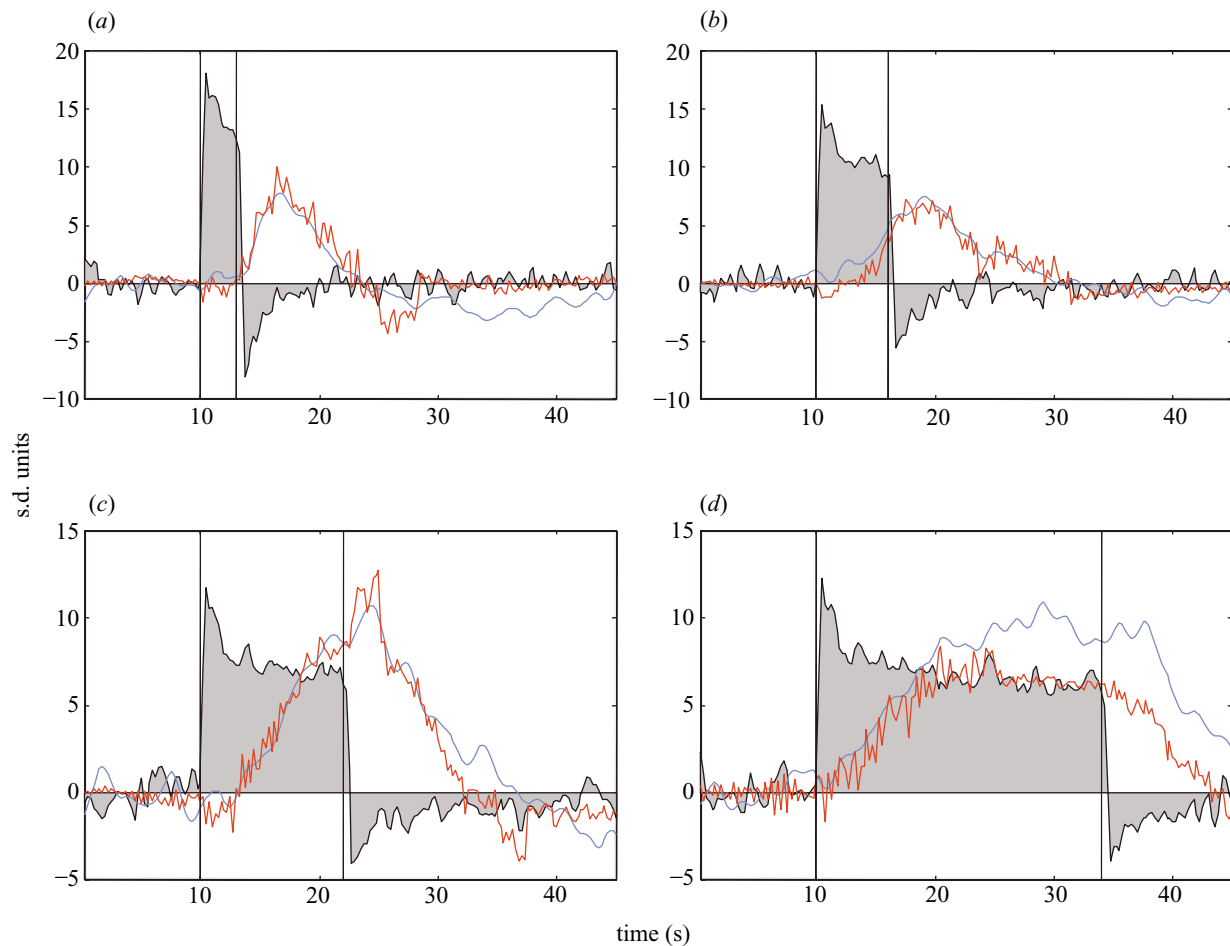
Figure 18. The measured LFP response as well as the measured and estimated BOLD response. (*a*) Pulse = 3 s; contrast = 100%; (*b*) pulse = 6 s; contrast = 100%; (*c*) pulse = 12 s; contrast = 100%; (*d*) pulse = 24 s; contrast = 100%. The grey trace is the measured LFP signal; the blue trace is the measured BOLD and the red trace is the estimated BOLD. Residual analysis showed an increased error for a longer pulse duration. Visual inspection of the data from a 24 s long stimulus presentation revealed greatly increased residuals after the initial ramp of the BOLD response, suggesting the existence of nonlinearities not captured by the Wiener–Kernel analysis applied here to the data.

make a greater contribution to the generation of periodicity than IPSPs (Pedemonte *et al.* 1998).

Similar conclusions were drawn in combined intra- and extracellular recordings in invertebrates. The antennal lobe of locust has a mixed population of projection and local (inter-) neurons (for a review see Laurent *et al.* 2001). The former are excitatory and project to the MB and lateral protocerebral lobe; the latter are inhibitory. Neither class has intrinsic oscillatory properties, and both show rhythmic activity patterns only during natural (odour) or electrical stimulation. Simultaneous recordings from the antennal lobe and the MB showed that stimulation evokes reproducible, phase locked 20–30 Hz oscillations in the membrane of PNs and the LFPs of MB neurons (Wehr & Laurent 1999). Here, too, paired intracellular recordings and pharmacological manipulations indicate that to a large extent LFP changes originate in the synaptic interactions within the antennal lobe.

But rhythmic activity related to some of the EEG frequency bands has also been reported for the spiking principal neurons. Many pyramidal neurons in layer 5 of the neocortex show prolonged, 5–12 Hz rhythmic firing patterns due to intrinsic membrane properties such as sodium conductance, which is essential for rhythmicity, and cal-

cium-dependent conductance, which strongly modifies it (Silva *et al.* 1991). Although synaptic networks of intrinsically rhythmic neurons may still be the origin of the synchronized cortical oscillations, spiking activity—in this case—will be tightly correlated with the LFPs and will contribute to the modulation of their amplitude. Similar behaviour has been reported for a biophysically distinct class of pyramidal cells (chattering cells) in the superficial cortex layers of cats (Gray & McCormick 1996). Their oscillatory behaviour (20–60 Hz), accompanied by periodic changes in the membrane potential, is induced in response to suprathreshold depolarizing current injection or visual stimulation, and is absent during periods of spontaneous activity. Oscillations were also observed in the peripheral olfactory system of insects (locust, *Schistocerca americana*) (Laurent & Davidowitz 1994), the olfactory cortex of rats and rabbits (Granger & Lynch 1991), and the somatosensory cortex of monkeys (Mountcastle *et al.* 1990; Ahissar & Vaadia 1990; Recanzone *et al.* 1992; Romo & Salinas 1999). New insights into their generation, as well as into intracortical processing in general, came from the study of inhibitory networks in hippocampus (Buzsaki & Chrobak 1995; Kandel & Buzsaki 1997; Kocsis *et al.* 1999).

In conclusion, MUA is obtained by bandpass filtering of the comprehensive neural signal in a frequency range of 400 to a few thousand Hz, and it represents the weighted average of the spiking activity within a sphere of approximately one-third of a millimetre radius with the microelectrode at its centre. It most probably includes dendritic spikes and activity from interneurons. LFPs, on the other hand, predominantly reflect synaptic events, including synchronized afferent or local spiking activity. They are obtained by low-pass filtering the signal to permit frequencies below 300 Hz, or by bandpass filtering it between 10 and 300 Hz, to exclude the sleep-related slow oscillations or changes due to anaesthesia. Spatial summation of LFPs occurs within a couple of millimetres from the electrode tip.

(v) *Spike rates of single units in extracellular recordings reflect cortical output activity*

Although LFP and MUA activity conveys important information regarding the role of small neuronal populations in sensory processing or behaviour, most neurophysiological studies, in particular those in behaving animals, concentrate on the activity of isolated single units. It is therefore worth considering the question of which neuronal types are usually reported in such experiments. The frequency with which certain neuronal types appear in extracellular recordings depends on their relative density, the size of their spikes, electrode properties and the stability of the recordings. For equivalent transmembrane action potentials, the discharge of a large neuron generates a substantially greater flow of membrane current and a larger extracellular spike than a small cell, and the resulting extracellular field remains above recording noise levels over a greater distance. Theoretically, one would expect larger neurons (cells with 20–30 μm diameter or greater) to generate a potential of 100 μV or more within a 100 μm diameter sphere with the electrode tip at its centre (Rall 1962). It follows that spikes generated by such large neurons may remain above the noise level over a greater distance from the cell than do spikes from small neurons, and thus microelectrodes are likely to sample their somas or axons preferentially. In addition, recordings from such neurons tend to be less sensitive to small motions, a quality which is critical for the stability of recordings in the alert behaving animal. Smaller neurons require the electrode tip to lie considerably closer to that neuron than to any other active ones of comparable size. If the tip is too close, it will usually injure a small cell, and if it is too far away, it becomes difficult to isolate the cell. Thus, the measured spikes represent very small neural populations of one or just a few isolated large cells, that in the cortex are by and large the principal cells (e.g. pyramidal cells in the cerebral cortex and Purkinje neurons in the cerebellar cortex).

Various investigators have also demonstrated such a microelectrode sampling bias experimentally. In a systematic study, Towe & Harding (1970) stimulated the PTNs of cats at the medullary level with stimulus intensities that would activate all the axons in the pyramidal tract, and computed the distribution of conduction speeds and the expected latencies by simultaneously recording in the pericruciate cortex. They then compared these distributions with those expected on the basis of the histological fibre

spectrum, namely from the distribution of 'axon sizes'. They found that although the pyramidal tract of cats consists mainly of small axons (low-conduction speed and thus long latencies), the latencies obtained during the experiment (antidromic response latencies) were mostly short (around 1 ms). Due to the fact that all the axons were stimulated, they indicated that a bias towards neurons with large bodies is evident in extracellular recordings. A similar electrode bias was reported in the monkey PTN system (Humphrey & Corrie 1978).

It follows that the vast majority of experiments employing extracellular recordings report on the activity of principal cells, namely on the output of a cortical area related to a given stimulus or task. This is particularly true for experiments in the alert, behaving animal or human (Fried *et al.* 1997; Kreiman *et al.* 2000*a*,*b*), during which even slight movements make holding smaller neurons for a sufficiently long time an extremely difficult task. Furthermore, recording from interneurons (e.g. inhibitory cells) is often very difficult as well, for their response is often uncorrelated to the stimulus or behaviour state of the animal.

6. THE NEURAL ORIGIN OF BOLD RESPONSE

(a) *Magnitude changes in LFPs and MUA during visual stimulation*

The contribution of MUA and LFP signals to the haemodynamic response was examined by applying time-dependent frequency analysis to the raw data. Typically, after stimulus presentation a transient increase in power was observed across all frequencies, followed by a lower level of activation that was maintained for the entire duration of the stimulus presentation. A prominent characteristic in all spectrograms was a marked stimulus-induced increase in the magnitude of the LFP, which was always larger than that observed for MUA. A decrease in neural activity was also observed immediately after the termination of the stimulus.

To confirm these results a spectrogram was computed across all the scans for the first 6 s of the neural response averaged over all the data collected during 6, 12, 12.5 and 24 s-long stimulus presentation (figure 16). The time series at each frequency is expressed in units of standard deviation (s.d.) of the activity in the prestimulus period and therefore represents the SNR of the response at that frequency. The average LFP and MUA responses were computed as the mean vector of the time-series in the frequency regions 40–130 Hz (red dashed lines) and 300–1500 Hz (green dashed lines). Figure 16*b* shows these mean curves together with the total average over all frequencies and the BOLD responses for all data in s.d. units. Note the marked difference in SNR (scale of the vertical axes) between the neural and the BOLD signals. Such a difference can, in principle, result in statistical rejection of the activation of various regions during mapping experiments, despite the fact that the underlying neural activity is highly robust and significant.

(b) *Adaptation reveals BOLD response without MUA*

A fraction of all multi-unit responses were found to be transient; they showed an initial increase in amplitude and

then returned to the baseline within 2–4 s. Figure 17 illustrates simultaneous recordings of haemodynamic responses, LFPs and transient single-unit activity and MUA in the striate cortex. As can be seen, both the SDF, representing the instantaneous firing rate of one or a few neurons whose spike waveform could be identified, and the MUA show strong adaptation, returning to the baseline *ca.* 2.5 s after stimulus onset. By contrast, the activity underlying the LFPs remains elevated for the entire duration of the visual stimulus. There was no single observation period or recording site for which the opposite result was observed, namely a highly correlated MUA signal and an uncorrelated or missing LFP signal. Similarly, we never observed MUA that was larger in magnitude than the measured LFP activity magnitude, or that the MUA–SNR ratio was higher than the LFP–SNR ratio. These findings indicate that BOLD activation may reflect the neural activity related to the input and the local processing in any given area rather than the output spiking activity.

(c) *LFP activity predicts the BOLD response better than MUA*

In a linear system, the relationship between input and output can be characterized completely by the haemodynamic impulse response function. Although the constraint of linearity may not apply to the haemodynamic system under all stimulation conditions, we initially applied linear systems analysis to examine the relationship of the BOLD fMRI signal to the different types of neural activities. Correlation analysis was applied to both the measurements obtained during visual stimulation and the measurements of spontaneous activity. The impulse response of the system is the cross covariance function of the neural and BOLD responses. The estimated impulse response functions were used to convolve the LFP and MUA responses to various stimuli. Figure 18 shows the neural responses as well as the measured and estimated BOLD responses for four different stimulus durations. Residual analysis showed increased errors (in the least-square sense) for longer pulse durations. Simple visual inspection of the data from the 24 s long stimulus presentation (figure 18*d*) shows greatly increased residuals after the initial ramp of the BOLD response, indicating the existence of nonlinearities not captured by the Wiener–Kernel analysis applied here to the data. Deconvolution of the BOLD response (figure 19) showed that estimation of the neural response is relatively accurate for low-temporal frequencies (up to 0.16 Hz). Increasing temporal frequency strongly increased the residuals. For stimulation frequencies higher than 0.21 Hz, reconstruction of the neural response was not possible (figure 19*c,d*). Moreover, residual analysis similarly showed lower errors (in the least-square sense) overall in LFP-based estimates than in estimates based on MUA responses. Figure 20*a* plots the distribution of determination coefficients (normalized residuals) for BOLD estimates from LFP and MUA using impulse functions computed from the LFP–BOLD and MUA–BOLD covariance, respectively. The LFP accounted for *ca.* 7.6% more of the variance in the fMRI responses than the MUA. The difference, although small, was statistically significant. Finally, residuals were found

to vary in a similar manner for both LFP and MUA (figure 20*b*).

(d) *BOLD signal and cortical activity: input, local processing and output*

Taken together, these results indicate that changes in the LFPs relate better to the evolution of the BOLD signal than those of the spiking activity of single or multiple neurons. I have already discussed the rationale behind LFP–MUA band separation and the reason the former is thought to represent cortical input and local, intracortical processing and the latter the weighted sum of spiking activity. With these arguments in mind, the results of the combined physiological and fMRI experiments indicate that the BOLD signal mainly reflects the incoming specific or association inputs into an area, and the processing of this input information by the local cortical circuitry (including excitatory and inhibitory interneurons). Naturally, in most cases such activity will be closely related to the output of that area. Incoming signals are processed and usually cause activation of the area's projection neurons. However, in cases in which the incoming signals are modulatory, or the projection neurons are inhibited by local interneurons, spiking activity measured with microelectrodes will be a poor predictor of the BOLD response. A number of experiments demonstrate the plausibility of this argument.

In a recent study, Tolias *et al.* (2001) used an adaptation technique (Grill-Spector *et al.* 1999; Kourtzi & Kanwisher 2001) to study the brain areas processing motion information. They repeatedly imaged a monkey's brain while the animal viewed continuous motion in a single, unchanging direction. Under these conditions, the BOLD response gradually became smaller as the visual neurons adapted to the unchanging stimulation. When the direction of motion was abruptly reversed, the measured brain activity immediately showed a partial recovery or rebound. The extent of this rebound was considered to be an index of the average directional selectivity of neurons in any activated area.

The results confirmed previous electrophysiological studies revealing a distributed network of visual areas in the monkey that process information about the direction of motion of a stimulus. In fact, BOLD signal increases were found in a number of visual areas, including V1, V2, V3 and V5 (MT). The results also confirmed previous fMRI studies providing indirect evidence of interactions between directionally selective neural populations in human area MT by measuring BOLD activity during the motion after-effect (Tootell *et al.* 1995; He *et al.* 1998). What came as a surprise, however, was the strong activation of area V4. Single-unit recordings have repeatedly demonstrated the very weak involvement of this area in motion processing (e.g. Desimone & Schein 1987). BOLD fMRI, alternatively, indicated that the rebound activity, and thus the sensitivity of this area, is as pronounced as that of the area V5 (see figure 21).

An explanation of this result is possible based on the arguments developed earlier. Areas V4 and MT are extensively interconnected (Felleman & Van Essen 1983; Maunsell & Van Essen 1983; Ungerleider & Desimone 1986; Steele *et al.* 1991), yet the properties of MT neurons differ considerably from those of V4. What purpose
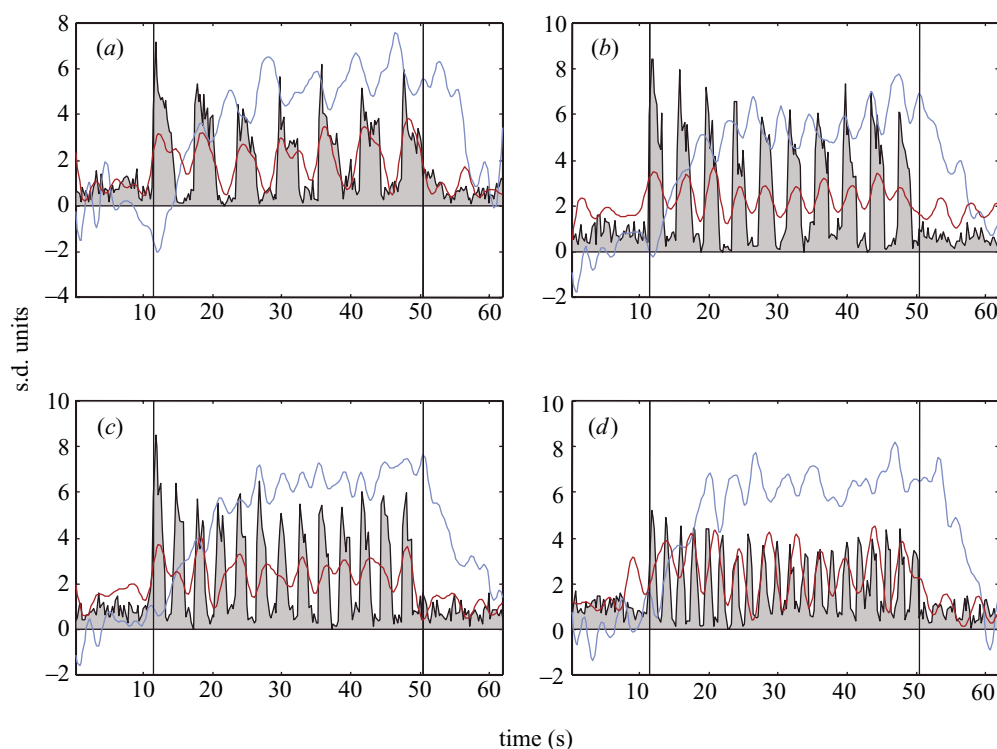
Figure 19. Deconvolution of the BOLD response. Estimation of the neural response was relatively accurate for low-temporal frequencies (0.16 Hz). Increasing the temporal frequency strongly increased the residuals; with frequencies higher than 0.21 Hz reconstruction of the neural response no longer being possible. Area plots show measured neural responses. The grey trace is the measured LFP signal, the blue trace is the measured BOLD and the red trace the estimated neural response. (*a*) Flicker rate = 0.16 Hz, contrast = 100%; (*b*) flicker rate = 0.21 Hz, contrast = 100%; (*c*) flicker rate = 0.25 Hz, contrast = 100%; (*d*) flicker rate = 0.4 Hz, contrast = 100%.

does the extensive interconnectivity serve? The visual system combines a large number of attributes into unified percepts. Areas related to motion, colour or form will certainly be coactivated and signal the presence of a single moving object under normal viewing conditions. Although they process separate stimulus properties, each area may be influencing the sensitivity of the others by providing some kind of 'modulatory' input, which in and of itself is insufficient to drive the pyramidal cells recorded in a typical electrophysiology experiment. BOLD fMRI in such cases will reveal significant activation and will appear to provide results that do not match those of neurophysiology. In this manner a number of experiments in monkeys appear to be inconsistent with fMRI experiments employing the same tasks or stimulation conditions (Tong *et al.* 1998; Gandhi *et al.* 1999; Polonsky *et al.* 2000; Kastner & Ungerleider 2000) (see also review by Blake & Logothetis (2002)), as the synaptic activity produced by lateral or feedback input is visible with imaging but not always with single-unit recordings. A good example is the measurement of the effects of spatial attention on neural activation. Attentional effects on the neurons of striate cortex have indeed been very difficult to measure in monkey electrophysiology experiments (Luck *et al.* 1997; McAdams & Maunsell 1999). However, for similar tasks strong attentional effects have been readily measurable with fMRI in human V1 (Tong *et al.* 1998; Gandhi *et al.* 1999; Kastner & Ungerleider 2000). In addition, attentional effects in area V4 were found to be considerably larger in human fMRI than monkey electrophysiology (Kastner *et al.* 1998; Ress *et al.* 2000).

An exquisite example of dissociation between intracortical processing and output of a brain structure was recently offered by Mathiesen *et al.* (1998, 2000), who demonstrated that both LFPs and CBF can increase at the same time that spiking activity ceases. These investigators stimulated the parallel fibres of cerebellum while recording Purkinje cell activity. Purkinje cells are the projection neurons of cerebellum and represent the only output of the structure. They form the Purkinje cell layer that is sandwiched between the molecular and granular layers. The input to the cerebellar cortex consists of the mossy and climbing fibres. The granule cells are at the 'input' side. Their axons ascend to the molecular layer where they bifurcate in a T-shape to give rise to the parallel fibres, that run strictly parallel to the axis of the folium. These axons can be selectively stimulated with a bipolar electrode using small currents. Their stimulation causes monosynaptic excitation of the Purkinje cells and disynaptic inhibition of the same neurons through the basket cells. The net effect is an inhibition of the Purkinje cells' spike activity, although at the same time synaptic activity may be increased. Mathiesen *et al.* (1998) actually demonstrated exactly this by measuring LFPs, single-unit activity and changes in cerebral flow. Both LFPs and CBF were found to increase when the spiking activity ceased.

Interestingly a very early indication that the top–down modulation of activity in a sensory area resulting from its massive feedback inputs may cause greater changes in cerebral circulation than the activity elicited by a simple sensory stimulus came from the clinical study mentioned in § 2. After many studies, during which the bruit from
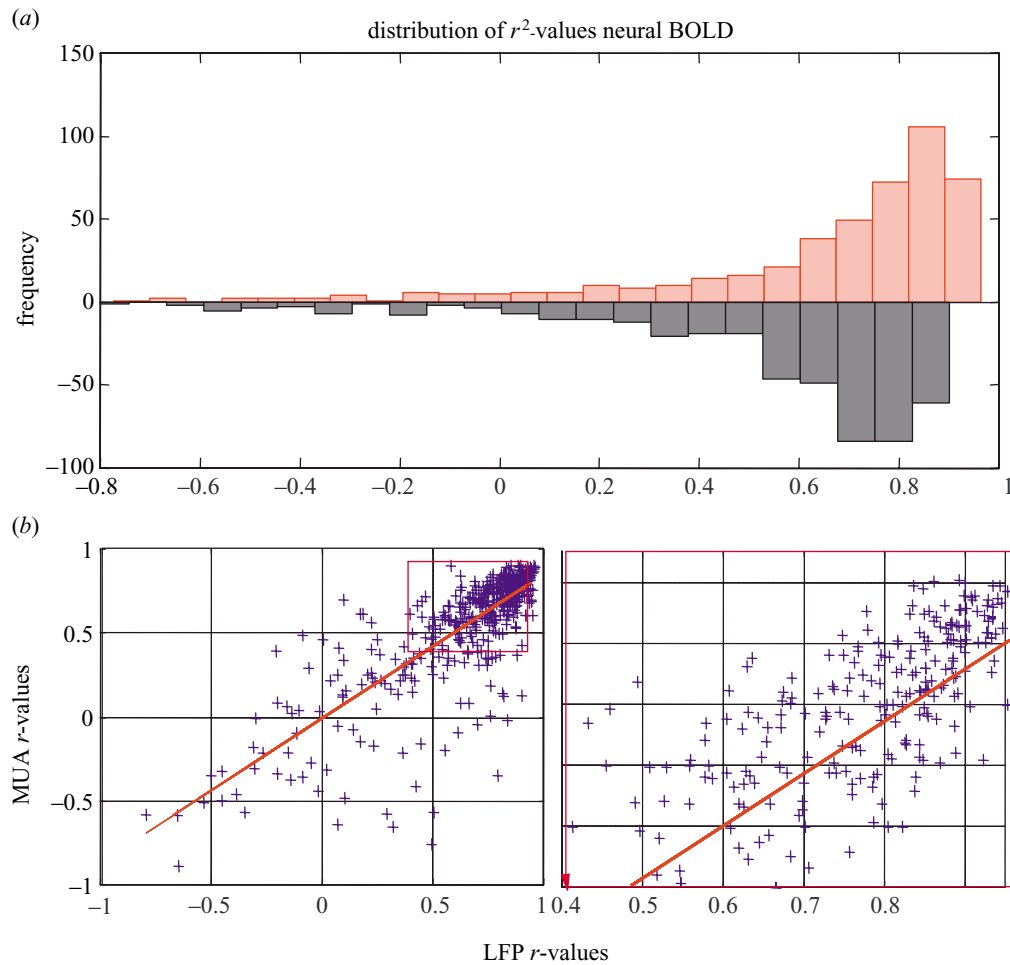
(a)

distribution of r^2-values neural BOLD

(b)

LFP r-values

Figure 20. (a) Distribution of the coefficient of determination (r^2) of LFP (pink) and MUA (grey). The r^2-values for LFP were significantly higher than for MUA. The plot includes data collected with pulse stimuli of 24, 12, 6 and 4 s, with N = 460, LFP mean = 0.521, LFP mode = 0.672, MUA mean = 0.410 and MUA mode = 0.457. (b) Covariation of the estimation error. The right plot is a magnified section of the left scatter plot.
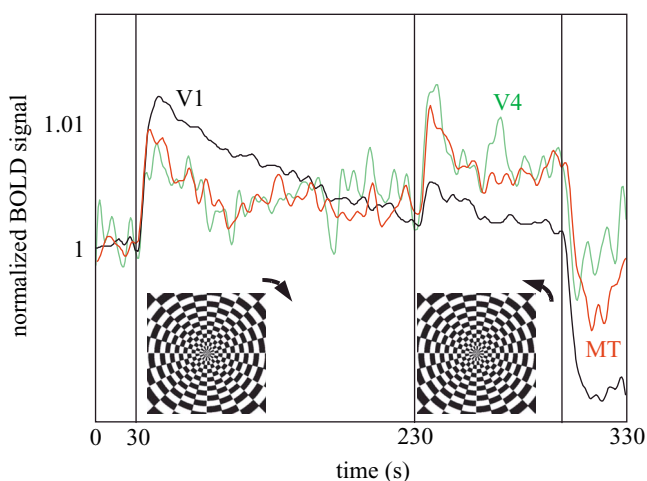

Figure 21. A visual adaptation paradigm was used to localize visual areas that process information about the direction of motion (modified from Tolias *et al.* (2001)). The BOLD signal in area V5 (MT) adapted more quickly than in V1, reflecting the difference in motion processing between these areas. Surprisingly, area V4 showed adaptation as strong and as fast as area V5, which is characterized by a much larger number of directional neurons.

the patient's occipital lobe was systematically recorded, the neurosurgeon Fulton (1928) indicated that 'it was *the effort to discern objects that were just at the limit of Walter K.'s acuity* that brought on the increases of the bruit', rather than merely presenting visual stimuli to his eyes. When no attentive behaviour and mental effort were required no increases in the bruit could be observed. The increase of the bruit during tasks requiring attentional efforts may well have been the result of top–down influences on the human visual system, as has been recently demonstrated in imaging studies (Shulman *et al.* 1997; Tong *et al.* 1998; Gandhi *et al.* 1999; Kastner & Ungerleider 2000).

(e) *LFPs and energy budget*

It should be noted that the greater contribution of LFP activity to the fMRI signal is consistent with recent findings regarding the bioenergetics underlying this signal. It has been shown that neural activity and energy metabolism are closely coupled (see Sokoloff 1989). Recent studies show that a quantitative relationship can actually be established between imaging signals and the cycling of certain cerebral neurotransmitters (Shulman & Rothman 1998; Magistretti *et al.* 1999; Rothman *et al.* 1999), as synaptic activity is tightly coupled to glucose uptake (Pellerin & Magistretti 1994; Takahashi *et al.* 1995). More

specifically, stoichiometric studies using NMR spectroscopy indicate that the utilization of Glu, the dominant excitatory neurotransmitter of the brain (*ca.* 90% of the synapses in GM are excitatory; Braitenberg & Schuez 1998), is equal to the rate at which this molecule is converted to Gln in the brain (Sibson *et al.* 1998). The Glu to Gln conversion occurs in the astrocytes and the required energy is provided by glycolysis. Astrocytes are specialized glia cells which are massively connected with both neurons and the brain's vasculature, and are enriched in glucose transporters. The transporters are driven by the electrochemical gradient of Na^+; for this reason there is a tight coupling between Glu and Na^+ uptake. Both Glu to Gln conversion and Na^+ restoration require ATP. Gln is subsequently released by astrocytes and taken up by the neuronal terminals to be reconverted to Glu (for review see Magistretti & Pellerin 1999). Calculations based on these findings indicate that the energy demands of glutamatergic neurons account for 80–90% of total cortical glucose usage in rats (Sibson *et al.* 1998) and humans (Pan *et al.* 2000).

In addition, electrical microstimulation experiments have indicated that glucose utilization mainly reflects presynaptic activity. In such experiments the increase in glucose utilization is assessed during orthodromic and antidromic stimulation, with the former activating both pre- and postsynaptic terminals and the latter activating only postsynaptic terminals. Increases were only observed during orthodromic stimulation (Kadekaro *et al.* 1985, 1987; Nudo & Masterton 1986) (for review see Jueptner & Weiller 1995). Taken together, these results indicate that the lion's share of brain energy consumption is due to presynaptic activity (restoration of gradients) and neurotransmitter cycling.

Recent calculations have challenged the notion that presynaptic activity is the major energy consumer in the brain (Attwell & Laughlin 2001). These investigators drew up an energy budget by recalculating the contribution of presynaptic activity, but also computing the energy required to restore all gradients changed by postsynaptic activity and action potentials. In their budget, that is based on computations of the number of vesicles released per action potential, the number of postsynaptic receptors activated per vesicle released, the metabolic consequences of activating a single receptor and changing ion fluxes, and neurotransmitter recycling, the largest portion of energy expenditure is attributed to the postsynaptic effects of Glu (*ca.* 34% of the energy in rodents and 74% in humans is attributed to postsynaptic events, mainly excitatory postsynaptic currents). Both pre- and postsynaptic currents are dominant elements of the LFPs, which—as mentioned in the previous paragraph—were indeed found to correlate best with the haemodynamic changes in the cerebral and cerebellar cortex.

7. CONCLUSION

In conclusion, the results of simultaneous fMRI and electrophysiological recordings presented here clearly show that the BOLD contrast mechanism directly reflects the neural responses elicited by a stimulus. Moreover, to a first approximation, BOLD responses and neural responses are shown to have a linear relationship for stimulus presentation of short duration. Neural signals are characterized by considerably higher SNR than the haemodynamic response, indicating that the extent of activation in human fMRI experiments is very often underestimated to a significant extent due to the variation in the vascular response. Finally, the haemodynamic response appears to be better correlated with the LFPs, implying that activation in an area is often likely to reflect the incoming input and the local processing in a given area rather than the spiking activity. While it is reasonable to expect that output activity will usually correlate with neurotransmitter release and pre- and postsynaptic currents, when input into a particular area plays what is primarily a modulatory role, fMRI experiments may reveal activation in areas in which no single-unit activity is found in physiological experiments.

REFERENCES

Abragam, A. 1961 *Principles of nuclear magnetism.* Oxford University Press.

Ackerman, J. J., Grove, T. H., Wong, G. G., Gadian, D. G. & Radda, G. K. 1980 Mapping of metabolites in whole animals by ^{31}P NMR using surface coils. *Nature* **283**, 167–170.

Ahissar, E. & Vaadia, E. 1990 Oscillatory activity of single units in a somatosensory cortex of an awake monkey and their possible role in texture analysis. *Proc. Natl Acad. Sci. USA* **87**, 8935–8939.

Aidley, D. J. 1989 *The physiology of excitable cells.* Cambridge University Press.

Ajmone-Marsan, C. 1965 Electrical activity of the brain: slow waves and neuronal activity. *Israel J. Med. Sci.* **1**, 104–117.

Albright, T. D. 1984 Direction and orientation selectivity of neurons in visual area MT of the macaque. *J. Neurophysiol.* **52**, 1106–1130.

Ames, A. 2000 CNS energy metabolism as related to function. *Brain Res.—Brain Res. Rev.* **34**, 42–68.

Ances, B. M., Zarahn, E., Greenberg, J. H. & Detre, J. A. 2000 Coupling of neural activation to blood flow in the somatosensory cortex of rats is time-intensity separable, but not linear. *J. Cerebral Blood Flow Metabolism* **20**, 921–930.

Apostol, G. & Creutzfeldt, O. D. 1974 Crosscorrelation between the activity of septal units and hippocampal EEG during arousal. *Brain Res.* **67**, 65–75.

Arezzo, J., Legatt, A. D. & Vaughan, H. G. J. 1979 Topography and intracranial sources of somatosensory evoked potentials in the monkey. I. Early components. *Electroencephalography Clin. Neurophysiol.* **46**, 155–172.

Attwell, D. & Laughlin, S. B. 2001 An energy budget for signaling in the grey matter of the brain. *J. Cerebral Blood Flow Metabolism* **21**, 1133–1145.

Axel, L. 1984 Blood flow effects in magnetic resonance imaging. *Am. J. Roentgenology* **143**, 1157–1166.

Axel, L. 1986 Blood flow effects in magnetic resonance imaging. *Magn. Resonance A.*, 237–244.

Bandettini, P. A., Wong, E. C., Hinks, R. S., Tikofsky, R. S. &

Hyde, J. S. 1992 Time course E.P.I. of human brain function during task activation. *Magn. Resonance Med.* **25**, 390–397.

Bandettini, P. A., Kwong, K. K., Davis, T. L., Tootell, R. B., Wong, E. C., Fox, P. T., Belliveau, J. W., Weisskoff, R. M. & Rosen, B. R. 1997 Characterization of cerebral blood oxygenation and flow changes during prolonged brain activation. *Hum. Brain Mapping* **5**, 93–109.

Barrenechea, C., Pedemonte, M., Nunez, A. & Garcia-Austt, E. 1995 *In vivo* intracellular recordings of medial septal and diagonal band of Broca neurons: relationships with theta rhythm. *Exp. Brain Res.* **103**, 31–40.

Basar, E. 1980 *EEG-brain dynamics: relation between EEG and brain evoked potentials*. Amsterdam: Elsevier-North Holland Biomedical.

Belle, V., Delon-Martin, C., Massarelli, R., Decety, J., Le, B., Benabid, A. L. & Segebarth, C. 1995 Intracranial gradient-echo and spin-echo functional MR angiography in humans. *Radiology* **195**, 739–746.

Belliveau, J. W., Kennedy, D. N., McKinstry, R. C., Buchbinder, B. R., Weisskoff, R. M., Cohen, M. S., Vevea, J. M., Brady, T. J. & Rosen, B. R. 1991 Functional mapping of the human visual cortex by magnetic resonance imaging. *Science* **254**, 716–719.

Blake, R. & Logothetis, N. K. 2002 Visual competition. *Nature Rev. Neurosci.* **3**, 13–23.

Bloch, F., Hansen, W. W. & Packard, M. 1946 The nuclear induction experiment. *Phys. Rev.* **70**, 474–485.

Bock, C., Schmitz, B., Kerskens, C. M., Gyngell, M. L., Hossmann, K. A. & Hoehn-Berlage, M. 1998 Functional MRI of somatosensory activation in rat: effect of hypercapnic up-regulation on perfusion- and BOLD-imaging. *Magn. Resonance Med.* **39**, 457–461.

Bonhoeffer, T. & Grinvald, A. 1996 Optical imaging based on intrinsic signals. In *Brain mapping, the methods* (ed. A. W. Toga & J. C. Mazziotta), pp. 55–97. New York: Academic.

Bonmassar, G., Anami, K., Ives, J. & Belliveau, J. W. 1999 Visual evoked potential (VEP) measured by simultaneous 64-channel EEG and 3T fMRI. *NeuroReport* **10**, 1893–1897.

Boxerman, J. L., Bandettini, P. A., Kwong, K. K., Baker, J. R., Davis, T. L., Rosen, B. R. & Weisskoff, R. M. 1995*a* The intravascular contribution to fMRI signal change: Monte Carlo modeling and diffusion-weighted studies *in vivo*. *Magn. Resonance Med.* **34**, 4–10.

Boxerman, J. L., Hamberg, L. M., Rosen, B. R. & Weisskoff, R. M. 1995*b* MR contrast due to intravascular magnetic susceptibility perturbations. *Magn. Resonance Med.* **34**, 555–566.

Braitenberg, V. & Schuez, A. 1998 *Cortex: statistics and geometry of neuronal connectivity*. Berlin: Springer.

Brewer, A. A., Press, W., Logothetis, N. K. & Wandell, B. 2002 Visual areas in macaque cortex measured using functional MRI. *J. Neurosci.* (In the press.)

Brooks, R. A., Battocletti, J. H., Sances, A., Larson, S. J., Bowman, R. L. & Kudravcev, V. 1975 Nuclear magnetic relaxation in blood. *IEEE Trans. Biomed. Engng* **22**, 12–18.

Buchwald, J. S. & Grover, F. S. 1970 Amplitudes of background fast activity characteristic of specific brain sites. *J. Neurophysiol.* **33**, 148–159.

Buchwald, J. S., Hala, E. S. & Schramm, S. A. 1965 Comparison of multi-unit activity and EEG activity recorded from the same brain site in chronic cats during behavioral conditioning. *Nature* **205**, 1012–1014.

Burke, M., Schwindt, W., Ludwig, U., Hennig, J. & Hoehn, M. 2000 Facilitation of electric forepaw stimulation-induced somatosensory activation in rats by additional acoustic stimulation: an fMRI investigation. *Magn. Resonance Med.* **44**, 317–321.

Buxton, R. B. 2001 The elusive initial dip. *Neuroimage* **13**, 953–958.

Buxton, R. B. & Frank, L. R. 1997 A model for the coupling between cerebral blood flow and oxygen metabolism during neural stimulation. *J. Cerebral Blood Flow Metabolism* **17**, 64–72.

Buxton, R. B., Wong, E. C. & Frank, L. R. 1998 Dynamics of blood flow and oxygenation changes during brain activation: the balloon model. *Magn. Resonance Med.* **39**, 855–864.

Buzsaki, G. & Chrobak, J. J. 1995 Temporal structure in spatially organized neuronal ensembles: a role for interneuronal networks. *Curr. Opin. Neurobiol.* **5**, 504–510.

Callaghan, P. T. 1991 *Principles of nuclear magnetic resonance microscopy*. Oxford University Press.

Cannestra, A. F., Pouratian, N., Bookheimer, S. Y., Martin, N. A., Becker, D. P. & Toga, A. W. 2001 Temporal spatial differences observed by functional MRI and human intraoperative optical imaging. *Cerebral Cortex* **11**, 773–782.

Chang, C. & Shyu, B. C. 2001 A fMRI study of brain activations during non-noxious and noxious electrical stimulation of the sciatic nerve of rats. *Brain Res.* **897**, 71–81.

Colby, C. L., Duhamel, J.-R. & Goldberg, M. E. 1993 Ventral intraparietal area of the macaque: anatomic location and visual response properties. *J. Neurophysiol.* **69**, 902–914.

Cormack, A. M. 1973 Reconstruction of densities from their projections, with applications in radiological physics. *Phys. Med. Biol.* **18**, 195–207.

Darian-Smith, C. & Gilbert, C. D. 1995 Topographic reorganization in the striate cortex of the adult cat and monkey is cortically mediated. *J. Neurosci.* **15**, 1631–1647.

Das, A. & Gilbert, C. D. 1995 Receptive field expansion in adult visual cortex is linked to dynamic changes in strength of cortical connections. *J. Neurophysiol.* **74**, 779–792.

Davis, T. L., Kwong, K. K., Weisskoff, R. M. & Rosen, B. R. 1998 Calibrated functional M.R.I: mapping the dynamics of oxidative metabolism. *Proc. Natl Acad. Sci. USA* **95**, 1834–1839.

De Valois, R. L., Yund, E. W. & Hepler, N. 1982 The orientation and direction selectivity of cells in macaque visual cortex. *Vis. Res.* **22**, 531–544.

Desimone, R. & Schein, S. J. 1987 Visual properties of neurons in area V4 of the macaque: sensitivity to stimulus form. *J. Neurophysiol.* **57**, 835–868.

Desimone, R. & Ungerleider, L. G. 1986 Multiple visual areas in the caudal superior temporal sulcus of the macaque. *J. Comp. Neurol.* **248**, 164–189.

Deyoe, E. A., Bandettini, P., Neitz, J., Miller, D. & Winans, P. 1994 Functional magnetic resonance imaging (FMRI) of the human brain. *J. Neurosci. Meth.* **54**, 171–187.

Disbrow, E., Roberts, T. P., Slutsky, D. & Krubitzer, L. 1999 The use of fMRI for determining the topographic organization of cortical fields in human and nonhuman primates. *Brain Res.* **829**, 167–173.

Disbrow, E. A., Slutsky, D. A., Roberts, T. P. & Krubitzer, L. A. 2000 Functional MRI at 1.5 tesla: a comparison of the blood oxygenation level-dependent signal and electrophysiology. *Proc. Natl Acad. Sci. USA* **97**, 9718–9723.

Dow, B. M. 1974 Functional classes of cells and their laminar distribution in monkey visual cortex. *J. Neurophysiol.* **37**, 927–946.

Dubowitz, D. J., Chen, D. Y., Atkinson, D. J., Scadeng, M., Martinez, A., Andersen, M. B., Andersen, R. A. & Bradley, W. G. J. R. 2001 Direct comparison of visual cortex activation in human and non-human primates using functional magnetic resonance imaging. *J. Neurosci. Meth.* **107**, 71–80.

Duvernoy, H. M., Delon, S. & Vannson, J. L. 1981 Cortical blood vessels of the human brain. *Brain Res. Bull.* **7**, 519–579.

Ehman, R. L. & Felmlee, J. P. 1989 Adaptive technique for

high-definition MR imaging of moving structures. *Radiology* **173**, 255–263.

Elul, R. 1969 The physiological interpretation of amplitude histograms of the EEG. *Electroencephalography Clin. Neurophysiol.* **27**, 703–704.

Elul, R. 1971 The genesis of the EEG. *Int. Rev. Neurobiol.* **15**, 227–272.

Engel, S. A., Rumelhart, D. E., Wandell, B. A., Lee, A. T., Glover, G. H., Chichilnisky, E.-J. & Shadlen, M. N. 1994 fMRI of human visual cortex. *Nature* **369**, 525.

Engel, S. A., Glover, G. H. & Wandell, B. A. 1997 Retinotopic organization in human visual cortex and the spatial precision of functional MRI. *Cerebral Cortex* **7**, 181–192.

Ernst, R. R. & Anderson, W. A. 1966 Application of Fourier transform spectroscopy to magnetic resonance. *Rev. Sci. Instrum.* **37**, 93–102.

Ernst, T. & Hennig, J. 1994 Observation of a fast response in functional MR. *Magn. Resonance Med.* **32**, 146–149.

Farmer, T. H., Cofer, G. P. & Johnson, G. A. 1990 Maximizing contrast to noise with inductively coupled implanted coils. *Investigative Radiology* **25**, 552–558.

Felleman, D. J. & Van Essen, D. C. 1983 The connections of area V4 of macaque extrastriate cortex. *Soc. Neurosci. Abstracts* **9**, 153.

Fox, P. T. & Raichle, M. E. 1986 Focal physiological uncoupling of cerebral blood flow and oxidative metabolism during somatosensory stimulation in human subjects. *Proc. Natl Acad. Sci. USA* **83**, 1140–1144.

Fox, P. T., Mintun, M. A., Raichle, M. E., Miezin, F. M., Allman, J. M. & Van Essen, D. C. 1986 Mapping human visual cortex with positron emission tomography. *Nature* **323**, 806–809.

Fox, P. T., Raichle, M. E., Mintun, M. A. & Dence, C. 1988 Nonoxidative glucose consumption during focal physiologic neural activity. *Science* **241**, 462–464.

Frahm, J., Merboldt, K. D., Hanicke, W., Kleinschmidt, A. & Boecker, H. 1994 Brain or vein—oxygenation or flow? On signal physiology in functional MRI of human brain activation. *Nucl. Magn. Resonance Biomed.* **7**, 45–53.

Frahm, J., Kruger, G., Merboldt, K. D. & Kleinschmidt, A. 1996 Dynamic uncoupling and recoupling of perfusion and oxidative metabolism during focal brain activation in man. *Magn. Resonance Med.* **35**, 143–148.

Freeman, W. J. 1975 *Mass action in the nervous system.* New York: Academic.

Fried, I., MacDonald, K. A. & Wilson, C. L. 1997 Single neuron activity in human hippocampus and amygdala during recognition of faces and objects. *Neuron* **18**, 753–765.

Fromm, G. H. & Bond, H. W. 1964 Slow changes in the electrocorticogram and the activity of cortical neurons. *Electroencephalography Clin. Neurophysiol.* **17**, 520–523.

Fromm, G. H. & Bond, H. W. 1967 The relationship between neuron activity and cortical steady potentials. *Electroencephalography Clin. Neurophysiol.* **22**, 159–166.

Frostig, R. D., Lieke, E. E., Ts'o, D. Y. & Grinvald, A. 1990 Cortical functional architecture and local coupling between neuronal activity and the microcirculation revealed by *in vivo* high-resolution optical imaging of intrinsic signals. *Proc. Natl Acad. Sci. USA* **87**, 6082–6086.

Fukushima, E. 1989 *NMR in biomedicine; the physical basis.* New York: American Institute of Physics.

Fulton, J. F. 1928 Observations upon the vascularity of the human occipital lobe during visual activity. *Brain* **51**, 310–320.

Gandhi, S. P., Heeger, D. J. & Boynton, G. M. 1999 Spatial attention affects brain activity in human primary visual cortex. *Proc. Natl Acad. Sci. USA* **96**, 3314–3319.

Garwood, M., Ugurbil, K., Rath, A. R., Bendall, M. R., Ross, B. D., Mitchell, S. L. & Merkle, H. 1989 Magnetic resonance imaging with adiabatic pulses using a single surface coil for RF transmission and signal detection. *Magn. Resonance Med.* **9**, 25–34.

Gasser, H. S. & Grundfest, H. 1939 Axon diameters in relation to the spike dimensions and the conduction velocity in mammalian A fibers. *Am. J. Physiol.* **127**, 393–414.

Gati, J. S., Menon, R. S. & Rutt, B. K. 2000 Field strength dependence of functional MRI signals. In *Functional MRI* (ed. C. T. Moonen & P. A. Bandettini), pp. 277–282. Berlin: Springer.

Glover, G. H. & Lai, S. 1998 Self-navigated spiral fMRI: interleaved versus single-shot. *Magn. Resonance Med.* **39**, 361–368.

Glover, G. H. & Lee, A. T. 1995 Motion artifacts in fMRI: comparison of 2DFT with PR and spiral scan methods. *Magn. Resonance Med.* **33**, 624–635.

Goldberg, M. E. & Wurtz, R. H. 1972 Activity of superior colliculus in behaving monkey. I. Visual receptive fields of single neurons. *J. Neurophysiol.* **35**, 542–559.

de Graaf, R. A. 1998 *In vivo NMR spectroscopy: principles and techniques.* Chichester: Wiley.

Granger, R. & Lynch, G. 1991 Higher olfactory processes: perceptual learning and memory. *Curr. Opin. Neurobiology* **1**, 209–214.

Gray, C. M. & McCormick, D. A. 1996 Chattering cells—superficial pyramidal neurons contibuting to the generation of synchronous oscillations in the visual cortex. *Science* **274**, 109–113.

Gray, C. M., Maldonado, P. E., Wilson, M. & McNaughton, B. 1995 Tetrodes markedly improve the reliability and yield of multiple single-unit isolation from multi-unit recordings in cat striate cortex. *J. Neurosci. Meth.* **63**, 43–54.

Gray, J. A. & Ball, G. G. 1970 Frequency-specific relation between hippocampal theta rhythm, behavior, and amobarbital action. *Science* **168**, 1246–1248.

Grill-Spector, K., Kushnir, T., Edelman, S., Avidan, G., Itzchak, Y. & Malach, R. 1999 Differential processing of objects under various viewing conditions in the human lateral occipital complex. *Neuron* **24**, 187–203.

Grover, F. S. & Buchwald, J. S. 1970 Correlation of cell size with amplitude of background fast activity in specific brain nuclei. *J. Neurophysiol.* **33**, 160–171.

Gruetter, R., Boesch, C., Martin, E. & Wuthrich, K. 1990 A method for rapid evaluation of saturation factors in *in vivo* surface coil NMR spectroscopy using B1-insensitive pulse cycles. *NMR Biomed.* **3**, 265–271.

Haacke, E. M., Lai, S., Yablonskiy, D. A. & Lin, W. L. 1995 *In vivo* validation of the BOLD mechanism—a review of signal changes in gradient echo functional MRI in the presence of flow. *Int. J. Imaging Systems Technology* **6**, 153–163.

Haacke, E. M., Brown, R. W., Thompson, M. R. & Venkatesan, R. 1999 *Magnetic resonance imaging: principles and sequence design.* New York: Wiley-Liss.

Haase, A., Frahm, J., Matthaei, D., Hanicke, W. & Merboldt, K.-D. 1986 FLASH imaging. Rapid NMR imaging using low flip-angle pulses. *J. Magn. Resonance* **67**, 258–266.

Hahn, E. L. 1950 Spin echoes. *Phys. Rev.* **80**, 580–594.

Hawken, M. J., Parker, A. J. & Lund, J. S. 1988 Laminar organization and contrast sensitivity of direction-selective cells in the striate cortex of the Old World monkey. *J. Neurosci.* **8**, 3541–3548.

He, S., Cohen, E. R. & Hu, X. P. 1998 Close correlation between activity in brain area MT/V5 and the perception of a visual-motion after effect. *Curr. Biol.* **8**, 1215–1218.

Heeger, D. J. & Ress, D. 2002 What does fMRI tell us about neuronal activity? *Nature Rev. Neurosci.* **3**, 142–151.

Heeger, D. J., Huk, A. C., Geisler, W. S. & Albrecht, D. G. 2000 Spikes versus BOLD: what does neuroimaging tell us about neuronal activity? *Nature Neurosci.* **3**, 631–633.

Hendrich, K., Xu, Y., Kim, S. G. & Ugurbil, K. 1994 Surface coil cardiac tagging and ^{31}P spectroscopic localization with B1-insensitive adiabatic pulses. *Magn. Resonance Med.* **31**, 541–545.

Henze, D. A., Borhegyi, Z., Csicsvari, J., Mamiya, A., Harris, K. D. & Buzsaki, G. 2000 Intracellular features predicted by extracellular recordings in the hippocampus *in vivo*. *J. Neurophysiol.* **84**, 390–400.

Hess, A., Stiller, D., Kaulisch, T., Heil, P. & Scheich, H. 2000 New insights into the hemodynamic blood oxygenation level-dependent response through combination of functional magnetic resonance imaging and optical recording in gerbil barrel cortex. *J. Neurosci.* **20**, 3328–3338.

Hoffmann, E. J., Phelps, M. E., Mullani, N. A., Higgins, C. S. & Ter Pogossian, M. M. 1976 Design and performance characteristics of a whole-body positron transaxial tomograph. *J. Nucl. Med.* **17**, 493–502.

Hoogenraad, F. G., Pouwels, P. J., Hofman, M. B., Reichenbach, J. R., Sprenger, M. & Haacke, E. M. 2001 Quantitative differentiation between BOLD models in fMRI. *Magn. Resonance Med.* **45**, 233–246.

Hsu, E. W., Hedlund, L. F. & MacFall, J. R. 1998 Functional MRI of the rat somatosensory cortex—effects of hyperventilation. *Magn. Resonance Med.* **40**, 421–426.

Hu, X. & Kim, S. G. 1994 Reduction of signal fluctuation in functional MRI using navigator echoes. *Magn. Resonance Med.* **31**, 495–503.

Hu, X., Le, T. H. & Ugurbil, K. 1997 Evaluation of the early response in fMRI in individual subjects using short stimulus duration. *Magn. Resonance Med.* **37**, 877–884.

Huang, C. M. & Buchwald, J. S. 1977 Interpretation of the vertex short-latency acoustic response: a study of single neurons in the brain stem. *Brain Res.* **137**, 291–303.

Humphrey, D. R. & Corrie, W. S. 1978 Properties of pyramidal tract neuron system within a functionally defined subregion of primate motor cortex. *J. Neurophysiol.* **41**, 216–243.

Hunt, C. 1951 The reflex activity of mammalian small-nerve fibres. *J. Physiol. Lond.* **115**, 456–469.

Hyde, J. S., Jesmanowicz, A., Grist, T. M., Froncisz, W. & Kneeland, J. B. 1987 Quadrature detection surface coil. *Magn. Resonance Med.* **4**, 179–184.

Hyde, J. S., Biswal, B. B. & Jesmanowicz, A. 2001 High-resolution fMRI using multislice partial k-space GR-EPI with cubic voxels. *Magn. Resonance Med.* **46**, 114–125.

Hyder, F., Shulman, R. G. & Rothman, D. L. 1998 A model for the regulation of cerebral oxygen delivery. *J. Appl. Physiol.* **85**, 554–564.

Jezzard, P., Rauschecker, J. P. & Malonek, D. 1997 An *in vivo* model for functional MRI in cat visual cortex. *Magn. Resonance Med.* **38**, 699–705.

Johnston, D. & Wu, S. M. 1995 *Foundations of cellular neurophysiology*. Cambridge, MA: MIT Press.

Jones, M., Berwick, J., Johnston, D. & Mayhew, J. 2001 Concurrent optical imaging spectroscopy and laser-Doppler flowmetry: the relationship between blood flow, oxygenation, and volume in rodent barrel cortex. *Neuroimage* **13**, 1002–1015.

Jueptner, M. & Weiller, C. 1995 Review—does measurement of regional cerebral blood flow reflect synaptic activity—implications for PET and fMRI. *Neuroimage* **2**, 148–156.

Juergens, E., Eckhorn, R., Frien, A. & Woelbern, T. 1996 *Brain and evolution*, p. 418. Berlin: Thieme.

Juergens, E., Guettler, A. & Eckhorn, R. 1999 Visual stimulation elicits locked and induced gamma oscillations in monkey intracortical- and EEG-potentials, but not in human EEG. *Exp. Brain Res.* **129**, 247–259.

Kaas, J. H., Krubitzer, L. A., Chino, Y. M., Langston, A. L., Polley, E. H. & Blair, N. 1990 Reorganization of retinotopic cortical maps in adult mammals after lesions of the retina. *Science* **248**, 229.

Kadekaro, M., Crane, A. M. & Sokoloff, L. 1985 Differential effects of electrical stimulation of sciatic nerve on metabolic activity in spinal cord and dorsal root ganglion in the rat. *Proc. Natl Acad. Sci. USA* **82**, 6010–6013.

Kadekaro, M., Vance, W. H., Terrell, M. L., Gary, H. J., Eisenberg, H. M. & Sokoloff, L. 1987 Effects of antidromic stimulation of the ventral root on glucose utilization in the ventral horn of the spinal cord in the rat. *Proc. Natl Acad. Sci. USA* **84**, 5492–5495.

Kamada, K., Pekar, J. J. & Kanwal, J. S. 1999 Anatomical and functional imaging of the auditory cortex in awake mustached bats using magnetic resonance technology. *Brain Res. Brain Res. Protocols* **4**, 351–359.

Kandel, A. & Buzsaki, G. 1997 Cellular-synaptic generation of sleep spindles, spike-and-wave discharges, and evoked thalamocortical responses in the neocortex of the rat. *J. Neurosci.* **17**, 6783–6797.

Kastner, S. & Ungerleider, L. G. 2000 Mechanisms of visual attention in the human cortex. *A. Rev. Neurosci.* **23**, 315–341.

Kastner, S., De Weerd, P., Desimone, R. & Ungerleider, L. G. 1998 Mechanisms of directed attention in the human extrastriate cortex as revealed by functional MRI. *Science* **282**, 108–111.

Kennan, R. P., Zhong, J. & Gore, J. C. 1994 Intravascular susceptibility contrast mechanisms in tissues. *Magn. Resonance Med.* **31**, 9–21.

Kennan, R. P., Scanley, B. E. & Gore, J. C. 1997 Physiologic basis for BOLD MR signal changes due to hypoxia/hyperoxia: separation of blood volume and magnetic susceptibility effects. *Magn. Resonance Med.* **37**, 953–956.

Kennan, R. P., Scanley, B. E., Innis, R. B. & Gore, J. C. 1998 Physiological basis for BOLD MR signal changes due to neuronal stimulation: separation of blood volume and magnetic susceptibility effects. *Magn. Resonance Med.* **40**, 840–846.

Kety, S. S. & Schmidt, C. F. 1948 Nitrous oxide method for the quantitative determination of cerebral blood flow in man: theory, procedure, and normal values. *J. Clin. Investigations* **27**, 475–483.

Kim, D. S., Duong, T. Q. & Kim, S. G. 2000 Reply to: can current fMRI techniques reveal the micro-architecture of cortex? *Nature Neurosci.* **3**, 414.

Kim, S. G., Hendrich, K., Hu, X., Merkle, H. & Ugurbil, K. 1994 Potential pitfalls of functional MRI using conventional gradient-recalled echo techniques. *Nucl. Magn. Resonance Biomed.* **7**, 69–74.

Kim, S. G. & Ugurbil, K. 1997 Comparison of blood oxygenation and cerebral blood flow effects in fMRI: estimation of relative oxygen consumption change. *Magn. Resonance Med.* **38**, 59–65.

Kim, S. G., Hu, X., Adriany, G. & Ugurbil, K. 1996 Fast interleaved echo-planar imaging with navigator: high resolution anatomic and functional images at 5 Tesla. *Magn. Resonance Med.* **35**, 895–902.

Koch, C. 1999 *Biophysics of computation: information processing in single neurons*. New York: Oxford University Press.

Kocsis, B., Bragin, A. & Buzsaki, G. 1999 Interdependence of multiple theta generators in the hippocampus: a partial coherence analysis. *J. Neurosci.* **19**, 6200–6212.

Kourtzi, Z. & Kanwisher, N. 2001 Representation of perceived object shape by the human lateral occipital complex. *Science* **293**, 1506–1509.

Krakow, K., Woermann, F. G., Symms, M. R., Allen, P. J., Lemieux, L., Barker, G. J., Duncan, J. S. & Fish, D. R. 1999 EEG-triggered functional MRI of interictal epileptiform

activity in patients with partial seizures. *Brain* **122**, 1679–1688.

Krakow, K., Allen, P. J., Symms, M. R., Lemieux, L., Josephs, O. & Fish, D. R. 2000 EEG recording during fMRI experiments: image quality. *Hum. Brain Mapping* **10**, 10–15.

Kreiman, G., Koch, C. & Fried, I. 2000*a* Imagery neurons in the human brain. *Nature* **408**, 357–361.

Kreiman, G., Koch, C. & Fried, I. 2000*b* Category-specific visual responses of single neurons in the human medial temporal lobe. *Nature Neurosci.* **3**, 946–953.

Kruger, G., Kleinschmidt, A. & Frahm, J. 1996 Dynamic MRI sensitized to cerebral blood oxygenation and flow during sustained activation of human visual cortex. *Magn. Resonance Med.* **35**, 797–800.

Kwong, K. K., Belliveau, J. W., Chesler, D. A., Goldberg, I. E., Weisskoff, R. M., Poncelet, B. P., Kennedy, D. N., Hoppel, B. E., Cohen, M. S. & Turner, R. 1992 Dynamic magnetic resonance imaging of human brain activity during primary sensory stimulation. *Proc. Natl Acad. Sci. USA* **89**, 5675–5679.

Lahti, K. M., Ferris, C. F., Li, F. H., Sotak, C. H. & King, J. A. 1998 Imaging brain activity in conscious animals using functional MRI. *J. Neurosci. Meth.* **82**, 75–83.

Laurent, G. & Davidowitz, H. 1994 Encoding of olfactory information with oscillating neural assemblies. *Science* **265**, 1872–1875.

Laurent, G., Stopfer, M., Friedrich, R. W., Rabinovich, M. I., Volkovskii, A. & Abarbanel, H. D. 2001 Odor encoding as an active, dynamical process: experiments, computation, and theory. *A. Rev. Neurosci.* **24**, 263–297.

Lauterbur, P. C. 1973 Image formation by induced local interactions: examples emplying nuclear magnetic resonance. *Nature* **242**, 190–191.

Le, B., Hassler, M., Reutenauer, H., Decorps, M., Camuset, J. P., Crouzet, G. & Benabid, A. L. 1987 MRI of the cervical spine. Creation of a surface coil. Technical and clinical results. *J. Radiologie* **68**, 579–586.

Lee, S. P., Duong, T. Q., Yang, G., Iadecola, C. & Kim, S. G. 2001 Relative changes of cerebral arterial and venous blood volumes during increased cerebral blood flow: implications for BOLD fMRI. *Magn. Resonance Med.* **45**, 791–800.

Legatt, A. D., Arezzo, J. & Vaughan, H. G. J. 1980 Averaged multiple unit activity as an estimate of phasic changes in local neuronal activity: effects of volume-conducted potentials. *J. Neurosci. Meth.* **2**, 203–217.

Lindauer, U., Royl, G., Leithner, C., Kuhl, M., Gold, L., Gethmann, J., Kohl-Bareis, M., Villringer, A. & Dirnagl, U. 2001 No evidence for early decrease in blood oxygenation in rat whisker cortex in response to functional activation. *Neuroimage* **13**, 988–1001.

Lindsley, D. B. & Wicke, J. D. 1974 The electroencephalogram: autonomous electrical activity in man and animals. In *Electroencephalography and human brain potentials* (ed. R. F. Thomson & M. M. Patterson), pp. 3–83. New York: Academic.

Logothetis, N. K. 2000 Can current fMRI techniques reveal the microarchitecture of cortex? *Nature Neurosci.* **3**, 413.

Logothetis, N. K., Guggenberger, H., Peled, S. & Pauls, J. 1999 Functional imaging of the monkey brain. *Nature Neurosci.* **2**, 555–562.

Logothetis, N. K., Peled, S. & Pauls, J. 1998 Development and application of fMRI for visual studies in monkeys. *Soc. Neurosci. Abstracts* **24**, 11.

Logothetis, N. K., Pauls, J., Augath, M., Trinath, T. & Oeltermann, A. 2001 Neurophysiological investigation of the basis of the fMRI signal. *Nature* **412**, 150–157.

Logothetis, N. K., Merkle, H., Augath, M., Trinath, T. & Ugurbil, K. 2002 Ultra-high resolution fMRI in monkeys with implanted RF coils. *Neuron* **35**, 227–242.

Lopez-Villegas, D., Kimura, H., Tunlayadechanont, S. & Lenkinski, R. E. 1996 High spatial resolution MRI and proton MRS of human frontal cortex. *Nucl. Magn. Resonance Biomed.* **9**, 297–304.

Lorente de Nó, R. 1947 Analysis of the distribution of action currents of nerve in volume conductors. *Studies Rockefeller Inst. Med. Res.* **132**, 384–477.

Luck, S. J., Chelazzi, L., Hillyard, S. A. & Desimone, R. 1997 Neural mechanisms of spatial selective attention in areas V1, V2 and V4 of macaque visual cortex. *J. Neurophysiol.* **77**, 24–42.

Lund, J. S., Yoshioka, T. & Levitt, J. B. 1994 Substrates for interlaminar connections in area V1 of macaque monkey cerebral cortex. In *Primary visual cortex in primates* (ed. A. Peters & K. S. Rockland), pp. 37–60. New York: Plenum Press.

Luo, Y., de, G., DelaBarre, L., Tannus, A. & Garwood, M. 2001 BISTRO: an outer-volume suppression method that tolerates RF field inhomogeneity. *Magn. Resonance Med.* **45**, 1095–1102.

McAdams, C. J. & Maunsell, J. H. 1999 Effects of attention on orientation-tuning functions of single neurons in macaque cortical area V4. *J. Neurosci.* **19**, 431–441.

McArdle, C. B., Crofford, M. J., Mirfakhraee, M., Amparo, E. G. & Calhoun, J. S. 1986 Surface coil M.R. of spinal trauma: preliminary experience. *Am. J. Neuroradiology* **7**, 885–893.

Magistretti, P. J. & Pellerin, L. 1999 Cellular mechanisms of brain energy metabolism and their relevance to functional brain imaging. *Phil. Trans. R. Soc. Lond.* B **354**, 1155–1163. (DOI 10.1098/rstb.1999.0471.)

Magistretti, P. J., Pellerin, L., Rothman, D. L. & Shulman, R. G. 1999 Neuroscience—energy on demand. *Science* **283**, 496–497.

Malonek, D. & Grinvald, A. 1996 Interactions between electrical activity and cortical microcirculation revealed by imaging spectroscopy: implications for functional brain mapping. *Science* **272**, 551–554.

Malonek, D., Dirnagl, U., Lindauer, U., Yamada, K., Kanno, I. & Grinvald, A. 1997 Vascular imprints of neuronal activity: relationships between the dynamics of cortical blood flow, oxygenation, and volume changes following sensory stimulation. *Proc. Natl Acad. Sci. USA* **94**, 14 826–14 831.

Mandeville, J. B., Marota, J. J., Ayata, C., Zaharchuk, G., Moskowitz, M. A., Rosen, B. R. & Weisskoff, R. M. 1999*a* Evidence of a cerebrovascular postarteriole windkessel with delayed compliance. *J. Cerebral Blood Flow Metabolism* **19**, 679–689.

Mandeville, J. B., Marota, J. J., Ayata, C., Moskowitz, M. A., Weisskoff, R. M. & Rosen, B. R. 1999*b* MRI measurement of the temporal evolution of relative CMRO2 during rat forepaw stimulation. *Magn. Resonance Med.* **42**, 944–951.

Mandeville, J. B., Jenkins, B. G., Kosofsky, B. E., Moskowitz, M. A., Rosen, B. R. & Marota, J. J. 2001 Regional sensitivity and coupling of BOLD and CBV changes during stimulation of rat brain. *Magn. Resonance Med.* **45**, 443–447.

Mansfield, P. 1977 Multi-planar image formation using N.M.R. spin echoes. *J. Phys.* C **10**, L55–L58.

Marota, J. J., Ayata, C., Moskowitz, M. A., Weisskoff, R. M., Rosen, B. R. & Mandeville, J. B. 1999 Investigation of the early response to rat forepaw stimulation. *Magn. Resonance Med.* **41**, 247–252.

Martin, E., Joeri, P., Loenneker, T., Ekatodramis, D., Vitacco, D., Hennig, J. & Marcar, V. L. 1999 Visual processing in infants and children studied using functional MRI. *Pediatric Res.* **46**, 135–140.

Martin, K. A. C. 1988 From single cells to simple circuits in the cerebral cortex. *Q. J. Exp. Psychol.* **73**, 637–702.

Mathiesen, C., Caesar, K., Akgoren, N. & Lauritzen, M. 1998 Modification of activity-dependent increases of cerebral

blood flow by excitatory synaptic activity and spikes in rat cerebellar cortex. *J. Physiol.* **512**, 555–566.

Mathiesen, C., Caesar, K. & Lauritzen, M. 2000 Temporal coupling between neuronal activity and blood flow in rat cerebellar cortex as indicated by field potential analysis. *J. Physiol.* **523** (Pt. 1), 235–246.

Matwiyoff, A. M. & Brooks, W. M. 1999 Instrumentation. In *Magnetic resonance imaging* (ed. D. D. Stark & W. Bradley), pp. 15–32. St Louis, MO: Mosby.

Maunsell, J. H. & Van Essen, D. C. 1983 The connections of the middle temporal visual area (MT) and their relationship to a cortical hierarchy in the macaque monkey. *J. Neurosci.* **3**, 2563–2586.

Mayhew, J., Johnston, D., Martindale, J., Jones, M., Berwick, J. & Zheng, Y. 2001 Increased oxygen consumption following activation of brain: theoretical footnotes using spectroscopic data from barrel cortex. *Neuroimage* **13**, 975–987.

Menon, R. S., Ogawa, S., Tank, D. W. & Ugurbil, K. 1993 4 Tesla gradient recalled echo characteristics of photic stimulation-induced signal changes in the human primary visual cortex. *Magn. Resonance Med.* **30**, 380–386.

Menon, R. S., Ogawa, S., Hu, X., Strupp, J. P., Anderson, P. & Ugurbil, K. 1995 BOLD based functional MRI at 4 Tesla includes a capillary bed contribution: echo-planar imaging correlates with previous optical imaging using intrinsic signals. *Magn. Resonance Med.* **33**, 453–459.

Menon, V., Ford, J. M., Lim, K. O., Glover, G. H. & Pfefferbaum, A. 1997 Combined event-related fMRI and EEG evidence for temporal-parietal cortex activation during target detection. *NeuroReport* **8**, 3029–3037.

Merkle, H., Garwood, M., and Ugurbil, K. 1993 Dedicated circularly polarized surface coil assemblies for brain studies at 4 Tesla. In *Proc. SMRM, 12th Annual Meeting, New York*, p. 1358.

Mitzdorf, U. 1987 Properties of the evoked potential generators: current source-density analysis of visually evoked potentials in the cat cortex. *Int. J. Neurosci.* **33**, 33–59.

Mosso, A. 1881 *Ueber den Kreislauf des Blutes im Menschlichen Gehirn.* Leipzig: Verlag von Veit.

Mountcastle, V. B., Steinmetz, M. A. & Romo, R. 1990 Frequency discrimination in the sense of flutter: psychophysical measurements correlated with postcentral events in behaving monkeys. *J. Neurosci.* **10**, 3032–3044.

Nakahara, K., Hayashi, T., Konishi, S. & Miyashita, Y. 2002 Functional MRI of macaque monkeys performing a cognitive set-shifting task. *Science* **295**, 1532–1536.

Nelson, P. G. 1966 Interaction between spinal motoneurons of the cat. *J. Neurophysiol.* **29**, 275–287.

Nicholson, C. & Llinas, R. 1971 Field potentials in the alligator cerebellum and theory of their relationship to Purkinje cell dendritic spikes. *J. Neurophysiol.* **34**, 509–531.

Nudo, R. J. & Masterton, R. B. 1986 Stimulation-induced [14]C2-deoxyglucose labeling of synaptic activity in the central auditory system. *J. Comp. Neurol.* **245**, 553–565.

Obata, S., Obata, J., Das, A. & Gilbert, C. D. 1999 Molecular correlates of topographic reorganization in primary visual cortex following retinal lesions. *Cerebral Cortex* **9**, 238–248.

Ogawa, S. & Lee, T. M. 1990 Magnetic resonance imaging of blood vessels at high fields: *in vivo* and *in vitro* measurements and image simulation. *Magn. Resonance Med.* **16**, 9–18.

Ogawa, S., Lee, T. M., Nayak, A. S. & Glynn, P. 1990a Oxygenation-sensitive contrast in magnetic resonance image of rodent brain at high magnetic fields. *Magn. Resonance Med.* **14**, 68–78.

Ogawa, S., Lee, T. M., Kay, A. R. & Tank, D. W. 1990b Brain magnetic resonance imaging with contrast dependent on blood oxygenation. *Proc. Natl Acad. Sci. USA* **87**, 9868–9872.

Ogawa, S., Tank, D. W., Menon, R., Ellermann, J. M., Kim, S. G., Merkle, H. & Ugurbil, K. 1992 Intrinsic signal changes accompanying sensory stimulation: functional brain mapping with magnetic resonance imaging. *Proc. Natl Acad. Sci. USA* **89**, 5951–5955.

Ogawa, S., Menon, R. S., Tank, D. W., Kim, S. G., Merkle, H., Ellermann, J. M. & Ugurbil, K. 1993 Functional brain mapping by blood oxygenation level-dependent contrast magnetic resonance imaging. A comparison of signal characteristics with a biophysical model. *Biophys. J.* **64**, 803–812.

Ogawa, S., Menon, R. S., Kim, S. G. & Ugurbil, K. 1998 On the characteristics of functional magnetic resonance imaging of the brain. *A. Rev. Biophys. Biomol. Struct.* **27**, 447–474.

Pan, J. W. (and 10 others) 2000 Spectroscopic imaging of glutamate C4 turnover in human brain. *Magn. Resonance Med.* **44**, 673–679.

Pauling, L. & Coryell, C. 1936 The magnetic properties and structure of hemogblogin. *Proc. Natl Acad. Sci. USA* **22**, 210–216.

Pedemonte, M., Barrenechea, C., Nunez, A., Gambini, J. P. & Garcia-Austt, E. 1998 Membrane and circuit properties of lateral septum neurons: relationships with hippocampal rhythms. *Brain Res.* **800**, 145–153.

Pedley, T. A. & Traub, R. D. 1990 Physiological basis of the EEG. In *Current practice of clinical electroencephalography* (ed. D. D. Daly & T. A. Pedley), pp. 107–137. New York: Raven Press.

Pellerin, L. & Magistretti, P. J. 1994 Glutamate uptake into astrocytes stimulates aerobic glycolysis: a mechanism coupling neuronal activity to glucose utilization. *Proc. Natl Acad. Sci. USA* **91**, 10 625–10 629.

Pfeuffer, J., Van, D., Ugurbil, K., Hu, X. P. & Glover, G. H. 2002a Correction of physiologically induced global off resonance effects in dynamic echo-planar and spiral functional imaging. *Magn. Resonance Med.* **47**, 344–353.

Pfeuffer, J., Van de Moortele, Yacoub, E., Shmuel, A., Adriany, G., Andersen, P., Merkle, H., Garwood, M., Hu, X. & Ugurbil, K. 2002b Zoomed functional imaging in the human brain at 7 Tesla with simultaneous high spatial and high temporal resolution. *Neuroimage* (In the press.)

Phelps, M. E., Hoffman, E. J., Mullani, N. A. & Ter Pogossian, M. M. 1975 Application of annihilation coincidence detection to transaxial reconstruction tomography. *J. Nucl. Med.* **16**, 210–224.

Polonsky, A., Blake, R., Braun, J. & Heeger, D. J. 2000 Neuronal activity in human primary visual cortex correlates with perception during binocular rivalry. *Nature Neurosci.* **3**, 1153–1159.

Purcell, E. M., Torrey, H. C. & Pound, C. V. 1946 Resonance absorption by nuclear magnetic moments in a solid. *Physiol. Rev.* **64**, 37–38.

Rabi, I. I., Zacharias, J. R., Millman, S. & Kusch, P. 1938 A new method for measuring nuclear magnetic moment. *Phys. Rev.* **55**, 526–535.

Rabi, I. I., Millman, S. & Kusch, P. 1939 The molecular beam resonance method for measuring nuclear magnetic moments. *Phys. Rev.* **55**, 643–674.

Raichle, M. E. 2000 A brief history of human functional brain mapping. In *The systems* (ed. A. W. Toga & J. C. Mazziotta), pp. 33–75. San Diego: Academic.

Raichle, M. E., Grubb, R. L. J., Eichling, J. O. & Ter Pogossian, M. M. 1976 Measurement of brain oxygen utilization with radioactive oxygen-15, experimental verification. *J. Appl. Physiol.* **40**, 638–640.

Rainer, G., Augath, M., Trinath, T. & Logothetis, N. K. 2001 Nonmonotonic noise tuning of BOLD fMRI signal to natural images in the visual cortex of the anesthetized monkey. *Curr. Biol.* **11**, 846–854.

Raisman, G. 1966 The connexions of the septum. *Brain* **89**, 317–348.

Rall, W. 1962 Electrophysiology of a dendritic neuron. *Biophys. J.* **2**, 145–167.

Recanzone, G. H., Merzenich, M. M. & Schreiner, C. E. 1992 Changes in the distributed temporal response properties of SI cortical neurons reflect improvements in performance on a temporally based tactile discrimination task. *J. Neurophysiol.* **67**, 1071–1091.

Rees, G., Friston, K. & Koch, C. 2000 A direct quantitative relationship between the functional properties of human and macaque V5. *Nature Neurosci.* **3**, 716–723.

Ress, D., Backus, B. T. & Heeger, D. J. 2000 Activity in primary visual cortex predicts performance in a visual detection task. *Nature Neurosci.* **3**, 940–945.

Roemer, P. B., Edelstein, W. A., Hayes, C. E., Souza, S. P. & Mueller, O. M. 1990 The NMR phased array. *Magn. Resonance Med.* **16**, 192–225.

Romo, R. & Salinas, E. 1999 Sensing and deciding in the somatosensory system. *Curr. Opin. Neurobiol.* **9**, 487–493.

Rosen, B. R., Belliveau, J. W., Aronen, H. J., Kennedy, D., Buchbinder, B. R., Fischman, A., Gruber, M., Glas, J., Weisskoff, R. M. & Cohen, M. S. 1991 Susceptibility contrast imaging of cerebral blood volume: human experience. *Magn. Resonance Med.* **22**, 293–299.

Rothman, D. L., Sibson, N. R., Hyder, F., Shen, J., Behar, K. L. & Shulman, R. G. 1999 *In vivo* nuclear magnetic resonance spectroscopy studies of the relationship between the glutamate–glutamine neurotransmitter cycle and functional neuroenergetics. *Phil. Trans. R. Soc. Lond.* B **354**, 1165–1177. (DOI 10.1098/rstb.1999.0472.)

Roy, C. S. & Sherrington, C. S. 1890 On the regulation of the blood supply of the brain. *J. Physiol. Lond.* **11**, 85–108.

Rudin, M. 1987 MR microscopy on rats in vivo at 4.7 T using surface coils. *Magn. Resonance Med.* **5**, 443–448.

Schiller, P. H., Finlay, B. L. & Volman, S. F. 1976 Quantitative studies of single-cell properties in monkey striate cortex. I. Spatiotemporal organization of receptive fields. *J. Neurophysiol.* **39**, 1288–1319.

Schmitt, F., Stehling, M. K. & Turner, R. 1998 *Echo-planar imaging: theory, technique and application*. Berlin: Springer.

Segebarth, C., Belle, V., Delon, C., Massarelli, R., Decety, J., Le, B., Decorps, M. & Benabid, A. L. 1994 Functional MRI of the human brain: predominance of signals from extracerebral veins. *NeuroReport* **5**, 813–816.

Sereno, M. E., Trinath, T., Augath, M. & Logothetis, N. K. 2002 Three-dimensional shape representation in monkey cortex. *Neuron* **33**, 635–652.

Sereno, M. I., Dale, A. M., Reppas, J. B., Kwong, K. K., Belliveau, J. W., Brady, T. J., Rosen, B. R. & Tootell, R. B. 1995 Borders of multiple visual areas in humans revealed by functional magnetic resonance imaging. *Science* **268**, 889–893.

Shulman, G. L., Corbetta, M., Buckner, R. L., Raichle, M. E., Fiez, J. A., Miezin, F. M. & Petersen, S. E. 1997 Top–down modulation of early sensory cortex. *Cerebral Cortex* **7**, 193–206.

Shulman, R. G. & Rothman, D. L. 1998 Interpreting functional imaging studies in terms of neurotransmitter cycling. *Proc. Natl Acad. Sci. USA* **95**, 11 993–11 998.

Sibson, N. R., Dhankhar, A., Mason, G. F., Rothman, D. L., Behar, K. L. & Shulman, R. G. 1998 Stoichiometric coupling of brain glucose metabolism and glutamatergic neuronal activity. *Proc. Natl Acad. Sci. USA* **95**, 316–321.

Siesjo, B. o. K. 1978 *Brain energy metabolism*. New York: Wiley.

Silva, L. R., Amitai, Y. & Connors, B. W. 1991 Intrinsic oscillations of neocortex generated by layer 5 pyramidal neurons. *Science* **251**, 432–435.

Silver, X., Ni, W. X., Mercer, E. V., Beck, B. L., Bossart, E. L., Inglis, B. & Mareci, T. H. 2001 *In vivo* H-1 magnetic resonance imaging and spectroscopy of the rat spinal cord using an inductively-coupled chronically implanted RF coil. *Magn. Resonance Med.* **46**, 1216–1222.

Sokoloff, L. 1960 The metabolism of the central nervous system *in vivo*. In *Handbook of physiology–neurophysiology* (ed. J. Field, H. W. Magoun & V. E. Hall), pp. 1843–1864. Washington, DC: American Physiological Society.

Sokoloff, L. 1977 Relation between physiological function and energy metabolism in the central nervous system. *J. Neurochem.* **29**, 13–26.

Sokoloff, L. 1981 Relationships among local functional activity, energy metabolism, and blood flow in the central nervous system. *Fed. Proc. Fedn Am. Socs Exp. Biol.* **40**, 2311–2316.

Sokoloff, L. 1989 Circulation and energy metabolism of the brain. In *Basic neurochemistry* (ed. G. Siegel, B. Agranoff, R. W. Albers & P. Molinoff), pp. 565–590. New York: Raven Press.

Sokoloff, L., Reivich, M., Kennedy, C., DesRosiers, M. H., Patlak, C. S., Pettigrew, K. D., Sakurada, O. & Shinohara, M. 1977 The [C14]deoxyglucose method for the measurement of local cerebral glucose utilization: theory, procedure and normal values in the conscious and anesthetized albino rat. *J. Neurochem.* **28**, 897–916.

Stark, D. D. & Bradley, W. 1999 *Magnetic resonance imaging*. St Louis, MO: Mosby.

Steele, G. E., Weller, R. E. & Cusick, C. G. 1991 Cortical connections of the caudal subdivision of the dorsolateral area (V4) in monkeys. *J. Comp. Neurol.* **306**, 495–520.

Steriade M. 1991 Alertness, quiet sleep, dreaming. In *Cerebral cortex*, pp. 279–357. New York: Plenum.

Steriade, M. & Hobson, J. 1976 Neuronal activity during the sleep–waking cycle. *Progr. Neurobiol.* **6**, 155–376.

Steriade, M., McCormick, D. A. & Sejnowski, T. J. 1993 Thalamocortical oscillations in the sleeping and aroused brain. *Science* **262**, 679–685.

Summers, R. M., Hedlund, L. W., Cofer, G. P., Gottsman, M. B., Manibo, J. F. & Johnson, G. A. 1995 MR microscopy of the rat carotid artery after balloon injury by using an implanted imaging coil. *Magn. Resonance Med.* **33**, 785–789.

Szentagothai, J. 1978 The Ferrier Lecture, 1977. The neuron network of the cerebral cortex: a functional interpretation. *Proc. R. Soc. Lond.* B **201**, 219–248.

Takahashi, S., Driscoll, B. F., Law, M. J. & Sokoloff, L. 1995 Role of sodium and potassium ions in regulation of glucose metabolism in cultured astroglia. *Proc. Natl Acad. Sci. USA* **92**, 4616–4620.

Ter Pogossian, M. M., Eichling, J. O., Davis, D. O., Welch, M. J. & Metzger, J. M. 1969 The determination of regional cerebral blood flow by means of water labeled with radioactive oxygen 15. *Radiology* **93**, 31–40.

Ter Pogossian, M. M., Eichling, J. O., Davis, D. O. & Welch, M. J. 1970 The measure *in vivo* of regional cerebral oxygen utilization by means of oxyhemoglobin labeled with radioactive oxygen-15. *J. Clin. Invest.* **49**, 381–391.

Ter Pogossian, M. M., Phelps, M. E., Hoffman, E. J. & Mullani, N. A. 1975 A positron-emission transaxial tomograph for nuclear imaging (PETT). *Radiology* **114**, 89–98.

Tolias, A. S., Smirnakis, S. M., Augath, M. A., Trinath, T. & Logothetis, N. K. 2001 Motion processing in the macaque: revisited with functional magnetic resonance imaging. *J. Neurosci.* **21**, 8594–8601.

Tong, F., Nakayama, K., Vaughan, J. T. & Kanwisher, N. 1998 Binocular-rivalry and visual awareness in human extrastriate cortex. *Neuron* **21**, 753–759.

Tootell, R. B., Reppas, J. B., Dale, A. M., Look, R. B., Sereno, M. I., Malach, R., Brady, T. J. & Rosen, B. R. 1995 Visual motion aftereffect in human cortical area M.T. revealed by functional magnetic resonance imaging. *Nature* **375**, 139–141.

Towe, A. L. & Harding, G. W. 1970 Extracellular microelectrode sampling bias. *Exp. Neurol.* **29**, 366–381.

Tuor, U. I., Malisza, K., Foniok, T., Papadimitropoulos, R., Jarmasz, M., Somorjai, R. & Kozlowski, P. 2000 Functional magnetic resonance imaging in rats subjected to intense electrical and noxious chemical stimulation of the forepaw. *Pain* **87**, 315–324.

Turner, R., Le Bihan, D., Moonen, C. T., DesPres, D. & Frank, J. 1991 Echo-planar time course MRI of cat brain oxygenation changes. *Magn. Resonance Med.* **22**, 159–166.

Ugurbil, K., Garwood, M., Ellermann, J., Hendrich, K., Hinke, R., Hu, X., Kim, S. G., Menon, R., Merkle, H. & Ogawa, S. 1993 Imaging at high magnetic fields: initial experiences at 4 T. *Magn. Resonance Q.* **9**, 259–277.

Ungerleider, L. G. & Desimone, R. 1986 Cortical connections of visual area MT in the macaque. *J. Comp. Neurol.* **248**, 190–222.

Van Zijl, P. C., Eleff, S. M., Ulatowski, J. A., Oja, J. M., Ulug, A. M., Traystman, R. J. & Kauppinen, R. A. 1998 Quantitative assessment of blood flow, blood volume and blood oxygenation effects in functional magnetic resonance imaging. *Nature Med.* **4**, 159–167.

Vanduffel, W., Fize, D., Mandeville, J. B., Nelissen, K., Van, H., Rosen, B. R., Tootell, R. B. H. & Orban, G. A. 2001 Visual motion processing investigated using contrast agent-enhanced fMRI in awake behaving monkeys. *Neuron* **32**, 565–577.

Vanzetta, I. & Grinvald, A. 1999 Increased cortical oxidative metabolism due to sensory stimulation: implications for functional brain imaging. *Science* **286**, 1555–1558.

Vanzetta, I. & Grinvald, A. 2001 Evidence and lack of evidence for the initial dip in the anesthetized rat: implications for human functional brain imaging. *Neuroimage* **13**, 959–967.

Vlaardingerbroek, M. & Den, B. 1996 *Magnetic resonance imaging: theory & practice*. Berlin: Springer.

Walker, P. M., Robin-Lherbier, B., Escanye, J. M. & Robert, J. 1991 Signal-to-noise improvement in mid-field MRI surface coils: a degree in plumbing? *Magn. Resonance Imaging* **9**, 927–931.

Wandell, B. A., Press, W. A., Brewer, A. & Logothetis, N. K. 2000 fMRI measurements of visual areas and retinotopic maps in monkey. *Soc. Neurosci. Abstracts* **26**, 821.

Wehr, M. & Laurent, G. 1999 Relationship between afferent and central temporal patterns in the locust olfactory system. *J. Neurosci.* **19**, 381–390.

Weisskoff, R. M., Zuo, C. S., Boxerman, J. L. & Rosen, B. R. 1994 Microscopic susceptibility variation and transverse relaxation: theory and experiment. *Magn. Resonance Med.* **31**, 601–610.

Wood, M. L. & Wehrli, F. W. 1999 Principles of magnetic resonance imaging. In *Magnetic resonance imaging* (ed. D. D. Stark & W. Bradley), pp. 1–14. St Louis, MO: Mosby.

Wyrwicz, A. M., Chen, N. K., Li, L. M., Weiss, C. & Disterhoft, J. F. 2000 fMRI of visual system activation in the conscious rabbit. *Magn. Resonance Med.* **44**, 474–478.

Yacoub, E. & Hu, X. 1999 Detection of the early negative response in fMRI at 1.5 tesla. *Magn. Resonance Med.* **41**, 1088–1092.

Zhang, Z. M., Andersen, A. H., Avison, M. J., Gerhardt, G. A. & Gash, D. M. 2000 Functional MRI of apomorphine activation of the basal ganglia in awake rhesus monkeys. *Brain Res.* **852**, 290–296.

Zhong, J., Kennan, R. P., Fulbright, R. K. & Gore, J. C. 1998 Quantification of intravascular and extravascular contributions to BOLD effects induced by alteration in oxygenation or intravascular contrast agents. *Magn. Resonance Med.* **40**, 526–536.

GLOSSARY

2DG: [^{14}C]deoxyglucose
BOLD: blood-oxygen-level-dependent
CBF: cerebral blood flow
CBV: cerebral blood volume
CMR: cerebral metabolic rate
CNR: contrast-to-noise ratio
DB: diagonal band of Broca
dHb: deoxyhaemoglobin
EEG: electroencephalography
EPSP: excitatory postsynaptic potential
EPI: echo planar imaging
FID: free induction decay
FLASH: fast low-angle shot
fMRI: functional magnetic resonance imaging
FOV: field of view
Gln: glutamine
Glu: glutamate
GM: grey matter
IPSP: inhibitory postsynaptic potential
LGN: lateral geniculate nuclei
LFP: local field potential
MB: mushroom body
MDEFT: modified driven equilibrium Fourier transform
MR: magnetic resonance
MRI: magnetic resonance imaging
MRS: magnetic resonance spectroscopy
MSN: medial septum nuclei
MT: middle temporal visual area
MUA: multi-unit activity
NMR: nuclear magnetic resonance
PET: positron emission tomography
PTN: pyramidal tract neuron
RF: radiofrequency
ROI: region of interest
SDF: spike-density function
SNR: signal-to-noise ratio
WM: white matter